ALL-EPITAXIALLY ORIENTATION-PATTERNED SEMICONDUCTORS FOR NONLINEAR OPTICAL FREQUENCY CONVERSION

A DISSERTATION

SUBMITTED TO THE DEPARTMENT OF APPLIED PHYSICS

AND THE COMMITTEE ON GRADUATE STUDIES

OF STANFORD UNIVERSITY

IN PARTIAL FULFILLMENT OF THE REQUIREMENTS

FOR THE DEGREE OF

DOCTOR OF PHILOSOPHY

Loren Alan Eyres

December 2001

I certify that I have read this dissertation and that, in my opinion, it is fully adequate in scope and quality as a dissertation for the degree of Doctor of Philosopy.

Martin M. Fejer, Principal Advisor

I certify that I have read this dissertation and that, in my opinion, it is fully adequate in scope and quality as a dissertation for the degree of Doctor of Philosopy.

James S. Harris

I certify that I have read this dissertation and that, in my opinion, it is fully adequate in scope and quality as a dissertation for the degree of Doctor of Philosopy.

Robert L. Byer

Approved for the University Committee on Graduate Studies:

Abstract

Nonlinear optical frequency conversion is an important technique for generation of mid-IR radiation from well-developed near-IR pumps like diode lasers and diode-pumped solid-state lasers. Zincblende semiconductor materials have excellent characteristics for optical frequency conversion including large nonlinearities and transparency through the mid-IR, but the absence of birefringence for phasematching has limited their application. Quasiphasematching provides an alternative solution to this phasematching problem, but requires techniques for inducing a modulation in the nonlinear susceptibility along the crystal. In this work we have developed all-epitaxial fabrication techniques for orientation-patterned semiconductor materials and have demonstrated that the resulting devices show excellent promise for mid-IR frequency conversion.

The two step fabrication technique requires making a template with the proper orientation pattern, which then serves as a substrate for orientation-patterned epitaxial growth. The template fabrication process utilizes polar-on-nonpolar molecular beam epitaxy (MBE) of a GaAs/Ge/GaAs heterostructure to achieve an epitaxial crystal inversion, after which the template is completed by a combination of photolithography and selective chemical etching. Orientation-patterned $Al_xGa_{1-x}As$ films grown on these templates exhibit ideal vertical antiphase domain propagation. Periods were demonstrated sufficient for quasiphasematching any collinear frequency mixing interaction in the transparency range of $Al_xGa_{1-x}As$. Orientation-patterned $Al_xGa_{1-x}As$ waveguiding structures were fabricated and utilized for harmonic generation of 1.55 μm laser radiation. The conversion efficiencies in these waveguide devices were limited by high modal propagation losses at both fundamental and harmonic wavelengths.

Thin GaAs orientation-patterned films were also used as templates for growth of much thicker (100s of μm) GaAs films by the hydride vapor phase epitaxy (HVPE) technique for bulk-focused frequency conversion. The antiphase boundaries were again observed to propagate vertically through the GaAs film with aspect ratios > 15:1. Periods sufficient to quasiphasematch parametric amplification using pump lasers of wavelength longer than 1.5 μm were demonstrated and excellent optical transmission was observed at both near-IR and mid-IR wavelengths. Frequency doubling of confocally-focused CO_2 laser radiation was performed in such an orientation-patterned film with efficiency close to theoretical.

Acknowledgements

Early in my Stanford career, a frequent visitor to the Byer-Fejer noontime group meeting said, in some superposition of seriousness and jest, that ". . .the meaning of life is to stay around Stanford as long as possible". The reasons for this attraction are obvious: the challenging intellectual environment, exceedingly talented and motivated colleagues, excellent resources, and many diverse opportunities. Though remaining as long as possible wasn't my intention, I have accumulated many enjoyable experiences and learned a great deal, both about physics and about life in general. I am grateful to all the people who have been a part of that; I am a wiser and better person as a result. In research, as in life, any large and meaningful project requires much help from others to be successful. Many more people played a part than I can hope to mention here.

My acknowledgements must begin with my advisor, Prof. Marty Fejer, who gave me the freedom to tackle a large project and supported me over the long time it took to complete it. His almost uncanny ability to ask penetrating questions and extract the essential elements of a problem from his interlocutor's mind proved invaluable for solving many of the problems we faced along the way. Prof. Jim Harris played a crucial role with his knowledge of epitaxy and his willingness to put a germanium source on MBE system II for this project (knowing it would contaminate the machine for other uses). I thank professor Prof. Bob Byer for his encouragement, especially during the bleakest periods of moving the MBE systems. I found it gratifying to hear him acknowledge the difficulties and frustrations of materials research.

Chris Ebert and Thierry Pinguet made possible the success of this project by doing the MBE growth and taking on lions' shares of MBE maintenance. Chris invested a great deal of effort in system modification and exploratory growths before we knew whether the scheme would work. I greatly enjoyed working with him, whether we were hunched over a RHEED screen looking at surface reconstructions, or setting up a tent somewhere in the Sierra Nevada. Thierry was somehow able to grow templates for the thick GaAs experiments in spite of myriad MBE problems. We characterized the first thick, orientation-patterned GaAs films together and discussed the meaning of life on our way back and forth to Livermore. Patrick Tourreau contributed significantly to getting the thick GaAs work underway while simultaneously becoming a fun housemate and good friend. Thierry, Ofer Levi, Torbjorn Skauli, and Luigi Scaccabarozzi continued to push the technology forward after I bowed out to write this dissertation and have generated very impres-

sive new results. Many other Harris group members also indirectly supported this project through their MBE maintenance efforts.

Extended collaboration with Eric Lallier, Loic Becouarn, and Bruno Gerard at Thales (Thomson-CSF) allowed this project to proceed much faster and further than we could have propelled it at Stanford alone. Their HVPE GaAs growth capabilities, combined with our templates, made possible all the thick GaAs results that demonstrate the utility of these materials and now motivate serious proposals for their commercialization. Tom Kulp and Scott Bisson from Sandia National Laboratories were also very helpful in pushing this technology forward through experimental collaboration and support.

My fellow students in the Byer-Fejer research group have probably been the most important part of making the lab a rewarding place to work. They were always willing to share ideas and humor, often willing to share equipment, and even occasionally willing to share work. In my first years I learned from more experienced students; in the later years I was able to reciprocate for a new generation. Eric Lim, Mike Bortz, Dieter Jundt, Gary Woods, Darwin Serkland, Steven Yang, and Chris Pohalski all preceded me through the graduate student experience and offered both models and lots of assistance. In my ultimately ill-fated exploration into wafer bonding I had Leslie Gordon and Dong Zheng as co-workers, with whom I shared equipment and frustrations. I remember many enjoyable and productive times with Bob Shine, Greg Miller, Larry Myers, Matt Husman, Mark Arbore, Bill Tulloch, Peter Byersdorf, Matthew Lawrence, Todd Rutherford, Justin Mansell, Gena Imeshev, Ming-Hsien Chou, Krishnan Parameswaran, Andy Schober, Jonathan Kurz, and Rob Batchko. The Ginzton faculty and students were also a large part of making the lab such a collegial place, whether in the courtyard at lunchtime or late at night in the hallways and microfabrication lab. I also have to acknowledge the AP entering class of ‘90 for support and distraction during that first long year of problem sets and laser laboratory experiments.

The group administration, including Kellie Koucky, Jackie Bretz, Annie Tran, Jo Major, and Sandy Bretz, somehow kept everything from falling apart and did their best to promote group unity using food. Eric Gustafson, Roger Route, and Bob Eckardt were always available for discussions about technology or life, while also taking care of tedious but important work like budgeting and proposal writing so that we as students could concentrate on research. Tom Carver always had helpful suggestions for dealing with microfabrication problems, as did Larry Randall for computer networking, machine shop, and automotive problems. Paula Perron and the other Applied Physics office staff saved me from stereotypically forgetting important deadlines and

incurring associated University fines. The Ginzton front office staff managed administrative issues we would usually rather avoid. Joe Vrhel and Chris Remen polished many oxide and semiconductor crystals for use in experiments. Dr. Mike Kelly helped me operate the XPS system and interpret the results.

Happily, I didn't spend the whole time at Stanford working. Singing with the Stanford Early Music Singers has been a very enjoyable distraction from the frustrations of research, particularly during long stretches of MBE downtime. Singing 15th century polyphony in the Memorial Church is an experience no one should miss. Classes and faculty in the French and Italian department, particularly involving Rene Girard and Jean-Pierre Dupuy, provided fascinating and existentially challenging intellectual diversions when I could take time away from research. Playing volleyball with the Ginzton GSB team gave me a good outlet for frustration and taught me a little about refereeing in a world where some people take things way too seriously. Thanks also to the friends who got me into swing dancing (especially Leslie Gordon) just in time for the late '90s swing revival in the Bay area.

After sharing a ramshackle house at 519 University Drive with 11 different housemates over eight years, I now have lots of good friends around the world who share my memories of leaking water heaters, broken automobiles, stolen bicycles, and occasional sleepwalking incidents. Thanks to all the friends with whom I have spent time working, playing or reflecting over the last decade. I feel a special gratitude towards everyone who was supportive during the last grueling phases of writing this dissertation.

Finally, I am grateful to my family. My brother Dean is my best friend and has always provided encouragement and a lot of fun whenever we have gotten together. I thank my parents, Jack and Marge Eyres, for the innumerable things they have given me over the years, including a life which has been filled with so many opportunities.

The research in this dissertation was supported by the Defense Advanced Research Projects Agency through the Office of Naval Research under the Center for Nonlinear Optical Materials (N00014-92-J-1903), by the Army Research Office under contract DAAH04-96-1-0002, and by the Department of Energy through Sandia National Laboratories under contract SNL4489.

Table of Contents

List of Tables

List of Figures

CHAPTER 1: New Materials for Nonlinear Optical Frequency Conversion

1.1 Introduction

From the initial optical harmonic generation experiments of Franken, *et al.* in 1961 [1], nonlinear optical frequency conversion has evolved over the past four decades into both an important tool for optical research and an ongoing subject of that research. In the last decade, nonlinear optical devices such as harmonic generators and parametric oscillators have moved out of the laboratory and become viable commercial products. Examples of this include frequency-doubled green sources to replace multi-Watt Ar+ ion lasers and optical parametric oscillators generating mid-IR radiation at the > Watt average power level for military countermeasure applications. These systems take advantage of recent advances in near-IR, diode-pumped, solid-state laser technology by converting the radiation from more easily and efficiently generated near-IR wavelengths out to the required visible and mid-IR wavelengths. The necessary high performance frequency conversion devices were enabled by recent advances in the fundamental understanding of and fabrication of nonlinear materials, in these cases $LiBO_3$, $LiNbO_3$ and $ZnGeP_2$.

Almost without exception, the performance of nonlinear optical devices and the range of their applications have historically been limited primarily by the available nonlinear optical materials and their characteristics. Many potentially interesting and useful applications, both scientific and industrial, await materials having sufficient conversion efficiency, transparency, and power handling capability. In this situation, the impact of advances in nonlinear optical material development is well illustrated by the explosion in device demonstration in the years following the development of electric-field-poling techniques for lithium niobate and other ferroelectric oxide materials (see, for example, the Conference on Lasers and Electro-Optics (CLEO) Technical Digests for 1996-1998). In this case, a material long used for nonlinear optical frequency conversion with birefringent phasematching achieved a qualitative advance in performance through development of techniques for tailoring the crystal structure on a microscopic scale to enable quasiphasematching. One of the highlight devices which resulted from this advance was the demonstration of a 93% pump-depleted continuous-wave (CW) singly-resonant optical parametric oscillator (SRO) generating 3.55 W of 3.25 μm idler radiation from a 1.064 μm pump laser using periodically-poled lithium niobate (PPLN) by Bosenberg, *et al.* [2]. Such a device would have been impossible to build four years earlier for lack of suitable crystals; in fact, the first CW SRO

was only demonstrated in 1992 [3] and was itself the beneficiary of advances in potassium titanyl phosphate (KTP) crystal development.

Zincblende semiconductors (GaAs, ZnSe, GaP) have attractive properties for frequency conversion except for their lack of birefringence. This lack of birefringence for phasematching or a practical alternative phasematching technique has historically prevented any significant frequency conversion applications. The goal of this dissertation has been to develop microscopic tailoring techniques for zincblende semiconductor materials in general and GaAs in particular to allow quasiphasematching and open up this class of materials for frequency conversion in a manner similar to the ferroelectric oxides. We have succeeded in developing all-epitaxial fabrication techniques for orientation-patterned gallium arsenide (OPGaAs) using polar-on-nonpolar epitaxy. Both bulk and waveguide OPGaAs devices have been fabricated and evaluated. Bulk devices perform as predicted theoretically with the known material parameters, while the waveguide device performance is limited by losses which should be reducible through further development of the fabrication process. These material and optical results confirm the potential of orientation-patterned GaAs and make it look promising for a range of frequency conversion applications.

This chapter provides an introduction to nonlinear optical frequency conversion devices and their operation, presents their potential applications, and compares the candidate materials for use in these devices. Following that, it reviews the prior research into quasi-phasematching in semiconductor materials, outlines the orientation-patterned crystal growth approach taken in this dissertation, and concludes with an overview of the rest of the dissertation.

1.2 Background

1.2.1 Nonlinear optical frequency conversion

In nonlinear optical frequency conversion, input beams at one or more optical frequencies interact through the nonlinear polarization in a crystal to generate beams at new frequencies. In each case, the generated frequency components are constrained by the relationship $\omega_3 = \omega_2 \pm \omega_1$, so that all three frequencies must be present in either the input or output or both. The polarization induced in a medium can be expanded as a Taylor series in the applied electric field

$$\boldsymbol{P}_i = \varepsilon_0(\chi_{ij}^{(1)}\boldsymbol{E}_j + \chi_{ijk}^{(2)}\boldsymbol{E}_j\boldsymbol{E}_k + \chi_{ijkl}^{(3)}\boldsymbol{E}_j\boldsymbol{E}_k\boldsymbol{E}_l + \ldots) \tag{1.1}$$

with the first term producing the linear effects usually described in terms of the dielectric constant or the index of the refraction, the next term generating the second-order effects we utilize in this dissertation, and the third-order term producing effects such as the nonlinear index and four-wave mixing. The interactions enabled by this second-order susceptibility $\chi_{ijk}^{(2)}$ are shown in Table 1.1 and include second harmonic generation (SHG), sum frequency generation (SFG), difference frequency generation (DFG), and parametric amplification, which is like DFG but with much stronger input beams at the pump than at the signal frequency, which can produce extremely high amplification at the signal and idler frequencies. Placing a resonant cavity around the parametric

process	**input frequencies**	**output frequencies**	**relationship**
SHG	ω_1	ω_2	$\omega_2 = \omega_1 + \omega_1$
SFG	ω_1, ω_2	ω_3	$\omega_3 = \omega_2 + \omega_1$
DFG	ω_3, ω_2	ω_1	$\omega_3 - \omega_2 = \omega_1$
OPA	ω_{pump}, ω_{signal}	ω_{idler}, ω_{signal}	$\omega_{pump} - \omega_{signal} = \omega_{idler}$

Table 1.1: Second-order nonlinear optical frequency conversion processes.

amplifier provides feedback which in combination with the parametric gain results in a parametric oscillator when the round trip gain exceeds the round trip loss. All of these processes are explored in more detail in Chapters 2 and 6.

1.2.2 Phasematching and efficiency

In general, this nonlinear conversion process is extremely inefficient unless the problem of phasematching is solved in some manner. The phasematching problem arises because dispersion in the medium causes a phase velocity mismatch between the nonlinear polarization of Equation (1.1) and the wave it radiates, causing them to walk quickly out of phase and limiting the coherent interaction length in the material to a distance typically beween a few microns and a few hundred microns. The effects of phasematching are illustrated in Figure 1.1 using the example of second harmonic generation. In the unphasematched case, the radiated harmonic power reaches a maximum after one coherence length, after which the polarization and the radiated wave walk out of phase and power repeatedly oscillates between fundamental and harmonic. In the perfectly phasematched, plane-wave, non-depleted pump case, the radiated second harmonic power grows parabolically with propagation distance in the medium and input fundamental power according to

$$P_{SH} = \eta P_F^2 L^2 . \tag{1.2}$$

Since nonlinear crystals can have several cm lengths, phasematching can enhance the efficiency by factors up to (few cm/few μm)^2 ~ 10^8. With phasematching, power conversion efficiencies around 50% can typically be achieved with SHG and OPO devices. Historically, the problem of phasematching was solved primarily by utilizing the different refractive indices for differently polarized waves in birefringent crystals. By choosing the proper combination of input and output polarizations and the proper propagation angle in the crystal, the phase mis-match could be cancelled and the parabolic dependence on crystal length realized. Virtually all successful nonlinear optical frequency conversion until the last decade was achieved using these birefringent phasematching techniques. Unfortunately the isotropic optical properties of the zincblende semiconductor materials such as GaAs preclude birefringent phasematching, so an alternative technique must be used for these materials.

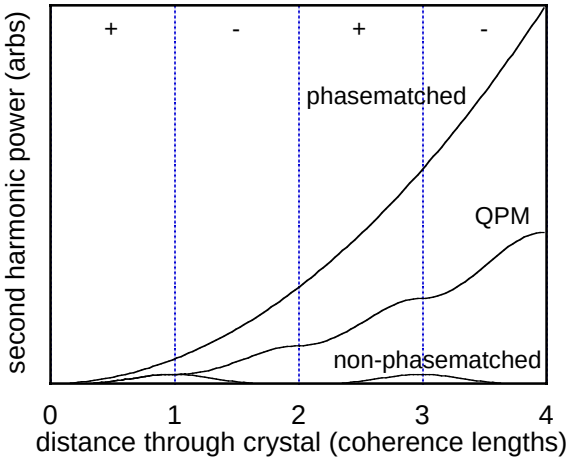

Figure 1.1: Impact of phasematching on frequency conversion efficiency as a function of distance through crystal including phasematched, quasi-phasematched, and non-phasematched cases.

1.2.3 Quasiphasematching

Quasiphasematching [4] utilizes a periodic modulation of the material parameters to compensate for the phase mismatch. This modulation is usually in the nonlinear susceptibility $\chi_{ijk}^{(2)}$ and the highest efficiencies are obtained when the modulation alternates sign (+/-). Figure 1.1 also illustrates the effect of quasiphasematching. After the nonlinear polarization and radiated wave walk out of phase over one coherence length, the sign of the susceptibility is reversed and the relative phase between them is reset, allowing the radiation from the following section of the crystal to add in phase rather than out of phase. With the proper periodic modulation period along the prop-

agation direction in the crystal, radiation from the entire crystal adds approximately in phase resulting in a quasi-parabolic increase in the conversion with crystal length, as shown in Figure 1.1. Using quasiphasematching techniques, high conversion efficiencies can be obtained with crystals such as GaAs which have otherwise excellent properties for frequency conversion but exhibit no birefringence. Figure 1.2 shows the domain periods required for quasiphasematching parametric amplification in GaAs with various pump wavlengths. For pumping at 2 μm, coherence lengths (half of the domain period for optimal first-order quasiphasematching) of 30 μm - 45 μm are required, depending on the signal and idler wavelengths, while for 1-μm pumping the required coherence lengths are 4 μm - 10 μm.

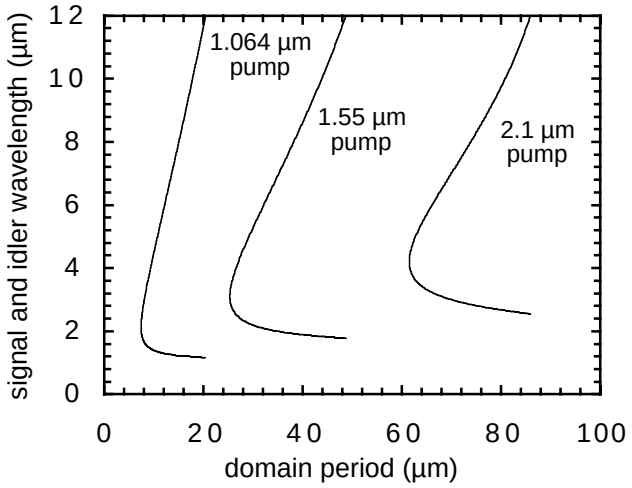

Figure 1.2: Domain periods required for quasiphasematching parametric amplification in GaAs for various pump wavelengths.

Fabrication of crystals with such a periodic modulation of the nonlinear susceptibility is nontrivial; the methods which are successful in one material system do not necessarily carry over into others. Therefore, the key to achieving high-performance, quasi-phasematched frequency conversion is the invention and development of techniques for fabricating media with modulated nonlinear susceptibility. This dissertation presents a practical technique for growing GaAs crystals with a built-in crystal orientation pattern which achieves a periodic sign modulation in the nonlinear susceptibility and makes possible quasiphasematched frequency conversion.

1.3 Applications

There are two major categories of application for quasi-phasematched semiconductor frequency conversion materials, mid-IR generation and communication devices.

1.3.1 Mid-IR generation

The mid-IR transparency of GaAs and other zincblende semiconductors makes them attractive for applications which require wavelengths beyond the ~ 5-μm long-wavelength transparency limit in oxide crystals, or those which require high power at wavelengths longer than 4 μm, where thermal loading can become a limitation in oxide crystals. These applications exist over a wide range of output power levels and pulse/temporal formats, from low average power (nW) to high average power (>10 W), from continuous-wave (CW) to ultrashort (fs) pulses. Running roughly from lowest to highest power, these applications include spectroscopy for fundamental science and industrial applications, remote sensing for environmental applications, and sensors/countermeasures for military applications.

Mid-IR spectroscopy applications typically require tunable narrow-linewidth sources with power levels depending on the context, concentrations, and spectroscopic technique [5-7]. The mid-IR is attractive for spectroscopy because many molecules have strong vibrational spectra which allows high-sensitivity measurement. Recently developed cavity ringdown spectroscopy techniques offer orders of magnitude higher sensitivities due to their extremely long effective path lengths [8, 9]. Similar techiques can be used for chemical detection, both in industrial processes and in the ambient environment [10, 11]. The atmospheric transmission windows of 3 μm - 5 μm and 8 μm - 12 μm restrict remote sensing applications within the mid-IR wavelength range. Remote sensing of atmospheric or biological chemicals and laser radar require high quality beams and higher power levels to compensate for power loss in atmospheric propagation and low efficiency collection of scattered radiation from the distant targets [12-14]. Many military countermeasures applications require multi-Watt average power levels at particular wavelengths to disrupt missile seekers operating in the mid-IR transmission windows. Many of these applications also have engineering constraints such as size, weight, and power consumption if they are to be used in real-world environments rather than in a laboratory.

1.3.2 Optical communications

Semiconductor-based nonlinear optical waveguides also have potential applications in photonics technology for optical communications. Wavelength conversion will be an essential

function for future transparent WDM networks and waveguide nonlinear optical frequency conversion has already demonstrated these functions with excellent efficiencies and linearity. Such frequency conversion devices fabricated from periodically-poled lithium niobate are capable of converting a bit stream between wavelength channels at efficiencies of –3dB using only tens of mW of pump power [15]. The three-frequency-mixing approach has the advantage of being all-optical, requiring no conversion of photons into electrons, and therefore should easily adapt to higher bit rates in the future. Such nonlinear waveguide devices have demonstrated simultaneous multi-channel conversion as well as other functions such as mid-span spectral inversion. Use of semiconductor waveguides would in principle have several advantages including higher efficiencies, which would reduce pump power requirements, and input polarization-independent wavelength conversion [16], something the current lithium niobate-based devices can't achieve without additional device complexity. Since the horizon for implementation in these communication applications appears further away than for the mid-IR applications, the remainder of this chapter will focus on the mid-IR, leaving further discussion of communication applications and devices for chapter 4.

1.4 Mid-IR sources

Some of these requirements for mid-IR sources will be met by non-frequency conversion devices, but no general solution exists which offers every desired combination of high beam quality, narrow linewidths, scalable output power, tunability, room-temperature operation, compact size and robustness. Solid-state lasers operate over limited wavelength ranges around 2 μm (Ho,Tm:YAG) and 3 μm (Er:YAG). Gas lasers such as CO_2 (10 μm) and chemical lasers like HF and DF also provide sources at specific mid-IR wavelengths. Lead-salt diode lasers can operate in this range with low output power levels, but only at the cost of cryogenic cooling. The newly-developed quantum cascade lasers have great promise, having demonstrated emission over the whole mid-IR, and will certainly solve some subset of problems, but have limitations on power output and beam quality and generally require tradeoffs between temporal format and cryogenic cooling.

Meanwhile, near-IR laser diodes and diode-pumped solid-state lasers in the 1.0 - 2.0 μm wavelength range are well-developed, possessing all of these desirable attributes. For this reason, mid-IR generation using nonlinear frequency conversion with these versatile near-IR pumps is a highly appealing strategy for many mid-IR applications provided that the nonlinear optical devices

achieve sufficient performance, a question which depends primarily on the capabilities of the nonlinear crystals. The most commonly used materials for mid-IR frequency conversion are the chalcopyrites, including $ZnGeP_2$, $AgGaSe_2$, and $AgGaS_2$, and $CdGeAs_2$, which are presently available in cm-scale aperatures and multiple cm lengths.

$ZnGeP_2$ has been used effectively for generation over much of the mid-IR spectrum, but suffers from absorption issues at short wavelength, which constrains pump lasers to operate at wavelengths > 2.0 μm, and at long wavelength, where phonon-related absorption limits efficiencies for wavelengths $\geq$ 9.0 μm. Perhaps the most impressive device reported is that of Budni, *et al.* [17], who demonstrated generation of 10 W combined mid-IR power at 3.67 μm and 4.67 μm from 20 W of pump power with a $ZnGeP_2$ OPO. Optical parametric generation has been used to produce longer wavelengths out to 11 μm [18], as have recent OPO devices used for spectroscopy applications [19].

$AgGaSe_2$ has similarly been useful for generation of radiation through the mid-IR, but is limited by thermal complications at high power levels due to the low thermal conductivity. Low-power tunable CW spectroscopy sources around 8 μm have been demonstrated in $AgGaSe_2$ using near-IR diode lasers as pump sources [20]. OPO experiments by Budni, *et al.* [21] observed thermal lensing in 2 μm-pumped $AgGaSe_2$ OPOs which limited the conversion efficiency. Moving away from the unfortunate absorption bands around 2 μm, Chandra, *et al.* [22] demonstrated a tunable 6-14 μm OPO output with 6 ns pulse width at the mJ level for lidar applications. 120 fs pulses tunable from 4-8 μm were also generated from a sync-pumped $AgGaSe_2$ OPO pumped at 1.57 μm [23]. Tunable output from 8 μm - 12 μm at the mJ level has also been demonstrated by DFG in a $AgGaSe_2$ crystal of the signal and idler out of a 1-μm-pumped KTP OPO [24].

$CdGeAs_2$ devices have been demonstrated, but the applications are limited by the requirement that the pump wavlength be > 3 μm to avoid excess absorption, so it typically must be pumped by another nonlinear frequency conversion device. Vodopyanov and Schunemann [25] demonstrated tunable DFG of 7 μm - 20 μm radiation in $CdGeAs_2$ using a 2.8-μm-pumped double-pass $ZnGeP_2$ optical parametric generator as a pump source.

1.5 Comparison of NLO materials

GaAs has excellent characteristics for frequency conversion, as can be seen from a comparison with those of the materials mentioned in the previous section. Table 1.2 shows several of the material properties important for frequency conversion. Material parameters are taken from several references [26-29]. Attenuation values vary in the references and the ones selected here are representative of the best production crystals. Three different sets of attenuation data are shown for GaAs, including typical bulk GaAs wafers, HVPE-grown GaAs films, and orientation-patterned GaAs with 27 μm period sufficient for phasematching frequency conversion pumped in the near-IR. The dramatic drop in near-IR attenuation for HVPE GaAs compared to regular bulk

material	d_{ij} and maximum d_{eff} (pm/V)	FOM $(pm/V)^2$	transparency range (μm)	thermal conductivity (W/m-K)	attenuation (cm^{-1}) (absorption + scattering) 1 μm	2 μm	10 μm	walkoff angle (°)
GaAs	90 (66)	400	0.9 - 12	52	~ 1	0.01	0.01	0 (QPM)
HVPE-GaAs					0.025			
OPGaAs					0.1	0.03*		
ZnSe	50 (37)	423	0.5 - 20	18	0.001	0.001	0.0005	0 (QPM)
$ZnGeP_2$	72	522	0.74 - 12	35	1.0	0.09	0.9	0.65
$AgGaSe_2$	34	171	0.7 - 12	1	0.01	0.03	0.01	0.64
$CdGeAs_2$	236	4483	2.3 - 18	4.2	----	----	0.01	----
$AgGaS_2$	13	29	0.5 - 13	11.5	0.001	0.08	0.6	
$LiNbO_3$	27 (17)	67	0.35 - 5	5.6	0.001	0.001	----	
* OPGaAs attenuation value at 1.55 μm from [30]								

Table 1.2: Properties of materials used for mid-IR nonlinear optical frequency conversion.

crystal GaAs is due to higher purity and crystal quality. There is some disagreement about the magnitude of d_{14} for GaAs, with several authors reporting values consistent with 83 pm/V for 10.6 μm frequency doubling [31], while others observe efficiencies consistent with larger values of 120 pm/V [32] to 150 pm/V [33]. Throughout this dissertation all calculations will assume 90 pm/V value for 10.6 μm frequency doubling scaled by the constant Miller's delta (CMD) [34] approximation for the sake of consistency. Results can easily be scaled to adjust as this discrepancy is resolved. The magnitude of d_{14} for ZnSe is highly uncertain [31, 35]. The walkoff angles are given for 2 μm pumping of a degenerate OPO.

One can define a material figure of merit proportional to the confocally-focused conversion efficiency in the regime not limited by absorption losses as FOM = d_{eff}/n^2. GaAs and

ZnSe have large FOMs comparable that for $ZnGeP_2$, while exhibiting low optical loss out to 12 μm and 20 μm for GaAs and ZnSe, respectively. This long wavelength transparency and large FOM, combined with the transparency of GaAs and ZnSe down to 1 μm, should give them significant advantages over the similar $AgGaSe_2$ and $AgGaS_2$ which are used for long wavelength generation. In addition, both GaAs and ZnSe have large thermal conductivities which will reduce dramatically the thermal focusing effects which have complicated $AgGaSe_2$ device operation. OPGaAs has demonstrated lower attenuation at the three tabulated wavelengths than $ZnGeP_2$. The attenuation at 1 μm and 2 μm in OPGaAs is likely dominated at present by scattering associated with the unoptimized orientation-patterned growth, so the thermal performance may actually be even better. Bulk ZnSe exhibits extremely low attenuation over an extremely wide wavelength range; it is not clear, however, whether such low losses would be obtainable in orientation-patterned material, as additional attenuation effects might arise. Since they utilize utilize quasiphase-matching, the zincblende materials don't suffer from Poynting vector walkoff which restricts focusing in long crystals and limits the single pass gains. From comparison of the material parameters alone, it is reasonable to expect that orientation-patterned GaAs (and ZnSe) could perform as well or better than the present state-of-the art nonlinear optical materials for mid-IR generation, particularly in the 9-12 μm wavelength region.

1.6 History of QPM in semiconductors

The attractiveness of zincblende semiconductors and GaAs in particular for frequency conversion has motivated a number of attempts to achieve practical quasiphasematching. This section reviews the previous research into quasiphasematching for bulk (focused gaussian beam) configurations. Research into phasematching techniques such those utilizing quantum wells which apply only in waveguides devices is covered in chapter 4. Achieving a periodically modulated nonlinear susceptibility in GaAs is somewhat more difficult than accomplishing the same thing in lithium niobate and other ferroelectrics, since GaAs exhibits no ferroelectricity and there is no method for inducing a susceptibility modulation into a uniform crystal. Instead, the local crystal orientation must be modulated periodically, something which can be done using two strategies. In the first, a GaAs crystal is cut into plates, the orientation of every second plate is physically reversed, and then the whole stack of plates is fused back together. In the second, a template whose crystallographic orientation is patterned across its surface is fabricated first, after which

thick or thin films are grown on that template under conditions where the orientation-pattern is preserved in the growing layers.

1.6.1 Stack of plates

The first successful demonstration of quasiphasematching in GaAs by Szilagyi, *et al.* [36] utilized GaAs plates aligned at Brewster's angle to minimize losses due to Fresnel reflections. They demonstrated enhancement of nonlinear frequency conversion, but the plates required precise individual alignment and such a scheme was clearly not mechanically robust. By the addition of wafer-bonding to the stack-of-plates technique, Gordon, *et al.* [37] fabricated a robust and monolithic structure more suitable for real applications. Not only were the individual plates fused into a single monolithic crystal, but this fusion eliminated the residual Fresnel losses resulting from air/GaAs interfaces. Using such structures, groups at Stanford and at Thomson-CSF were able to demonstrate SHG [33, 37], DFG [38, 39], and even an OPO, though the OPO oscillated only briefly before the crystal damaged [40]. One advantage of this technique is that it enables crystals of arbitrarily large aperture, easily scaling to two or three inch wafer diameters. There also are several disadvantages, however. The serial fabrication process scales poorly (since ever more plates are required) to the long sample lengths desirable for frequency conversion. As the plate thickness drop significantly below ~ 100 μm, polishing and handling the thin plates becomes more problematic. Looking back at Figure 1.2, the coherence lengths required for pumping at wavelengths ≤ 2 μm would be virtually unfabricable using this technique, forcing one to use higher order QPM at much reduced efficiencies.

One of the few demonstrated alternatives to the stack of plates technique took advantage of the phase shifts on total internal reflection to phasematch harmonic generation in a single thin plate of GaAs, ZnSe, and ZnS [41, 42]. This approach followed the original suggestions of Bloembergen [43]. It is limited by tight tolerances on the precise plate thickness, limited aperture size, and residual losses due to the repeated total internal reflections from the plate surfaces.

1.6.2 Orientation-patterned epitaxial growth

The second strategy for obtaining an orientation-modulated GaAs crystal is to grow orientation-patterned layers following a previously fabricated template. This technique has several advantages over the wafer bonding approach. First, the template orientation-pattern dimensions can be set using photolithography, eliminating tolerances on plate polishing and manageable plate thicknesses. In principle, narrow periods are equally fabricable as wide periods. The device

lengths can be extended up to wafer size without difficulty. Many different devices with different gratings can easily be fabricated in parallel; more complicated non-periodic grating structures, such as chirped gratings for pulse compression, can be fabricated straightforwardly as well. Finally, this technique is also compatible with heterostructure waveguide fabrication. The only intrinsic drawback to this strategy is that the aperture size is limited in one dimension to whatever thickness can be grown epitaxially.

Historically, there are some precedents for this approach. Angell, *et al.* [44] invented a technique for orientation-patterned growth of II-VI ZnSe/ZnTe semiconductor waveguides using patterned CdTe seeding layers. The devices had on/off modulation of the nonlinear susceptibility as the ZnSe/ZnTe growth axis alternated between [001] and [111] across the plane of the film. Unfortunately, the lack of symmetry between the orientations complicated growth of orientation-patterned layers and resulted in devices with disappointingly high propagation losses. More successful orientation-patterning methods were developed by Yoo, *et al.* employing templates fabricated by wafer-bonding two GaAs wafers using InGaP bonding layers. They grew waveguide devices and demonstrated SHG [45] and DFG [16], determining that the waveguide performance was limited by high waveguide losses. Similar work was done later by Xu, *et al.* [46].

1.7 All-epitaxial template fabrication

The central advance in this dissertation is the invention of a more elegant approach to template fabrication employing only epitaxial techniques, particularly polar-on-nonpolar heteroepitaxy. Unlike the case of Angell [44], this strategy results in +/- patterning of the susceptibility with both orientations having the same axis along the [001] growth direction, thereby eliminating the complications with orientation-patterned crystal growth. This breakthrough has enabled fabrication of both waveguide and bulk nonlinear optical devices which show excellent promise for becoming practical solutions to nonlinear optical frequency conversion problems.

The fabrication process is illustrated in Figure 1.3 It begins with growth of a GaAs/Ge/GaAs heterostructure in which the top GaAs layer has an antiphase or inverted crystallographic orientation with respect to the substrate. The lattice-matched Ge layer functions as a nonpolar buffer to separate the orientations and make possible the inversion of the top GaAs layer, which would otherwise follow the orientation of the substrate. After growth of the heterostructure, the wafer is removed from the epitaxial growth system and photolithographically patterned with a grating pattern across the surface. The wafer is then exposed to an etchant which will etch through

the top GaAs and Ge layers, exposing the orientation of the underlying substrate in clear regions while the areas protected by the photoresist are unaffected. Removal of the photoresist leaves the desired template with an orientation-patterned wafer surface. The technique has demonstrated orientation-patterned templates with the periods required for quasi-phasematching frequency conversion over the whole transparency range of GaAs/AlGaAs. After template fabrication, the template is then placed back into the epitaxial growth environment for subsequent growth of either waveguiding or thick layers in which frequency conversion will be performed.

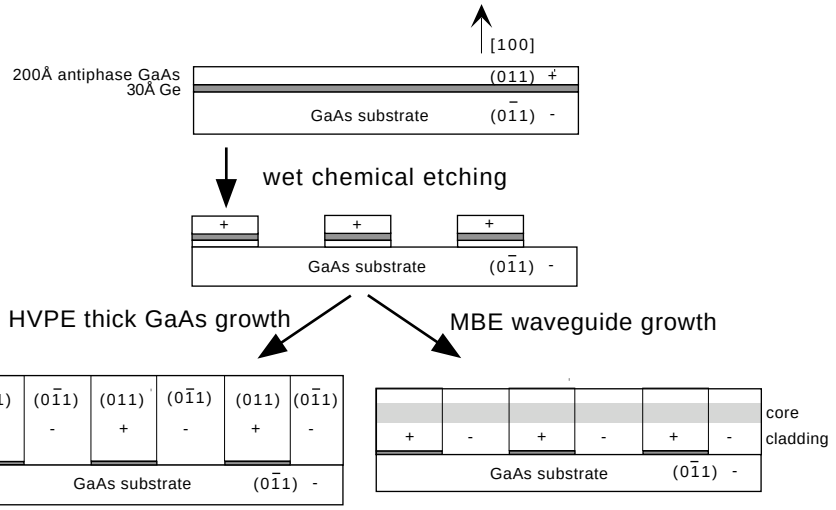

Figure 1.3: Schematic fabrication process for orientation-patterned GaAs.

Similar work has been independently undertaken at the University of Tokyo using both Ge and Si nonpolar layers [47, 48]. Researchers determined that Ge buffers layers worked better then Si buffers, which is not surprising given the relative lattice parameters of the materials. This work will be described in more detail in Chapter 3.

1.8 Dissertation overview

Chapter 2 will introduce the basic theoretical background necessary for predicting the performance of nonlinear frequency converters, both bulk and waveguide. Chapter 3 discusses all-epitaxial orientation control and the GaAs/Ge/GaAs epitaxial techniques. It then describes the fabrication of template structures and the growth of basic orientation-patterned films. Chapter 4 examines thin-film waveguide devices fabricated using the orientation-templates, evaluating both

linear and nonlinear optical properties of these devices. The growth and evaluation of thick OPGaAs films appears in Chapter 5 along with the excellent optical frequency conversion results obtained in them. Chapter 6 contains analysis and predictions about the potential performance of orientation-patterned GaAs crystals in parametric devices, after which Chapter 7 summarizes the dissertation.

References

1. P.A. Franken, A.E. Hill, C.W. Peters, and G. Weinreich, "Generation of optical harmonics," Phys. Rev. Lett. **7**, 118-119 (1961).

2. W.R. Bosenberg, A. Drobshoff, J.I. Alexander, L.E. Myers, and R.L. Byer, "93% pump depletion, 3.5 W continuous-wave, singly resonant optical parametric oscillator," Opt. Lett. **21**, 1336-1338 (1996).

3. S.T. Yang, R.C. Eckardt, and R.L. Byer, "Continuous-wave singly resonant optical parametric oscillator pumped by a single-frequency resonantly doubled Nd:YAG laser," Opt. Lett. **18**, 971-973 (1993).

4. M.M. Fejer, G.A. Magel, D.H. Jundt, and R.L. Byer, "Quasi-phase-matched second harmonic generation: tuning and tolerances," IEEE J. Quantum Electron. **28**, 2631-2654 (1992).

5. J.J. Scherer, K.W. Aniolek, N.P. Cernansky, and D.J. Rakestraw, "Determination of methyl radical concentrations in a methane/air flame by infrared cavity ringdown spectroscopy," J. Chem. Phys. **107**, 6196-6203 (1997).

6. W.C. Eckoff, R.S. Putnam, S. Wang, R.F. Curl, and F.K. Tittel, "A continuously tunable long-wavelength CW IR source for high-resolution spectroscopy and trace-gas detection," *Conference on Lasers and Electro-Optics*, OSA Technical Digest (Optical Society of America, Washington, DC, 1996) pp. 440-441.

7. A.A. Kosterev, R.F. Curl, F.K. Tittel, C. Gmachl, F. Capasso, D.L. Sivco, J.N. Baillargeon, A.L. Huchinson, and A.Y. Cho, "Methane concentration and isotopic composition measurements with a mid-infrared quantum-cascade laser," Opt. Lett. **24**, 1762-1764 (1999).

8. K.W. Aniolek, T.J. Kulp, B.A. Richman, S.E. Bisson, and P.E. Powers, "Development of a compact cavity-ringdown spectrometer using a PPLN-based OPG/OPA light source," *Conference on Lasers and Electro-Optics (CLEO)*, OSA Technical Digest (Optical Society of America, Washington, DC, 1999) pp. 193-194.

9. B.A. Paldus, C.C. Harb, T.G. Spence, R.N. Zare, C. Gmachl, F. Capasso, D.L. Sivco, J.N. Baillargeon, A.L. Hutchinson, and A.Y. Cho, "Cavity ringdown spectroscopy using mid-infrared quantum-cascade lasers," Opt. Lett. **25**, 666-668 (2000).

10. P.E. Powers, T.J. Kulp, and R. Kennedy, "Demonstration of differential backscatter absorption gas imaging," Appl. Opt. **39**, 1440-1448 (2000).

11. Y. Mine, N. Melander, D. Richter, D.G. Lancaster, K.P. Petrov, R.F. Curl, and F.K. Tittel, "Detection of formaldehyde using mid-infrared difference-frequency generation," Appl. Phys. B. **65**, 771-774 (1997).

12. L.B. Whitbourn, R.N. Phillips, G. James, M.T. O'Grien, and M.D. Waterworth, "An airborne multiline CO_2 laser system for remote sensing of minerals," Jour. Modern Opt. **37**, 1365-1372 (1990).

13. P.F. Ambrico, A. Amodeo, P. DiGirolamo, and N. Spinelli, "Sensitivity analysis of differential absorption lidar measurements in the mid-infrared spectral region," Appl. Opt. **39**, 6847-6865 (2000).

14. S.W. Lee, J. McNeil, T. Zenker, and T.H. Chyba, "A mid-IR OPO based lidar system for DIAL measurements of tropospheric methane concentration," *Conference on Lasers and Electro-Optics*, OSA Technical Digest (Optical Society of America, Washington, DC, 1999) p. 425.

15. M.H. Chou, J. Hauden, M.A. Arbore, and M.M. Fejer, "1.5-μm-band wavelength conversion based on difference-frequency generation in $LiNbO_3$ waveguides," Opt. Lett. **23**, 1004-1006 (1998).

16. S.J.B. Yoo, C. Caneau, R. Bhat, M.A. Koza, A. Rajhel, and N. Antoniades, "Wavelength conversion by difference frequency generation in AlGaAs waveguides with periodic domain inversion achieved by wafer bonding," Appl. Phys. Lett. **68**, 2609-2611 (1996).

17. P.A. Budni, L.A. Pomeranz, M.L. Lemons, P.G. Schunemann, T.M. Pollak, and E.P. Chicklis, "10 W mid-IR holmium pumped $ZnGeP_2$ OPO," *Advanced Solid State Lasers*, OSA Trends in Optics and Photonics (TOPS) Vol. 19, W.R. Bosenberg and M.M. Fejer, eds. (Optical Society of America, Washington, DC, 1998) pp. 226-229.

18. V. Petrov, Y. Tanaka, and T. Suzuki, "Parametric Generation of 1-ps pulses between 5 and 11 μm with a $ZnGeP_2$ crystal," IEEE J. Quantum Electron. **33**, 1749-1755 (1997).

19. K.L. Vodopyanov, F. Ganikhanov, J.P. Maffetone, I. Zwieback, and W. Ruderman, "$ZnGeP_2$ optical parametric oscillator with 3.8-12.4 μm tunability," Opt. Lett. **25**, 841-843 (2000).

20. K.P. Petrov, R.F. Curl, F.K. Tittel, and L. Goldberg, "Continuous-wave tunable 8.7 μm spectroscopic source pumped by fiber-coupled communications lasers," Opt. Lett. **21**, 1451-1453 (1996).

21. P.A. Budni, M.G. Knights, E.P. Chicklis, and K.L. Schepler, "Kilohertz $AgGaSe_2$ optical parametric oscillator pumped at 2 μm," Opt. Lett. **18**, 1068-1070 (1993).

22. S. Chandra, T.H. Allik, G.C. Catella, R. Utano, and J.A. Hutchinson, "Continuously tunable, 6-14 μm silver-gallium selenide optical parametric oscillator pumped at 1.57 μm," Appl. Phys. Lett. **71**, 584-586 (1997).

23. S. Marzenell, R. Beigang, and R. Wallenstein, "Synchronously pumped femtosecond optical parametric oscillator based on $AgGaSe_2$ tunable from 2 μm to 8 μm.," Appl. Phys. B **69**, 423-428 (1999).

24. R. Utano and M.J. Ferry, "8-12 μm generation using difference frequency generation in $AgGaSe_2$ of a Nd:YAG pumped KTP OPO," *Advanced Solid State Lasers*, OSA Trends in Optics and Photonics (TOPS) Vol. 10, C.R. Pollak and W.R. Bosenberg, eds. (Optical Society of America, Washington, DC, 1997) pp. 267-269.

25. K.L. Vodopyanov and P.G. Schunemann, "Efficient difference-frequency generation of 7-20 μm radiation in $CdGeAs_2$," Opt. Lett. **23**, 1096-1098 (1998).

26. P.F. Bordui and M.M. Fejer, "Inorganic crystals for nonlinear optical frequency conversion," Annu. Rev. Mater. Sci. **23**, 321-379 (1993).

27. G.C. Catella and D. Burlage, "Crystal growth and optical properties of $AgGaS_2$ and $AgGaSe_2$," MRS Bulletin **23**, 28-36 (1998).

28. P.G. Schunemann and T.M. Pollak, "Ultralow gradient HGF-grown $ZnGeP_2$ and $CdGeAs_2$ and their optical properties," MRS Bulletin **23**, 23-27 (1998).

29. L. Gordon, R.C. Eckardt, and R.L. Byer, "Investigations of diffusion-bonded stacked GaAs for infrared quasi-phasematched parametric oscillation," *Nonlinear Optics for High-Speed Electronics and Optical Frequency Conversion*, Proceedings of the SPIE (Society of Photo-Optical Instrumentation Engineers, Bellingham, WA, 1994) pp. 316-326.

30. T.J. Pinguet, O. Levi, T. Skauli, L.A. Eyres, L. Scaccabarozzi, M.M. Fejer, J.S. Harris, T.J. Kulp, S. Bisson, B. Gerard, L. Becouarn, and E. Lallier, "Characterization of 0.5 mm thick films of orientation-patterned GaAs for nonlinear optical applications," *Conference on Lasers and Electro-Optics*, OSA Trends in Optics and Photonics (TOPS) Vol. 56 (Optical Society of America, Washington, DC, 2001) p. 138.

31. I. Shoji, T. Kondo, A. Kitamoto, M. Shirane, and R. Ito, "Absolute scale of second-order nonlinear-optical coefficients," J. Opt. Soc Am. B **14**, 2268-2294 (1997).

32. T. Skauli, personal communication to L. Eyres (2001).

33. L. Becouarn, E. Lallier, M. Brevignon, and J. Lehoux, "Cascaded second-harmonic and sum-frequency generation of a CO_2 laser using a single quasi-phase-matched GaAs crystal," Opt. Lett. **23**, 1508-1510 (1998).

34. R.C. Miller, "Optical second harmonic generation in piezo-electric crystals," Appl. Phys. Lett. **5**, 17-19 (1964).

35. S. Singh, "Nonlinear Optical Properties," in *Handbook of Laser Science and Technology*, M.J. Weber ed. (CRC Press, Boca Raton, FL, 1986) pp. 3-228.

36. A. Szilagyi, A. Hordvik, and H. Schlossberg, "A quasi-phase-matching technique for efficient optical mixing and frequency doubling," J. Appl. Phys. **47**, 2025-2032 (1976).

37. L. Gordon, G.L. Woods, R.C. Eckardt, R.R. Route, R.S. Feigelson, M.M. Fejer, and R.L. Byer, "Diffusion-bonded stacked GaAs for quasi-phase-matched second-harmonic generation of a carbon dioxide laser," Electron. Lett. **29**, 1942-1944 (1993).

38. D. Zheng, L. Gordon, Y.S. Wu, R.S. Feigelson, M.M. Fejer, R.L. Byer, and K.L. Vodopyanov, "16-μm infrared generation by difference-frequency mixing in diffusion-bonded-stacked GaAs," Opt. Lett. **23**, 1010-1012 (1998).

39. E. Lallier, L. Becouarn, M. Brevignon, and J. Lehoux, "Infrared difference frequency generation with quasi-phase-matched GaAs," Electron. Lett. **34**, 1609-1611 (1998).

40. E. Lallier, personal communication to L.A. Eyres (2000).

41. G.D. Boyd and C.K.N. Patel, "Enhancement of optical second-harmonic generation (SHG) by reflection phase matching in ZnS and GaAs," Appl. Phys. Lett. **8**, 313-315 (1966).

42. H. Komine, W.H.J. Long, J.W. Tully, and E.A. Stappaerts, "Quasi-phase-matched second-harmonic generation by use of a total-internal-reflection phase shift in gallium arsenide and zinc selenide plates," Opt. Lett. **23**, 661-663 (1998).

43. J.A. Armstrong, N. Bloembergen, J. Ducuing, and P.S. Pershan, "Interactions between light waves in a nonlinear dielectric," Phys. Rev. **127**, 1918-1939 (1962).

44. M.J. Angell, R.M. Emerson, J.L. Hoyt, J.F. Gibbons, L.A. Eyres, M.L. Bortz, and M.M. Fejer, "Growth of alternating <100>/<111>-oriented II-VI regions for quasi-phase-matched nonlinear optical devices on GaAs substrates," Appl. Phys. Lett. **64**, 3107-3109 (1993).

45. S.J.B. Yoo, R. Bhat, C. Caneau, and M.A. Koza, "Quasi-phase-matched second-harmonic generation in AlGaAs waveguides with periodic domain inversion achieved by wafer-bonding," Appl. Phys. Lett. **66**, 3410-3412 (1995).

46. C.Q. Xu, K. Takemasa, K. Nakamura, K. Shinozaki, H. Okayama, and T. Kamijoh, "Device length dependence of optical second-harmonic generation in AlGaAs quasiphase matched waveguides," Appl. Phys. Lett. **70**, 1554-1556 (1997).

47. S. Koh, T. Kondo, T. Ishiwada, C. Iwamoto, H. Ichinose, H. Yaguchi, T. Usami, Y. Shiraki, and R. Ito, "Sublattice reversal in GaAs/Si/GaAs (100) heterostructures by molecular beam epitaxy," Jpn. J. Appl. Phys. **37**, L1493-L1496 (1998).

48. S. Koh, T. Kondo, M. Ebihara, T. Ishiwada, H. Sawada, H. Ichinose, I. Shoji, and R. Ito, "GaAs/Ge/GaAs sublattice reversal epitaxy on GaAs (100) and (111) substrates for nonlinear optical devices," Jpn. J. Appl. Phys. **38**, L508-L511 (1999).

CHAPTER 2: Theory of Nonlinear Optical Frequency Conversion

This chapter presents the theoretical background necessary for predicting the efficiencies of waveguide and bulk nonlinear optical devices in orientation-patterned GaAs. Nonlinear optical frequency conversion is already theoretically well-developed, so I include only the basics for the non-specialist reader, while pointing those interested to widely available detailed derivations [1, 2]. Throughout the chapter I attempt to point out the important approximations to make clear the limitations on the utility of the expressions. Topics which have more specific application to nonlinear optical devices in semiconductors, such as symmetry properties of the nonlinear susceptibilities and overlaps in 4-layer planar waveguides, will be examined in more detail.

The first section begins with presentation of the coupled mode equations and nonlinear polarization, from which the topics of nonlinear coupling, quasiphasematching, and attenuation losses emerge straightforwardly. This is followed by an examination of frequency conversion in waveguide devices and the mode overlap integrals required to calculate their efficiencies. The last section analyzes the conversion efficiencies of bulk-focused devices, including difference frequency generation and harmonic generation. Discussion of high peak and average power devices such as OPOs, where nonidealities like optical damage or two-photon absorption may be limitations, is postponed until chapter 6.

2.1 Plane wave frequency conversion

Employment of plane wave beams in our basic derivation will allow investigation of the nonlinear optical phenomena and important topics such as phasematching and attenuation without complications due to focusing and associated effects. This restriction will be relaxed as necessary in the following sections to allow estimation of conversion efficiencies for realistic NLO devices.

2.1.1 Coupled equations

To model frequency conversion mediated through the nonlinear polarization, one can derive from Maxwell's equations and the constutitive relations a differential equation coupling the electric field at frequency ω_m in a medium and a nonlinear polarization radiating at the same fre-

quency. The Fourier amplitude of the electric field at frequency ω_m can be expressed according to

$$\boldsymbol{E}_m(z) = E_m(z)\exp(-ik_m z), \tag{2.1}$$

where the envelope E_m is a function of z. With use of the slowly-varying envelope approximation, which assumes that the envelope magnitude varies only over lengths much greater than the wavelength, the coupling equation is

$$\frac{d}{dz}E_m(z) = i\frac{\omega_m^2\mu_0}{2k_m}\boldsymbol{P}^{NL}\exp(ik_m z), \tag{2.2}$$

where $\boldsymbol{P}^{NL}$ is the nonlinear polarization induced in the medium at frequency ω_m. The second order nonlinear polarization components can be expressed using the d-tensor formalism as products of the electric fields at two other frequencies constrained by $\omega_3 = \omega_2 + \omega_1$

$$\boldsymbol{P}_1^{NL} = 2\varepsilon_0 d_{eff}\boldsymbol{E}_3\boldsymbol{E}_2^* \tag{2.3a}$$

$$\boldsymbol{P}_2^{NL} = 2\varepsilon_0 d_{eff}\boldsymbol{E}_3\boldsymbol{E}_1^* \tag{2.3b}$$

$$\boldsymbol{P}_3^{NL} = 2\varepsilon_0 d_{eff}\boldsymbol{E}_1\boldsymbol{E}_2 \tag{2.3c}$$

where d_{eff} is the effective nonlinear susceptibility taking account of crystal symmetry, polarization configuration, and phasematching technique. Using these nonlinear polarizations one can write a set of three coupled equations which describe completely the evolution of the coupled plane-wave frequency components through the nonlinear medium

$$\frac{d}{dz}E_1(z) = i\frac{\omega_1 d_{eff}}{n_1 c}E_3(z)E_2(z)^*\exp(-i\Delta k z) \tag{2.4a}$$

$$\frac{d}{dz}E_2(z) = i\frac{\omega_2 d_{eff}}{n_2 c}E_3(z)E_1(z)^*\exp(-i\Delta k z) \tag{2.4b}$$

$$\frac{d}{dz}E_3(z) = i\frac{\omega_3 d_{eff}}{n_3 c}E_2(z)E_1(z)\exp(i\Delta k z) \tag{2.4c}$$

where the wave vector mismatch is defined as

$$\Delta k = (k_3 - k_2 - k_1) = 2\pi\left(\frac{n_3}{\lambda_3} - \frac{n_2}{\lambda_2} - \frac{n_1}{\lambda_1}\right), \tag{2.5}$$

n_j is the refractive index and λ_j is the wavelength. It is clear from the coupled equations that the derivatives will oscillate rapidly in phase with z and result in negligible change in the envelope magnitudes and low conversion efficiency unless the wave vector mismatch is somehow compensated. One can gain an idea of the effective lengths utilizable in the presence of residual phase mismatch by examining the coherence length $L_c = \pi/(\Delta k)$. For unphasematched GaAs devices

this ranges between L_c = 4 μm for 1 μm-pumped parametric amplification and L_c = 100 μm for harmonic generation of 10-μm radiation

2.1.2 Conversion efficiency

From the solutions to the coupled equations one can predict conversion efficiencies and gain in various nonlinear optical devices. Depending on the configuration, one or more of the fields can often be assumed invariant through the crystal, the so-called "undepleted-pump approximation", which greatly simplifies the analysis. For the case of sum frequency mixing, the pump fields E_1 and E_2 are taken to be constant, which allows direct integration of Equation 2.4c over the length of the nonlinear medium of length L to obtain

$$I_3 = \frac{8\pi^2 d_{eff}^2}{n_1 n_2 n_3 c\varepsilon_0 \lambda_3^2} I_2 I_1 \mathrm{sinc}^2\left[\frac{\Delta kL}{2}\right] L^2, \tag{2.6}$$

where $I = nc\varepsilon_0|E|^2/2$. For plane waves the conversion scales with the square of interaction length provided the residual phase mismatch is sufficiently small. For the specific case of second harmonic generation, the nonlinear polarization is defined as $\boldsymbol{P}^{NL} = \varepsilon_0 d_{eff} \boldsymbol{E}_\omega^2$, rather than as in equation 2.3c, in order to allow use of the same nonlinear coefficient as the other processes and (at least in principle) minimize confusion. In that case equation 2.6 still applies, but the sum frequency wavelength λ_3 should be replaced directly by the fundamental wavelength λ_f to cancel properly all the factors of 2 associated with the different polarization definition. For difference frequency generation with two undepleted pump waves, the similarity of the coupled equations makes possible the use of equation 2.6 to calculate the efficiency provided the wavelength λ_3 is replaced by the wavelength of the generated difference frequency λ_{DFG}.

For prediction of device performance, the spatial overlap of the nonlinear polarization and the effects of diffraction must be taken into account to convert properly these intensity expressions into power expressions. If the transverse beam profiles are assumed to be Gaussian so that

$$E_j \propto \exp\left(-\frac{r^2}{w_j^2}\right) \tag{2.7}$$

we can define an effective area for each beam $A_j = \pi w_j^2/2$ so that the peak intensity and power are related by $P_j = I_{0j} A_j$. The waists of the induced nonlinear polarization and input beams are related by

$$\frac{1}{\overline{w_3^2}} = \frac{1}{w_1^2} + \frac{1}{w_2^2} \tag{2.8}$$

where the bar indicates the waist is that of a nonlinear polarization. In the near-field approximation where diffraction can be ignored, one assumes that the beam radiated from the nonlinear polarization has the same waist size as the nonlinear polarization itself. Integration over the assumed Gaussian transverse dependence of each beam and the nonlinear polarization yields an expression for sum frequency power

$$P_3 = \eta P_1 P_2 \mathrm{sinc}^2\left[\frac{\Delta kL}{2}\right] L^2, \tag{2.9}$$

where the normalized efficiency has units of Watts/cm^2 and is defined as

$$\eta = \frac{8\pi^2 d_{eff}^2}{n_1 n_2 n_3 c\varepsilon_0 \lambda_3^2 A_{NF}} \tag{2.10}$$

and the effective area in this near-field approximation is

$$A_{NF} = \pi\frac{(w_1^{\,2} + w_2^{\,2})}{2}. \tag{2.11}$$

This effective area quantifies the magnitude of the coupling between the nonlinear polarization and the radiation at ω_3. Corresponding expressions for SHG and DFG efficiencies can be found by consistently permuting the frequency indices and properly substituting for the wavelength factor in equation 2.10, as discussed above. Thus, the efficiency increases as the mode sizes of the pump waves decrease as long as the near-field approximation remains valid. This near field approximation will break down when any one of the beam waists becomes small enough that diffraction effects are no longer negligible, something which is clearly most likely to occur with the longest wavelength beam.

2.1.3 Polarization and effective nonlinearity

The zincblende semiconductors belong to symmetry group $\bar{4}3m$, where the $\bar{4}$ symmetry axis is <100>. The $\bar{4}3m$ symmetry group requires that d_{14}, d_{25} and d_{36} (all having equal magnitudes) be the only nonzero elements of the reduced second order nonlinear susceptibility tensor. The majority of GaAs material research, device fabrication, and all of the work described in this dissertation has been performed on GaAs wafers polished on or close to (001). This combination of symmetry and wafer orientation constrains the useful polarization and propagation propagation directions for nonlinear optical frequency conversion.

The use of (001) wafers for our orientation-patterned growth requires that the optical k-vectors must lie in or approximately (modulo the wafer misorientation) in (001) in order to achieve long propagation lengths and high efficiencies, both for bulk and waveguide geometries. The three nonlinear polarization components for frequency mixing in this crystal symmetry are

$$\boldsymbol{P}_x^{(2)}(\omega_3) = 2\varepsilon_0 d_{14}[\boldsymbol{E}_y(\omega_1)\boldsymbol{E}_z(\omega_2) + \boldsymbol{E}_z(\omega_1)\boldsymbol{E}_y(\omega_2)] \tag{2.12a}$$

$$\boldsymbol{P}_y^{(2)}(\omega_3) = 2\varepsilon_0 d_{14}[\boldsymbol{E}_x(\omega_1)\boldsymbol{E}_z(\omega_2) + \boldsymbol{E}_z(\omega_1)\boldsymbol{E}_y(\omega_2)] \tag{2.12b}$$

$$\boldsymbol{P}_z^{(2)}(\omega_3) = 2\varepsilon_0 d_{14}[\boldsymbol{E}_x(\omega_1)\boldsymbol{E}_y(\omega_2) + \boldsymbol{E}_y(\omega_1)\boldsymbol{E}_x(\omega_2)]\,. \tag{2.12c}$$

where $\omega_3 = \omega_2 \pm \omega_1$ and the notation $\boldsymbol{E}_x(\omega_1)$ here indicates the Fourier amplitude of the electric field at frequency ω_1 polarized along the x direction. It is clear immediately that the combination of input and output wave polarizations must have some projection along all of the x, y and z axes in order for the effective nonlinearity to be nonzero. To explore the effects of propagation direction and polarization on the effective nonlinearity, we define a set of angles according to the diagram in Figure 2.1. Here ϕ is defined as the angle in the (001) plane between the k-vector and the

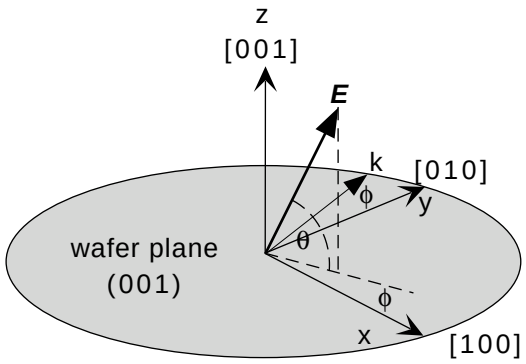

Figure 2.1: Reference angles used for calculation of GaAs effective nonlinear susceptibilities.

y-axis [010], so that the electric field vector lies in the x-z plane when $\phi = 0$. θ_1 and θ_2 are defined as the angles between the (001) plane and the electric field vector at frequency ω_1 and ω_2, respectively, as illustrated in Figure 2.1. Thus, when $\theta = \phi = 0$, the electric field vector lies along the x-axis. Using these variables we can write the nonlinear polarizations as

$$\boldsymbol{P}_x^{(2)}(\omega_3) = 2\varepsilon_0 d_{14}\sin\phi\hat{\boldsymbol{x}}[\cos\theta_1\sin\theta_2 + \cos\theta_2\sin\theta_1]E_{\omega_1}E_{\omega_2} \tag{2.13}$$

$$\boldsymbol{P}_y^{(2)}(\omega_3) = 2\varepsilon_0 d_{14}\cos\phi\hat{\boldsymbol{y}}[\cos\theta_1\sin\theta_2 + \cos\theta_2\sin\theta_1]E_{\omega_1}E_{\omega_2} \tag{2.14}$$

$$\boldsymbol{P}_z^{(2)}(\omega_3) = 4\varepsilon_0 d_{14}\cos\phi\sin\phi\hat{\boldsymbol{z}}[\cos\theta_1\cos\theta_2]E_{\omega_1}E_{\omega_2} \tag{2.15}$$

where E_{ω_j} represents the amplitude of the electric field at frequency ω_j. If we define ψ to be the angle in the {001} plane between the induced nonlinear polarization vector and the x-axis (similar to ϕ), we find that

$$\psi = \text{atan}\left(\frac{\boldsymbol{P}_y^{(2)}(\omega_3)}{\boldsymbol{P}_x^{(2)}(\omega_3)}\right) = \text{atan}\left(\frac{\cos\phi}{\sin\phi}\right), \tag{2.16}$$

so that the induced polarization is not in general normal to the direction of optical propagation. Restricting ourselves, therefore, to the most useful case of collinear propagation for all three waves, we can write magnitude of the polarization in the x-y plane orthogonal to the k-vector as

$$\left|\boldsymbol{P}_{xy}^{(2)}(\omega_3)\right| = 4\varepsilon_0 d_{14}\cos\phi\sin\phi[\cos\theta_1\sin\theta_2 + \cos\theta_2\sin\theta_1]E_{\omega_1}E_{\omega_2}. \tag{2.17}$$

For optimum nonlinearity one must clearly choose $\phi = \pi/4$, which corresponds to optical propagation along <110>. GaAs also cleaves easily in {110}, which means that optimal nonlinear devices can have high-quality, easily fabricated, normal incidence endfacets. Assuming this optimal propagation angle we can write the magnitude of the nonlinear polarization as

$$P_{mag}^{(2)}(\omega_3) = 2\varepsilon_0 d_{14}[(\sin\theta_1\cos\theta_2 + \cos\theta_1\sin\theta_2)^2 + (\cos\theta_1\cos\theta_2)^2]^{1/2} \tag{2.18}$$

and the nonlinear polarization angle θ_p with respect to the wafer plane as

$$\theta_p = \text{atan}\left(\frac{\cos\theta_1\cos\theta_2}{\cos\theta_1\sin\theta_2 + \cos\theta_2\sin\theta_1}\right) \quad . \tag{2.19}$$

From the three terms in equation 2.18 we can discern two different pure polarization configurations. The first two terms correspond to the case in which the polarizations of the two input waves are orthogonal, with one in the wafer plane and the other normal to the wafer plane. In this case the nonlinear polarization is aligned in the wafer plane. The third term in equation 2.18 corresponds to the case in which both input waves are polarized in the wafer plane and the nonlinear polarization is normal to the wafer plane. In all of these geometries the effective nonlinearity is simply $d_{eff} = d_{14}$. Note that if one of the input waves is aligned in the plane, the effective nonlinearity is then independent of the polarization state of the other input wave, allowing the polarization-independent frequency conversion desirable for WDM wavelength conversion applications.

In addition to these type-II configurations, one can also find an optimal type-I configuration. If we maximize equation 2.18 under the condition that $\theta_1 = \theta_2$ by setting the derivative

with respect to θ equal to zero, we find that $\theta_3 = \theta_1 = \theta_2 = 35.26°$, which corresponds to alignment of all polarizations along <111>. The effective nonlinearity obtained in this case is

$$d_{eff} = \frac{2}{\sqrt{3}} d_{14}, \tag{2.20}$$

which is the maximum obtainable from a material with this symmetry.

2.1.4 Quasiphasematching

As some dispersion of the refractive indices is present in all materials, in general $\Delta k \neq 0$ and high conversion efficiencies are achieveable only by employing some phasematching technique. In birefringent crystals, propagation directions and polarization states can be selected so that the wave-vector mismatch vanishes, but this is only true for a limited number of materials and even then often over only limited wavelength ranges. Quasiphasematching provides a more flexible techique for obtaining phasematching provided some technique can be found for fabricating the materials. In a quasiphasematched interaction, the magnitude and/or sign of effective nonlinearity is modulated periodically along the propagation direction of the radiation and can be expressed as a Fourier series

$$d(z) = d_{eff} \sum_{m=-\infty}^{m=\infty} G_m \exp(-iK_m z) \tag{2.21}$$

where the grating vector is defined as $K_m = 2\pi m/\Lambda$ and the Λ is the period of the modulation. If the sign of the susceptibility is modulated, the amplitude of the mth Fourier coefficient is

$$G_m = \frac{2}{m\pi} \sin(m\pi D) \tag{2.22}$$

where D is the duty cycle ($0 < D < 1$) of the reversed domains. The maximum nonlinearity is obtained with lowest-order quasiphasematching (m = 1), and equal length domains ($D = 1/2$)

$$d_{QPM} = \frac{2}{\pi} d_{eff}. \tag{2.23}$$

Inserting this definition of the nonlinearity from equation 2.23 into equation 2.4c and following through the same derivation as Section 2.12 gives

$$P_3 = \eta_{QPM} P_1 P_2 L^2 \operatorname{sinc}^2\left[\frac{(\Delta k - K_m)L}{2}\right] \tag{2.24}$$

where $\eta_{QPM} = \eta(2/\pi)^2$. Addition of the proper nonlinear susceptibility modulation thus makes possible compensation of the dispersion and wave vector mismatch for any desired frequency con-

version process by simple adjustment of the modulation period. Where previously the wave vector mismatch limited the effective interaction length to the 4 μm - 100 μm range, with the quasiphase-matching grating the device length can be arbitrarily long. Devices having interaction lengths > 5 cm have been demonstrated in PPLN and other materials. The reduction in the prefactor by $(2/\pi)^2$ for this quasiphasematched interaction is a small price to pay for the many orders of magnitude increase in effective length and the much higher efficiency it enables.

2.1.5 Attenuation effects

The presence of attenuation at one or more wavelengths will reduce the conversion efficiencies and modify the tuning behavior of a nonlinear optical device. The functional similarity of the coupled equations for the planar wavefront case and the waveguide case will allow us to derive a single correction factor for the conversion efficiency in the presence of loss that applies to both cases. With power losses of α_1, α_2, and α_3 at wavelengths λ_1, λ_2, and λ_3, respectively, the coupled equations 2.4 are transformed into the form

$$\frac{dE_3}{dz} + \frac{\alpha_3}{2}E_3 = i\frac{\omega_3 d_{eff}}{n_3 c}E_2 E_1 \exp\left[i(\Delta k - K_m)z - \frac{(\alpha_1 + \alpha_2)}{2}z\right]. \tag{2.25}$$

Solution of this equation yields a significantly more complicated expression for the efficiency and tuning behavior. Comparing the lossy device with a lossless device, we can define an efficiency reduction factor $\gamma = P_{lossy}/P_{lossless}$. Examining only the phasematched case and defining $\alpha' = \alpha_1 + \alpha_2 - \alpha_3$, one finds this efficiency reduction factor to be

$$\gamma = \frac{\exp(-\alpha_3 L)[\exp(-\alpha' L) - 1]^2}{\alpha'^2 L^2}. \tag{2.26}$$

For devices with losses at only α_3, or some combination $\alpha_1 + \alpha_2$, the output power saturates with length as the numerator is approximately 1 and the L^2 factor in the denominator cancels the parabolic gain in the lossless expression. With losses at all wavelengths, the converted power will exhibit a maximum at a particular crystal length and then decrease for longer crystals. Attenuation losses thus limit the useable crystal lengths and therefore the obtainable efficiencies from a particular material or device. The effects on tuning behavior can be calculated from the solution of equation 2.25 and will affect the tuning behavior primarily around $|\sin x/x| \to 0$. Note that for the special condition of $\alpha' = 0$, the efficiency is simply multipled by the attenuation factor $\exp(-\alpha_3 L)$, as can be seen by expanding the quantity in square brackets as a Taylor series.

2.2 Frequency conversion in waveguides

This section will develop the expressions necessary to predict the efficiency of frequency conversion in semiconductor waveguides, then examine some interesting device examples. Waveguide modes and nonlinear optics in waveguides have been investigated extensively, so I will present only the parts of the derivation necessary to be internally consistent and to outline the approximations employed, directing those interested to more detailed treatments [3-5]. The chapter starts with a brief overview of waveguide mode properties, then develops effective areas which properly account for the transverse mode overlap of the nonlinear polarization and radiated mode. Nondimensional solutions for 1-dimensional planar waveguides with four layers are developed and these are used to find nondimensional overlap integrals, which are used in turn to caluculate the efficiencies of waveguide NLO devices.

2.2.1 Mode normalization

The stable modes of a dielectric waveguide structure propagate like plane waves, but their transverse beam properties are set by the boundary conditions on the electric and magnetic fields rather than by simple diffraction. Such a waveguide has a discrete spectrum of modes which are orthonormal and which have differing transverse electric and magnetic field dependences. While a waveguide may support many modes at a particular wavelength, for nonlinear optical frequency conversion one is almost always interested in conversion to and from a single transverse mode at each wavelength, both because this yields the highest efficiencies and because modal dispersion usually insures that only one combination will be phasematched at a time. Additionally, since we are considering collinear frequency conversion, we include only the forward propagating waves, though the formalism can easily be extended to include non-collinear interactions such as the backward OPO.

One can write the electric and magnetic fields of a guided mode propagating without change in amplitude as

$$\boldsymbol{E}_\nu(x,y,z) = \vec{E}_\nu(x,y)\exp(-i\beta z) \tag{2.27a}$$

$$\boldsymbol{H}_\nu(x,y,z) = \vec{H}_\nu(x,y)\exp(-i\beta z) \tag{2.27b}$$

where $\beta = 2\pi n_\nu/\lambda$ and the modal index is n_ν. These modes exhibit the following orthonormalization relationship,

$$\frac{1}{2}\int_{-\infty}^{\infty}\int \mathrm{Re}[\vec{E}_\nu(x,y)\times\vec{H}_\mu{}^*(x,y)]\cdot\hat{z}\,dx\,dy = \delta_{\nu\mu}P_\nu, \tag{2.28}$$

where P_ν is the power carried by the mode. For many waveguides used in nonlinear optics, one can make the "weak-guidance" approximation, in which the z-components of the fields are neglected and one considers only the transverse components. In this approximation the electric and magnetic components of a particular mode are proportional and related by

$$\tilde{H}_\nu(x,y) \approx \sqrt{\frac{\varepsilon_0}{\mu_0}} n_\nu \hat{z} \times \tilde{E}_\nu(x,y). \tag{2.29}$$

This approximation allows the definition of a simpler scalar normalization which depends only on the modal electric field and which is extremely convenient for nonlinear optical calculations

$$\int_{-\infty}^{\infty} \tilde{E}_\nu(x,y)\tilde{E}_\mu(x,y)dxdy = \delta_{\nu\mu}. \tag{2.30}$$

The modal electric field can then be written as the product of a complex amplitude, a z-independent normalized transverse field profile, and a rapidly varying phase factor

$$\boldsymbol{E}_\nu(x,y,z) = \boldsymbol{A}_\nu \tilde{E}_\nu(x,y)\exp(i\beta z), \tag{2.31}$$

so that the power carried by the mode is

$$P_\nu = \frac{n_\nu \varepsilon_0 c}{2}|\boldsymbol{A}_\nu|^2. \tag{2.32}$$

This mode normalization will be assumed for all subsequent waveguide calculations in this dissertation. In the next section, the factor $\boldsymbol{A}_\nu$ will be allowed to vary with z to derive a set of coupled equations for the mode amplitudes.

Accurate solutions of 2-dimensional mode profiles typically requires numerical evaluation of the modal propagation constants and field profiles. A variety of methods are used to find the eigenvectors and values, including finite difference [6, 7] (and references therein), finite element [8], and beam propagation techniques [3]. For semiconductor waveguides, these methods require taking account of the exact structure formed by the particular lateral confinement technique used, whether an etched rib, or a regrown buried heterostructure. We used a 2-D finite difference algorithm to compute mode indices and transverse profiles for our devices; the specific implementation will be discussed in Chapter 4 along with the device design issues.

For some waveguides one can approximate the modes as being separable, so that

$$\tilde{E}_\nu(x,y) \approx \tilde{E}_{\nu x}(x)\tilde{E}_{\nu y}(y) \tag{2.33}$$

and the normalization becomes

$$\int_{-\infty}^{\infty} \tilde{E}_{\nu x}(x)\tilde{E}_{\mu x}(x)dx \;=\; \int_{-\infty}^{\infty} \tilde{E}_{\nu y}(y)\tilde{E}_{\mu y}(y)dy \;=\; \delta_{\nu\mu}\,. \tag{2.34}$$

This approximation, of which the effective index method [9, 10] is an example, provides a simpler though less accurate technique for estimating the transverse modal profiles, since the two-dimensional problem reduces to two separate one-dimensional problems.

2.2.2 Efficiency and effective area

If one allows the modes at each frequency to have a slowly varying envelope $\boldsymbol{A}_\nu(z)$ in the z direction in a manner similar to that used for plane waves in Section 2.1.1

$$\boldsymbol{E}_\nu(x,y,z) \;=\; \tilde{E}_\nu(x,y)\boldsymbol{A}_\nu(z)\exp(-i\beta z)\,, \tag{2.35}$$

one can write a set of coupled equations for the $\boldsymbol{A}_j(z)$ s which have the same functional form as those developed for plane waves. The efficiency of a waveguide sum frequency generation device can therefore be written as

$$P_3 \;=\; \eta_{wg}P_1(0)P_2(0)L^2\mathrm{sinc}^2\left[\frac{(\Delta\beta - K_m)L}{2}\right] \tag{2.36}$$

and the normalized efficiency η_{wg} has the same factors as in the previous section

$$\eta_{wg} \;=\; \frac{8\pi^2 d_{eff}^2}{n_1 n_2 n_3 c\varepsilon_0 \lambda_3^2 A_{eff}}\,. \tag{2.37}$$

To move from sum frequency generation to harmonic generation and difference frequency generation one must simply replace λ_3 with either λ_f or λ_{DFG} as discussed above in Section 2.1.2 to obtain the proper normalized efficiency. The different factor A_{eff} still has units of area and is defined as

$$A_{eff} \;=\; \vartheta^{-2} \;=\; \left|\int_{-\infty}^{\infty}\int \tilde{E}_1(x,y)\tilde{E}_2(x,y)\tilde{E}_3(x,y)dxdy\right|^{-2}\,. \tag{2.38}$$

This effective area quantifies the physical size of the waveguide and magnitude of the coupling between the nonlinear polarization and the waveguide mode at the generated frequency, being equivalent to the area of the top-hat modes which would have the same conversion efficiency. Thus, the calculation of efficiencies for collinear guided-wave nonlinear interactions reduces to the calculation of the relevant overlap integrals, which will be investigated in more detail for specialized cases in the following section. Under the assumption that the waveguide modes are sepa-

rable, one can write the overlap integral as the product of separate 1-dimensional overlap integrals in each transverse dimension $\vartheta = \vartheta_x \vartheta_y$, where

$$\vartheta_x = \int_{-\infty}^{\infty} \tilde{E}_{1x}(x)\tilde{E}_{2x}(x)\tilde{E}_{3x}(x)dx \tag{2.39}$$

$$\vartheta_y = \int_{-\infty}^{\infty} \tilde{E}_{1y}(y)\tilde{E}_{2y}(y)\tilde{E}_{3y}(y)dy \ . \tag{2.40}$$

2.2.3 One-dimensional slab waveguides

In this section we find the normalized modes of a 4-layer planar waveguide structure, since this strucuture is typical of those fabricable in semiconductor materials. We follow the approach of Kogelnik and Ramaswamy [11] using normalized mode parameters, but extend this to a four layer structure with a top cladding between the waveguide core and air. Determination of these four-layer mode solutions makes possible computation of the normalized overlap integrals in the following section, which in turn allows easy estimation of the potential efficiencies obtainable for various interesting NLO waveguide devices. Only the TE modes of the structure are investigated here. The TM mode solutions can also be found, but use of the weak guidance approximation in calculating overlap integrals eliminates the distinction between the transverse dependence of the TE and TM modes.

The four layer planar dielectric structure to be analyzed is shown in Figure 2.2. We constrain the index and composition of the top cladding layer to be same as the lower cladding underneath the core. This constraint allows exploration into the impact of the top cladding layer while adding only one additional parameter. Additionally, this is a particularly suitable structure for growth by molecular beam epitaxy, since the few effusion sources (typically two Ga and one Al sources) can only be modulated on/off and therefore only a limited number of compositions can be grown without ramping the source temperatures during a growth run.

In accordance with the normalized approach, we define normalized coordinates to make the conclusions independent of the dimension and wavelength of the devices. Taking the core width ρ as the characteristic dimension of the waveguide in the x direction, one can define

$$X = x/\rho \, . \tag{2.41}$$

The one-dimensional transverse field profiles are then normalized according to

air		$n = 1$
top cladding	l	n_s
core	ρ	n_f
bottom cladding		n_s

Figure 2.2: Four-layer dielectric waveguide structure.

$$\int_{-\infty}^{\infty} \left|\tilde{E}_v(X)\right|^2 dX = 1. \tag{2.42}$$

With the vacuum wave vector defined as

$$k_o = \frac{2\pi}{\lambda} \tag{2.43}$$

one can define a set of normalized waveguide parameters based on the waveguide structure showing in Figure 2.2

$$V = k_o \rho (n_f^2 - n_s^2)^{1/2} \tag{2.44}$$

$$a = (n_s^2 - 1)/(n_f^2 - n_s^2) \tag{2.45}$$

$$b = (N^2 - n_s^2)/(n_f^2 - n_s^2) \tag{2.46}$$

$$w = \frac{l}{\rho} \tag{2.47}$$

where V is the normalized frequency, a is the normalized asymmetry, b is the normalized mode index ($0<b<1$), and w is the normalized top cladding width $0 \le w \le \infty$. Solving for the dispersion relation in terms of the normalized variables yields

$$V\sqrt{1-b} = v\pi + \operatorname{atan}\sqrt{\frac{b}{1-b}} + \operatorname{atan}\left(\sqrt{\frac{b}{1-b}}\left[\frac{\sinh(Vw\sqrt{b}) + \sqrt{\frac{(b+a)}{b}}\cosh(Vw\sqrt{b})}{\cosh(Vw\sqrt{b}) + \sqrt{\frac{(b+a)}{b}}\sinh(Vw\sqrt{b})}\right]\right), \tag{2.48}$$

which reduces in the limit of $w \to 0$ to the dispersion relation for the asymmetric 3-layer slab waveguide and reduces in the limit of $w \to \infty$ to the dispersion relation for the symmetric 3-layer slab waveguide.

While this dispersion relation for the 4-layer waveguide is more complicated than that of the 3-layer case, it can easily be solved numerically. Figure 2.3 shows the normalized mode index

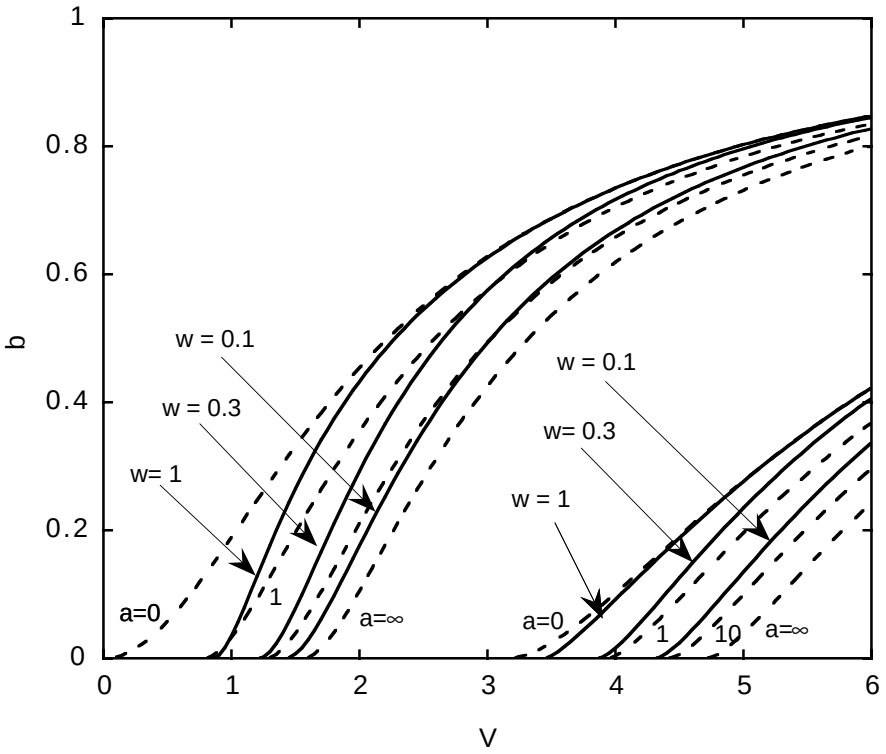

Figure 2.3: Normalized ω–β diagrams for three and four layer planar waveguides. The dashed curves are those of [12] for three-layers waveguides plotted for the two lowest order modes with asymmetries of 0, 1, 10 and ∞. The solid lines are for four-layer waveguides of infinite asymmetry but having normalized top cladding thicknesses of 0.1, 0.3, and 1.

as a function of normalized confinement for various asymmetry and top cladding combinations. The dashed curves show the classic solutions for various asymmetries without any top cladding included in [11], while the solid curves show a waveguide with infinite asymmetry, but including top cladding layers of varying normalized widths. Typical asymmetries for waveguides in AlGaAs range between 5 and 40. Addition of a top cladding layer of equal thickness to the core results in a mode index approximately equal to that of a symmetric waveguide for normalized confinements greater than $V = 2$. One can see that even relatively thin top cladding layers significantly decrease the asymmetry and raise the mode index.

2.2.4 Mode overlaps of four-layer planar waveguides

This section presents one-dimensional overlap integrals for the normalized 4-layer waveguides of the last section which can be used for the calculation of the conversion efficiencies, as developed in Section 2.2.2. In general, this normalized overlap is a function of the waveguide

parameters, the three wavelengths of interest, as well as the dispersion of the materials between those wavelengths. We expand the analysis of Lim, et al[5, 13], who investigated symmetric and asymmetric 3-layer structures for harmonic generation, by extending here the analysis to 4-layers and arbitrary frequency interactions. Following Lim, et al [5, 13] we can define a dispersion parameter r_{ij} between λ_i and λ_j as

$$r_{ij} = \frac{(n_f^2 - n_s^2)_i}{(n_f^2 - n_s^2)_j} \tag{2.49}$$

and a non-degeneracy parameter δ which relates the various wavelengths λ_1, λ_2, and λ_3 according to

$$\frac{\lambda_1}{\lambda_3} = \frac{2}{1-\delta} \text{ and } \frac{\lambda_2}{\lambda_3} = \frac{2}{1+\delta} \tag{2.50}$$

where $|\delta| < 1$. Using these we can then express the normalized confinement at the three wavelengths as

$$V_1 = V_3\left(\frac{1-\delta}{2}\right)\sqrt{r_{13}} \text{ and } V_2 = V_3\left(\frac{1+\delta}{2}\right)\sqrt{r_{23}} \tag{2.51}$$

which can be inverted to yield

$$V_2 = \left(\frac{1+\delta}{1-\delta}\right)\sqrt{\frac{r_{23}}{r_{13}}}V_1 \quad \text{and } V_3 = \frac{2}{(1-\delta)\sqrt{r_{13}}}V_1 \tag{2.52}$$

With these definitions and the previous definitions of $\tilde{E}_j$ we can define a normalized depth in one dimension as

$$D_x = \left| \int_{-\infty}^{\infty} \tilde{E}_1(V_1, w, a, \delta, X)\tilde{E}_2(V_1, w, a, \delta, r_{23}, r_{13}, X)\tilde{E}_3(V_1, w, a, \delta, r_{13}, X)\, dX \right|^{-2} \tag{2.53}$$

so that the $1/(D_j\rho_j) = \vartheta_j^2$ Thus, if the transverse mode is assumed to be separable, the effective area can be expressed in terms of the characteristic dimensions as

$$A_{eff} = \rho_x D_x \rho_y D_y . \tag{2.54}$$

D provides a dimensionless parameter which quantifies the overlap of the three modes in the interaction independent of the wavelengths or waveguide dimensions. The expression is written as a function of the normalized confinement at the longest wavelength, V_1, because this mode is closest to cut-off and therefore has the most implications for device design.

More useful for device design is the nondimensional depth parameter (DV_1), because it is proportional to the effective depth $(D\rho)$ for a given core-cladding index difference. Since conversion efficiencies are proportional to the inverse of effective depth, it makes sense to plot the reciprocal $(DV_1)^{-1}$ which is proportional to conversion efficiency and has a maximum at the point of minimum effective depth. Figure 2.4 shows $(DV_1)^{-1}$ as a function of V_1 for the values $w = 0, 1, \infty$, $a = \infty$, and $\delta = 0$. For the semiconductor materials under consideration, the overlaps are relatively weak functions of the dispersion parameters, so we plot the cases where $r_{13} = r_{23} = 1$. The parameter $(DV_1)^{-1}$ exhibits a maximum value corresponding to the optimum 1-D overlap which is relatively constant as a function of top cladding thickness for this degenerate case, though the value of V_1 corresponding to this maximum varies over the transition from asymmetric to symmetric waveguides. The relative insensitivity of this maximum will allow optimization of the waveguide structures for other important factors such as noncriticality or low scattering losses without large sacrifices in conversion efficiency.

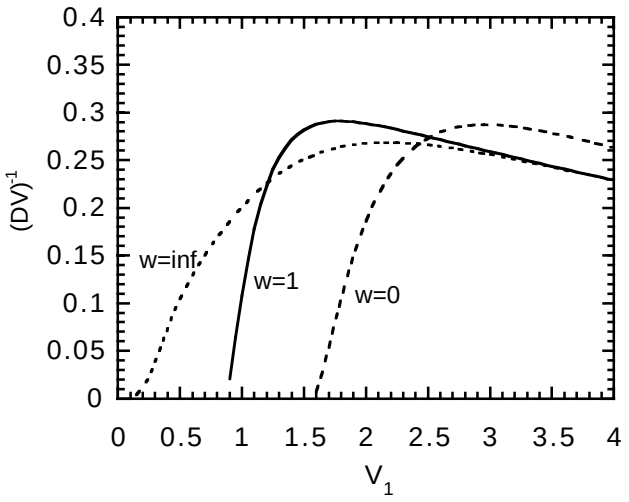

Figure 2.4: Nondimensional depth parameter as a function of normalized frequency and cladding width.

Defining D_{opt} and V_{opt} to be values of D and V_1 associated with this maximum achievable confinement, we can explore the behavior of $(D_{opt}V_{opt})^{-1}$, the optimal normalized depth parameter, as a function of the normalized device parameters. Figure 2.5 shows $(D_{opt}V_{opt})^{-1}$ as a

function of the normalized top cladding thickness w for values of the degeneracy parameter $\delta = 0, 0.3, 0.6, 0.9$.

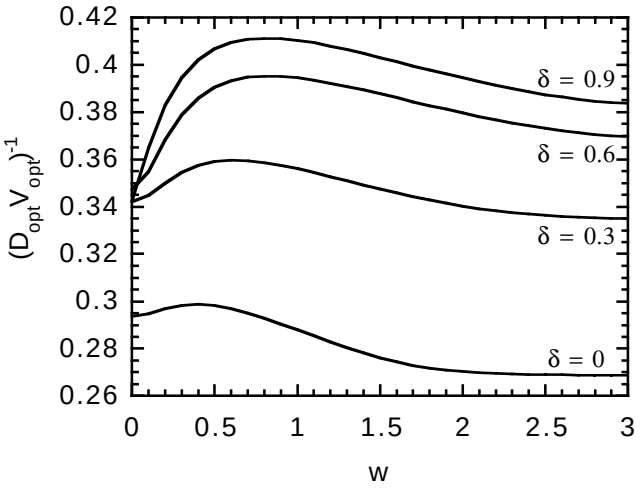

Figure 2.5: Optimal depth parameter as a function of the normalized top cladding width and nondegeneracy.

The figure is plotted for a typical asymmetry of 20 corresponding to $\Delta n_{core-cladding} = 0.15$ and thus an approximately 30% difference in Al fraction for AlGaAs. The magnitude $(D_{opt}V_{opt})^{-1}$ is a strong function of the top cladding width only far from degeneracy and at low cladding widths, where the addition of a thin top cladding makes possible better overlap between the modes at different wavelengths. The highest efficiencies are obtained for normalized top cladding thicknesses of around $w \approx 0.5$, though even in the $\delta = 0.9$ case the increase resulting from addition of the cladding is only about 20%. One can also see from the graph that the dependence of efficiency on the degeneracy parameter is roughly independent of top cladding thickness for normalized cladding thicknesses greater than 0.5. Also, though this is not shown in Figure 2.5, the curves are only weakly dependent on the assumed asymmetry except near $w = 0$; intuitively, most of the variation with asymmetry occurs when the top cladding layers are very thin, since otherwise the top cladding layer determines the mode profiles.

2.2.5 Waveguide NLO device predictions

We can use the predictions of the last section to estimate conversion efficiencies for useful nonlinear optical devices such as difference frequency generators for IR generation. For simplic-

ity, we consider a completely symmetric hetrostructure waveguide in which the core region is surrounded entirely by a uniform refractive index cladding, as shown in Figure 2.6.

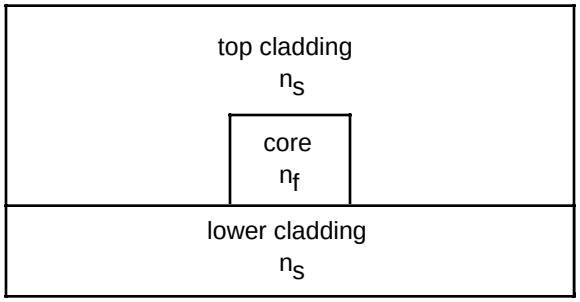

Figure 2.6: Schematic diagram of the buried heterostructure used for waveguide device calculations.

We make the simplifying assumptions that the mode profile is separable in the transverse dimensions and that we can approximate the 2-D overlap by a product of 1-D overlaps, as discussed in the previous sections. The approach of Marcatili [14] approximates the two-dimensional mode of such a buried rectangular waveguide as a product of two one-dimensional waveguide modes, the first satisfying TE boundary conditions in one direction and the other satisfying TM boundary conditions in the orthogonal direction. In the weak guidance approximation, these TE and TM modal profiles are identical, so the waveguide mode can be approximated simply by the product of two one-dimensional modes of the kind developed in section 1.2.3. This allows straightforward use of the normalized formalism and results of the previous section. Assuming the top cladding is sufficiently thick, we can treat the vertical mode as symmetric and use those values for $(D_{opt}V_{opt})^{-1}$ for both the vertical and horizontal modes.

With these approximations, the efficiency for difference frequency generation can be found from equations 2.54, 2.44 and 2.37 to be

$$\eta_{wg}\left[\frac{1}{W \cdot cm^2}\right] = \frac{64\pi^4 d_{eff}^2 \Delta n}{n^2 c\varepsilon_0 \lambda_1^4 (D_{opt}V_{opt})^2} = \frac{7.447\times10^4(\Delta n)}{\lambda_1^4[\mu m](D_{opt}V_{opt})^2} \tag{2.55}$$

for d_{eff} = 57 pm/V and a refractive index of 3.2. The generated wavelength λ_1 is the longest wavelength and the approximation

$$n_f^2 - n_s^2 \approx 2n_s\Delta n \tag{2.56}$$

is assumed valid. From Figure 2.5 one can determine the values of $(D_{opt}V_{opt})^{-1}$ and find an estimated efficiency. The efficiency exhibits an extremely strong wavelength dependence and is lin-

ear in the core-cladding refractive index difference. To make the results independent of wavelength, Figure 2.7 plots the product $\eta_{wg}\lambda_1^4$ as a function of Δn and δ. The efficiency varies by approximately a factor of 2 between the degenerate and highly nondegenerate cases. With pumps in the near-IR, DFG of 10 μm radiation could achieve efficiencies of 0.1 $(W*cm^2)^{-1}$ with Δn = 0.1, which corresponds to a composition difference of approximately 20% Al in AlGaAs. This efficiency would allow generation of 1 mW of 10 μm radiation in a 1 cm long orientation-patterned GaAs waveguide with only 100 mW of pump radiation at each of the pump wavelengths. The same 100 mW could generate 10 μW of output at 10 μm wavelength in only a 1 mm long orientation patterned AlGaAs waveguide, a power level which is still very useful for spectroscopic applications. This means that even relatively high loss AlGaAs waveguide devices such as those characterized in chapter 4 may be useful for mid-IR generation, with their utility increasing as the losses improve with further research. Of course, methods for coupling the pump beams into such highly multi-moded waveguides will need to be developed to achieve these efficiencies, something discussed in more detail in Chapter 4.

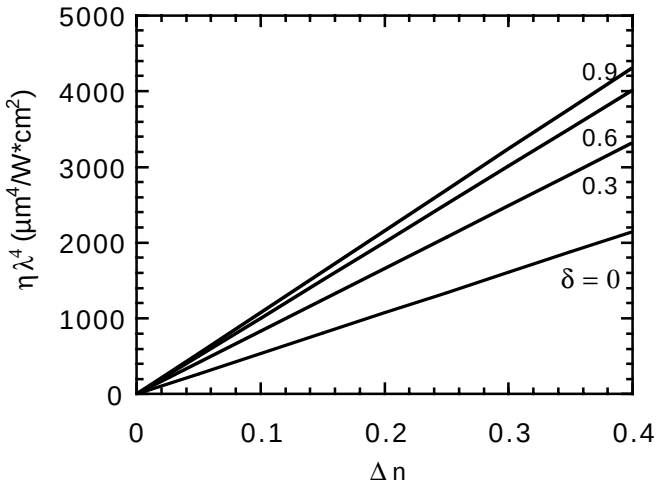

Figure 2.7: DFG efficiency for AlGaAs waveguides as a function of core-cladding confinement.

Optical parametric oscillators could also be developed in these waveguides, but the high propagation losses measured to date at near-IR pump wavelengths have been too large to consider this as a realistic possibility. However, future advances in lowering attenuation losses could make this an attractive option for achieving high conversion efficiencies.

2.3 Bulk single-pass NLO CW devices

In this section we extend the expressions derived for plane wave frequency conversion to realistic devices and predict GaAs device performance for low power applications. The section begins with calculation of the performance of difference frequency generation devices, then briefly outlines harmonic generation for comparison with our experimental results in Chapter 5. Discussion of OPOs and other high power devices will be delayed until Chapter 6, which will investigate the limitations on high-peak-power and high-average-power devices.

2.3.1 Difference frequency generation

To estimate the conversion efficiencies obtainable in GaAs for mid-IR generation, we can use equations 2.8, 2.9, and 2.10 and make some reasonable assumptions regarding the beam sizes. If we assume that the generated DFG wavelength is much larger than either of the pump wavelengths, diffraction will affect the long wavelength beam under conditions for which the other two beams remain within their near field limits. As the pump beams are focused more and more tightly, the radiated idler beam will begin to diffract away rapidly from the driving idler polarization region and the efficiency and beam quality will be compromised. We can estimate the conversion efficiency of a DFG device producing a good quality idler beam by setting the generated idler polarization to be confocal in the crystal, so that the effect of diffraction on the conversion efficiency will not be too large. This condition is the lower limit on the use of the near-field approximation.

If the electric field of the gaussian pump beams have the transverse dependence

$$E \propto \exp\left(-\frac{r^2}{w(z)^2}\right) \quad , \tag{2.57}$$

where the beam waist transforms according to

$$w(z) = w_0\sqrt{1+\left(\frac{z}{z_R}\right)^2} \tag{2.58}$$

the idler polarization will have a similar gaussian transverse profile with a local waist of

$$\frac{1}{w_i^2(z)} = \frac{1}{w_p^2(z)} + \frac{1}{w_s^2(z)}, \tag{2.59}$$

though this idler polarization will obviously not transform longitudinally as a Gaussian beam. This case is in constrast to harmonic generation, where the product of two identical gaussian beams produces a harmonic polarization that also propagates as a gaussian beam. In the confocal

approximation we ignore the z dependence of all beams and choose the pump focusing to make the waist of the idler polarization the same as that of a confocally focused beam of the idler wavelength in the crystal, so that

$$L = 2z_R = 2\frac{\pi w_{idler}^2}{\lambda_{idler}} \tag{2.60}$$

The pump and signal waists make symmetric contributions to the size of the idler beam, so we assume them here to be equal. The optimal efficiency is actually obtained with the pump and signal having equal confocal parameters rather than equal waist sizes. However, in the highly non-degenerate case, the two conditions are approximately the same. Using the expression for the Rayleigh length, we obtain an expression for the DFG power at zero phase mismatch in the confocal idler approximation

$$\frac{P_{DFG}}{P_2} = \eta_{DFG} P_1 L \tag{2.61}$$

where

$$\eta_{DFG}\left[\frac{1}{W \cdot cm}\right] = \frac{8\pi^2 d_{eff}^2}{n^2 c\varepsilon_0 \lambda_{DFG}^3} = \frac{9.4\times10^{-2}}{\lambda_1^3[\mu m]} \quad . \tag{2.62}$$

Again, the refractive index is assumed to be 3.2 and d_{eff} to be 57 pm/V. The DFG efficiency for generating 10 μm radiation is approximately 1×10^{-4} $(W*cm)^{-1}$. With 100 mW at each of the pump wavelengths and a 1 cm long bulk OPGaAs crystal, the output power would be 1 μW, which is a factor of 10^3 lower than that of the waveguide device having the same 1 cm length. However, the high losses measured in waveguide devices at present make bulk and waveguide devices more comparable, since useful waveguide lengths will be in the < mm regime. The bulk crystal avoids the waveguide's pump power limitations arising from the very small waveguide end-facet areas. With the much lower attenuation losses measured in bulk OPGaAs compared to waveguide devices, longer crystals can be used. 1 Watt of power at each pump wavelength and a 3-cm-long OPGaAs crystal could achieve 1 mW DFG power at 10 μm using crystals comparable to those already demonstrated.

Further investigation of the effects of focusing and diffraction on DFG efficiency [15, 16] have been performed by Guha, and Mayet. The gain in efficiency with tighter focusing begins to saturate around the confocal idler condition and exhibits a maximum in the vicinity of a confocal pump condition, but that maximum is relatively broad, with similar efficiencies obtained across a wide range of focusing conditions. More potentially complicating for many applications is the

impact of focusing on the beam quality. Mayet investigated the M^2 value of the DFG beam as a function of focusing and found that the confocal idler case resulted in M^2 values around 1, while $M^2 > 1$ for the confocal pump situation. When the pump is confocal, the M^2 value is a function of the non-degeneracy. At degeneracy the confocal pump case has an M^2 value of 1.03, while for the $\delta = 2/3$ case the M^2 at the same focusing condition is 1.32. Thus, depending on the application, one can trade-off between maximum efficiency around the pump confocal condition and higher beam quality available at the confocal idler condition. More detailed analysis of these focusing effects is outside the scope of this dissertation, but will be required for optimization of the devices.

2.3.2 Second harmonic generation

Second harmonic generation is useful for mid-IR generation though frequency doubling of CO_2 lasers. For our purposes it provides an easier tool for evaluating new materials, since only one input beam is required. The effects of focusing on second harmonic generation efficiency have been analyzed in detail by Boyd and Kleinman [17] and only the results will be presented here. For a beam of wavelength λ focused into a crystal of length L and refractive index n with a waist of $1/e^2$ radius w_0, one can define a normalized focusing parameter $\xi = \frac{L}{2z_R} = \frac{L\lambda}{2\pi w_0^2 n}$ which characterizes the focusing of the beam in a crystal. Boyd and Kleinman define a function $h(B, \xi)$ which includes the impact of focusing on the SHG efficiency. B is a normalized walkoff length, but since GaAs has an isotropic refractive index, $B = 0$ for all nonlinear optical interactions at normal incidence and there are no length limitations due to Poynting vector walkoff. For optimum phase mismatch, which is not necessarily $\Delta k = 0$ in the focused case, the maximum conversion efficiency for a particular focusing condition is

$$\frac{P_2}{P_1} = \frac{8\pi d_{eff}^2}{n_2 n_1^2 c\varepsilon_0 \lambda_1^2} P_1 k_1 L h(B, \xi) \ , \tag{2.63}$$

where k_1 is the k-vector for the fundamental beam in the crystal. The optimum efficiency is found at $L = 5.74 z_R$, where the h factor is 1.2. For harmonic generation of 5 μm radiation using a 10 μm fundamental beam in a 1 cm long GaAs crystal, one obtains a conversion efficiency of 2.1×10^{-4} $(W*cm)^{-1}$. The approximate factor of 2 difference between the efficiency for SHG with

a 10 μm fundamental and the efficiency for DFG generation of 10 μm arises from the different waists used to calculate the effective area in equation 2.11. For SHG the 10 μm pump waves are confocally focused in the crystal, while for DFG the pump waves in the near-IR have waists larger by $\sqrt{2}$ to generate a confocally focused idler wave.

2.4 Conclusion

In this chapter we developed expressions for the conversion efficiency of various low-power nonlinear optical devices, in both plane-wave and confocal approximations, focusing primarily on difference frequency generation. Additionally, we investigated the effects of top cladding layers on the modes of 4-layer slab waveguides, calculated the effective areas of waveguide devices as a function of the normalized waveguide parameters such as confinement and degeneracy, and estimated the conversion efficiencies achieveable in waveguide devices.

References

1. R.W. Boyd, *Nonlinear Optics* (Academic Press, San Diego, 1992).
2. Y.R. Shen, *The Principles of Nonlinear Optics* (John Wiley & Sons, New York, 1984).
3. D. Marcuse, *Theory of Dielectric Waveguides*, Quantum Electronics -- Principles and Applications, P.F. Luao and P.L. Kelley eds. (Academic Press, San Diego, 2nd ed., 1991).
4. A. Yariv, "Coupled-mode theory for guided-wave optics," IEEE J. Quantum Electron. **QE-9**, 919-933 (1973).
5. E.J. Lim, "Quasi-phasematching for guided-wave nonlinear optics in lithium niobate," Ph. D. dissertation (Stanford University, Stanford, CA, 1992).
6. M.S. Stern, "Semivectorial polarised finite difference method for optical waveguides with arbitrary index profiles," IEE Proc. J **135**, 56-63 (1988).
7. M.S. Stern, "Rayleigh quotient solution of semivectorial field problems for optical waveguides with arbitrary index profiles," IEE Proc. J **138**, 185-190 (1991).
8. B.M.A. Rahman and J.B. Davies, "Vector-H finite element solution of GaAs/GaAlAs rib waveguides," IEE Proc. J **132**, 336-342 (1985).
9. G.B. Hocker and W.K. Burns, "Mode dispersion in diffused channel waveguides by the effective index method," Appl. Opt. **16**, 113-118 (1977).
10. J. Buus, "The effective index method and its application to semiconductor lasers," IEEE J. Quantum Electron. **QE-18**, 1083-1089 (1982).
11. H. Kogelnik, "Theory of dielectric waveguides," in *Integrated Optics*, T. Tamir ed. (Springer-Verlag, New York, 1975) pp. 13-81.
12. H. Kogelnik and R.V. Ramaswamy, "Scaling rules for thin-film optical waveguides," Appl. Opt. **13**, 1857-1862 (1974).
13. E.J. Lim, S. Matsumoto, and M.M. Fejer, "Noncritical phase matching for guided-wave frequency conversion," Appl. Phys. Lett. **57**, 2294-2296 (1990).
14. E.A.J. Marcatili, "Dielectric rectangular waveguide and directional coupler for integrated optics," Bell Syst. Tech. J. **48**, 2071-2102 (1969).
15. S. Guha, F.J. Wu, and J. Falk, "The effects of focusing on parametric oscillation," IEEE J. Quantum Electron. **QE-18**, 907-912 (1982).
16. J. Mayet, "Quasi-phase-matched frequency conversion of gaussian beams," report (Ginzton Laboratory, Stanford University, Stanford, CA, 1996).
17. G.D. Boyd and D.A. Kleinman, "Parametric interaction of focused gaussian light beams," J. Appl. Phys. **39**, 3597-3639 (1968).

CHAPTER 3: All-Epitaxial Fabrication of GaAs Orientation Templates

Invention of an all-epitaxial orientation template fabrication process is the breakthrough which made possible the growth of orientation-patterned films and therefore the optical device results presented in subsequent chapters. This chapter surveys the background research relevant to all-epitaxial template fabrication and describes in detail our investigations into template fabrication processes. We have successfully developed templates suitable for regrowth of orientation-patterned bulk and waveguide devices. We have also explored improvements on this process which could lead ultimately to higher performance nonlinear optical devices, particularly for waveguide applications. Undoubtedly, this process can be refined much further than we have succeeded in doing to date and we hope that the combination of background, results, and suggestions presented here will be useful for anyone pursuing similar investigations.

This chapter begins with an overview of the primary issues in template fabrication, after which it reviews epitaxial growth of both Ge and GaAs on each other and also their integration to form a GaAs/Ge/GaAs heterostructure. It then presents the results of our experiments in epitaxial inversion, discusses them in the context of related research, and lays out profitable routes for future exploration. The last sections address issues associated with template patterning, etch stop behavior, and regrowth considerations.

3.1 Introduction

Epitaxial growth of orientation-patterned semiconductor films useful for quasi-phase-matched nonlinear optics requires templates whose surface contains a modulation in crystalline orientation with the proper period and duty cycle. There is little precedent for fabrication of such controllably multi-orientation crystals and almost none for achieving it solely epitaxially. The most successful patterned growth technique to date utilized wafer bonding to provide an inverted layer and produced waveguide devices whose performance was limited by waveguide losses attributed to longitudinal corrugation of the core-cladding boundaries [1]. The only previous all-epitaxial attempt to solve this problem was made in II-VI materials [2]. Waveguides were fabricated using this technique, but issues of corrugation associated with unequal epitaxial growth rates for (001) and (111) surfaces resulted in very high waveguide losses.

3.1.1 Overview

Since crystal quality considerations limit us to epitaxial growth techniques in materials like GaAs, there are two possible strategies for achieving an all-epitaxial surface with two different orientations present. Both utilize photolithography to set the domain periods and duty cycles, making straightforward the fabrication of very short periods, the preservation of domain coherence across the wafer, and the fabrication of different-period devices on the surface of a single wafer. The first strategy starts with a wafer of a primary orientation and involves spatially selective growth of secondary orientation material. This can be done using a self-patterning technique such as ion-beam deposition or some kind of selective area epitaxy through a photolithographically defined mask. The second possibility reverses the steps – the secondary crystal orientation is grown uniformly in a thin layer across the primary orientation wafer surface. After deposition of a photolithographically defined etch mask, one etches down through the thin film to expose the primary orientation resulting in the desired orientation template. Figure 3.1 illustrates both possibilities. We have explored both of these approaches for template fabrication, but have focused primarily on the etch-back approach for reasons of film quality which will become clearer as we proceed.

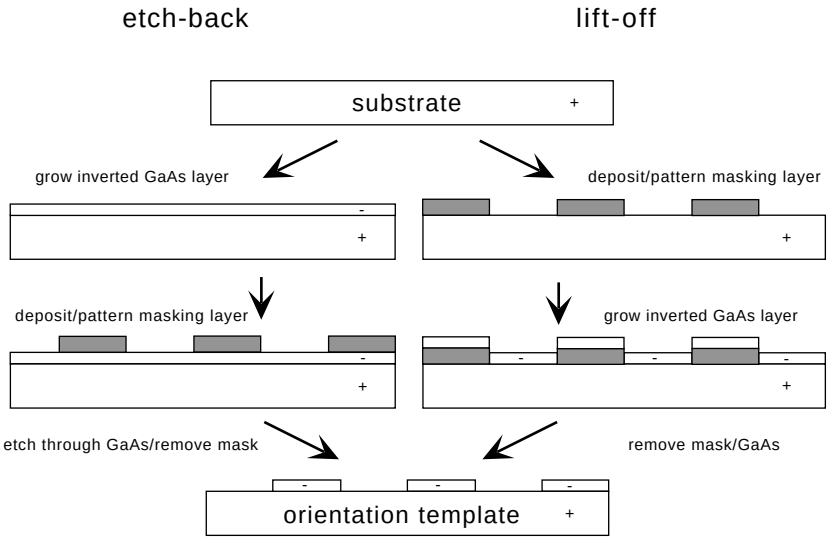

Figure 3.1: Two strategies for obtaining an all-epitaxial, orientation-patterned film.

Both of the above strategies will produce a corrugation in the template which may be preserved during subsequent regrowth. If this residual corrugation reaches the subsequently-grown waveguiding layers, it will result in core-cladding interface corrugation and associated scattering

losses in the waveguides. Therefore, we desire to minimize the template corrugation so as to reduce the ultimate waveguide losses. Since the original template corrugation results primarily from the total layer thickness required to achieve the epitaxial inversion, minimizing template layer thicknesses is a high priority. It may be possible to planarize the film surface during subsequent regrowth, but reduction of the initial template corrugation will obviously make things easier. One could also consider variations on the above strategies, such a slight back-etch through the mask before growing the inverted layer in the lift-off approach so that a nominally flat template surface results.

Regardless of how the orientation pattern is defined, some technique is required for modulating the crystal growth in a fashion such that the nonlinear optical susceptibility seen by the optical radiation varies from section to section. In the absence of a spontaneous ferroelectric polarization, this can only be achieved through a change in crystal orientation. As discussed in chapter 2, the highest effective nonlinear susceptibility and the greatest efficiencies are achieved when this modulation alternates sign, so that the two orientations differ by a crystallographic inversion. The zincblende crystal structure consists of a face-centered crystal (fcc) lattice structure with a two atom basis. Crystallographic inversion in a III-V zincblende semiconductor can be understood simply as an exchange of the two basis atoms (Ga and As, for example) on their respective sublattices, or equivalently as a reversal in direction of the single III-V bond which runs along the <111> direction. Figure 3.2 illustrates the two phases.

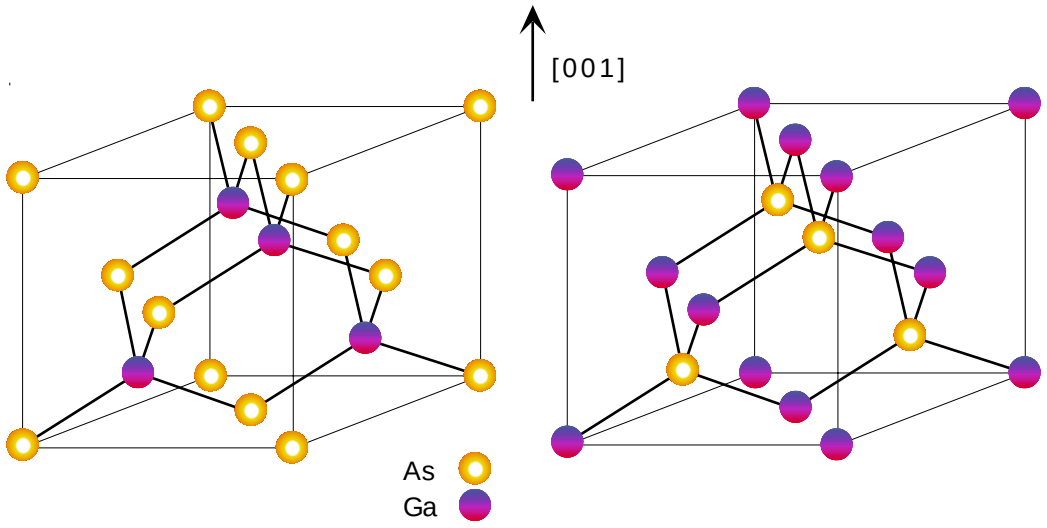

Figure 3.2: GaAs unit cells showing both GaAs phases.

The relationship between the two energetically equivalent phases, which differ by the desired crystal inversion, is designated "antiphase". Antiphase boundaries (APBs) separate regions of opposite phase and can lie in several different atomic planes [3]. The APBs form planes of incorrectly-bonded nearest neighbor atoms, As-As or Ga-Ga, with the exact configuration depending on the plane in which the APD lies. Since zincblende crystals have symmetry group $\bar{4}3m$, these phases differ by a 90° rotation about <001>, which is normal to the usual wafer surface of (001). This inversion can be visualized by rotating one of the unit cells in Fig. 3.2 by 90° about [001] and then lowering it by 1/4 of a unit cell to obtain the opposite phase. For (001) wafers this symmetry relationship is highly desirable for subsequent regrowth of orientation-patterned films because both phases have the same surface exposed, minimizing any asymmetry between the growth rates and resulting corrugations. This eliminates the major corrugation-producing complication in the work of Angell, *et al.* [2].

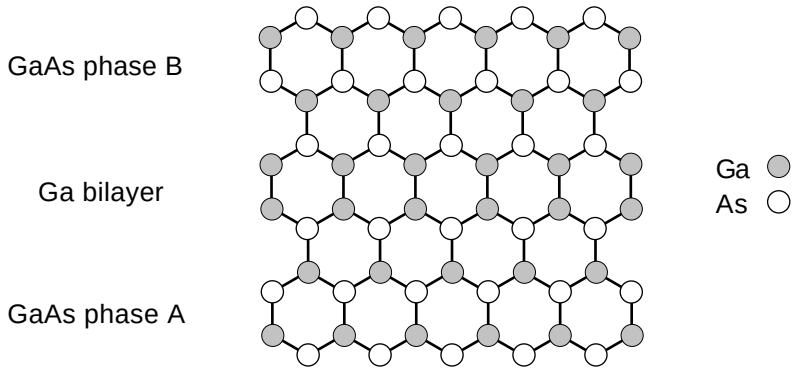

Figure 3.3: Gedanken epitaxial inversion with two consecutive atomic layers

Obtaining an epitaxial inversion thus requires that all the column III and column V atoms exchange sublattices at some point during crystal growth. If we imagine epitaxy as a simplistic spraying of alternating layers of Ga and As, then one would need only to deposit two consecutive layers (Ga, for example) of the same atomic species and then continue with the alternating sequence to achieve crystal inversion, as shown in Figure 3.3. However, such a cation bilayer would be extremely unstable and atomic exchange mechansims during subsequent deposition would result in continued growth of material in phase with the substrate. In fact, relative stability against such spontaneous antiphase twinning is clearly a necessary precondition for normal high-quality epitaxial growth.

Thinking more generally, any scheme which relies on an exact number of atomic monolayers separating the two GaAs phases is difficult to implement both for technological and fundamental reasons. Accurate calibration of growth rates to sub-monolayer precision is difficult to accomplish. More importantly, rather than being a simple plane of atoms, the actual vacuum-semiconductor interface exhibits a complicated free-energy-driven reconstruction with partially complete atomic layers extending several monolayers into the crystal [4]. Not only does this fact make the utility of depositing an exact number of monolayers unclear, but it also hints that the ultimate orientation of the top GaAs will depend critically on the exact surface reconstruction.

A more realistic approach to epitaxial inversion uses a neutral buffer to isolate the two orientations and governs nucleation of the secondary orientation by the buffer surface characteristics rather than the thickness. A suitable buffer must meet several criteria. It must preserve crystal quality so that subsequent layers are not highly defective. Precise buffer layer thickness should not matter. There must be some method for nucleating the desired orientation on top of the buffer. Finally, it is desirable that the buffer and secondary orientation layers of the template structure be as thin as possible to minimize template corrugations which might propagate into device layers.

To find a neutral buffer layer, it is logical to look at those column IV semiconductors which have been widely investigated for use in epitaxially-fabricated devices. These have the diamond crystal structure, which is identical to the zincblende III-Vs except that both the atoms in the basis are the same. Comparing the lattice constants of GaAs (5.6533 Å) with Si (5.4309 Å) and Ge (5.6461 Å), we see that Si has a 4% lattice mismatch, while Ge has < 0.1 % mismatch. This makes thick (> 1000Å) Ge layers possible without generation of misfit dislocations, whereas lattice relaxation of Si layers grown on GaAs begins between 10 Å and 15 Å [5, 6]. These strain effects on epitaxial inversion quality were confirmed by Koh, *et al.* who observed by cross-sectional transmission electron microscopy that inverted films with Si buffer layers had much higher densities of misfit dislocations than did those with Ge buffer layers [7, 8].

A more complicated problem is finding a technique for controlling the orientation of the GaAs layer on top of Ge, since in general both GaAs domains (differing by a crystal inversion) can nucleate and grow equally well on the higher symmetry Ge surface. GaAs growth on a neutral Ge (100) surface produces a poly-domain GaAs film with a high density of antiphase domains (APDs). Such highly defective films are not suitable for electrical or optical applications and a great deal of research was devoted to polar-on-nonpolar epitaxy in the late 1980s and early 1990s with the goal of hybrid integration of III-V and IV materials, particularly GaAs on Si substrates.

The keys to obtaining single-phase polar films on nonpolar substrates were found to be a combination of growth conditions and use of misoriented substrates polished a few degrees from the nominal crystal plane, which creates an array of atomic steps and terraces running in one direction across the nonpolar surface [9]. This misorientation breaks the symmetry between the two domains, favoring one over the other during nucleation and subsequent crystal growth. Single domain films could be obtained though a combination of preferential nucleation and APD annihilation during subsequent growth. This dependence of polar domain on the misorientation of a nonpolar surface gives us the necessary mechanism for GaAs orientation control. By choosing the proper growth conditions and misorientation direction of the original GaAs wafer surface, we will force the top GaAs layers in a GaAs/Ge/GaAs heterostructure to be inverted with respect to the substrate.

We have worked solely with GaAs/Ge/GaAs heterostructures to achieve GaAs crystal inversion. Similar GaAs/Ge/GaAs epitaxial inversion has been recently achieved by Koh, *et al.* [8] working independently from us. Such epitaxial inversion has also been achieved using Si interlayers [7] by the same researchers, but this process resulted in films with large antiphase domains and some density of misfit dislocations. Additionally, they found antiphase rotation and GaAs quality to be sensitive to the exact Si layer thickness, with layers below 10 Å not exhibiting domain inversion, but layers >15 Å beginning to exhibit relaxation of the Si. The Ge technique is not sensitive to layer thickness in the same manner and seems clearly more promising due to the excellent lattice match. Only the Ge template technique has been carried all the way to nonlinear optical devices, as will be described in chapters 4 and 5.

3.1.2 MBE outline

For fabrication of the templates and waveguide devices we utilize the technique of molecular beam epitaxy, primarily because we have access to the proper equipment and expertise. Molecular Beam Epitaxy (MBE) was developed in the late 1970's and has played a fundamental role in the development of heterostructure electronics and optics. Extensive references are available [10, 11], so only a brief sketch will be presented here. In MBE, the single crystal substrate is placed into a high vacuum environment (typically with base pressure of $< 10^{-10}$ torr) which contains a number of high-temperature evaporation cells. When these cells are heated to sufficient temperatures, evaporation from the liquid or solid source material produces a molecular beam which, because of the large mean free path in the high vacuum environment, can propagate across the chamber and impinge on the wafer. The adsorbing atoms migrate across the surface and even-

tually incorporate in registry with the substrate. Moveable shutters placed in front of each cell allow on-off modulation of the individual beams and thereby control the composition of the composite beam striking the wafer. In this way heterostructures of varying composition can be grown for electronic and optical devices. The UHV environment of MBE allows the use of surface analysis tools such as reflection high energy electron diffraction (RHEED) and X-ray photoemission spectroscopy (XPS) to probe the surface properties and the growth mechanisms themselves. Also, the simplicity of the incident atomic species provides a model system for studying various crystal growth issues. In our discussion below we confine ourselves to issues of MBE growth of GaAs/Ge/GaAs heterostructures for orientation templates. Similar results may well be achievable via alternative epitaxial growth techniques such as metal-organic chemical vapor deposition (MOCVD), but that remains to be investigated.

3.1.3 RHEED

Since extensive literature on RHEED is available [12], this section will provide only a brief outline to orient the unfamiliar reader. RHEED involves diffraction of a ~ 17 kV electron beam at shallow angle (~ few °) off the wafer surface and onto a phosphor screen to observe the surface atomic structure. Atoms at a vacuum-semiconductor interface will reconstruct to minimize the energy of the dangling bonds. The equilibrium reconstruction is a function of temperature, overpressure, surface atomic species, etc. Such reconstruction will typically produce periodicities in the surface atomic structure having periods that are integer multiples of the unit cell repeat distances along the particular direction in question. For example, if every other atom is displaced on a reconstructed surface, the reconstruction would be denoted as "two-fold", since it would exhibit a period twice that of a fully populated, unreconstructed surface. When these various periodicities are present in the wafer atomic reconstruction, the diffracted electron beam includes additional spots or streaks when the electron beam is directed orthogonal to the repeat direction. RHEED observation of GaAs and Ge surfaces is most often performed with the electron beam directed along the [110] and $[1\bar{1}0]$ directions. Observed RHEED patterns are then designated as N x M, where N and M are the repeat lengths in these two orthogonal directions (for example, 2 x 4, or two-fold by four-fold). This abstract connection between RHEED pattern and surface reconstruction should be sufficient to understand the discussion later in this chapter. More detailed information about the GaAs surface reconstructions generating the RHEED patterns and interpretation of electron diffraction patterns from GaAs surfaces can found in [4].

3.2 Epitaxial inversion: Background

Fortunately for the course of this project, we were able to draw significantly on previous research into GaAs and Ge growth in developing a practical GaAs/Ge/GaAs template fabrication process. This section reviews previous research which both illuminated and constrained our template fabrication development. Comparison between our results and others' along with more detailed examination of complex epitaxial issues affecting further template development will be given after presentation of our experimental results.

Growth of Ge on GaAs and GaAs on Ge have been investigated in detail, but GaAs/Ge/GaAs heterostrucures have undergone very little examination as interdiffusion at the GaAs and Ge boundaries makes these heterostructures unsuitable for electronic or quantum well devices. Many important questions about growth issues remain unanswered, since growth of the heterostructures is more complicated than simple sequencing of the Ge/GaAs and GaAs/Ge growth processes. The optimal growth temperatures for GaAs/Ge and simple GaAs lie in a range where Ge films can exhibit morphological instability. It is also not clear whether the same surface reconstructions and step structure can be obtained on a Ge/GaAs film as are obtained on a bulk Ge crystal. This is extremely important, because the problem of antiphase domain disorder has been solved for growth of GaAs/Ge by tailoring of the surface step structure. Finally, the presence of As is a further potential complication whenever Ge is grown on GaAs, as As has been observed to modify the Ge surface step structure. These issues and the research elucidating them will be examined in the following sections.

3.2.1 Growth of Ge on GaAs(001)

Growth of Ge on GaAs (001) is relatively straightforward. Since a nonpolar material is deposited on a polar one, there are no issues of antiphase disorder. The Ge growth temperature is an important parameter for the growth of such thin films, however, and excessive temperatures can lead to clustering effects. At low temperatures, Ge/GaAs(001) grows in a quasi-Frank-van der Merwe (FM) or layer by layer mode, while at higher temperatures it grows in a Stranski-Krastanov (SK) or layer-by-layer followed by island growth mode. The Ge surface atomic diffusion length is sufficiently short at low temperature to produce uniform layers, but the increased diffusion length at higher temperatures allows the film to relax into the lower energy island configuration. In the experiments of Wang, *et al.* thin Ge films up to 20 Å in thickness grown around 400 °C were annealed at higher temperatures and clustering behavior of the Ge film was observed for temperatures above 525 °C [13, 14]. At 600 °C, complete clustering of an originally uniform 20-Å-thick

Ge film grown on GaAs at lower temperature (400 °C) required about 15 minutes, in the process exposing hypothesized Ge-Ga dimers on the surface outside of the clusters. In this way a thin Ge film behaves very differently than a bulk Ge surface or a thicker Ge film. Pukite and Cohen, on the other hand, report no signs of macrosopic clustering when annealing a 1000-Å-thick Ge film grown on GaAs at similar temperatures [15]. Presumably there is a critical thickness over which clustering no longer results in a net reduction of free energy and the Ge surface remains stable at elevated temperature. Naturally, the thinnest possible Ge layers are desirable for minimizing template corrugations, so the stability of the Ge films at higher temperatures, a potentially important factor for GaAs growth on Ge, might well come at the cost of ultimate waveguide device performance.

Another potentially complicating issue in Ge/GaAs(100) growth is outdiffusion and/or surface segregation of As during or after Ge deposition, since antiphase domain characteristcs of GaAs growing on Ge(100) depend strongly on the surface structure and exposure to As has been demonstrated to alter the Ge surface. For low Ge deposition rates of < 1 Å/min at 320 °C, Bauer and Mikkelsen observe that a Ge film grown on GaAs exhibits an As-stabilized surface, with the amount of surface arsenic independent of the concentration of arsenic present on the GaAs surface prior to Ge growth [16]. This surface As layer results from segregation of As through the Ge film and is reported to persist up through layers ". . .orders of magnitude greater than the three monolayer film . . ." examined in that particular reference. The authors conclude that a highly stable $GeAs_x$ surface layer forms, lowering the free energy of the the Ge(001) surface and making it stable to subsequent thermal annealing in both vacuum and As vapor, though temperature ranges of this stability are not reported. Similar results were obtained by Mrstik, whose auger electron spectroscopy (AES) data on Ge layers up to 10 monolayers in thickness were best fit by assuming 1/2 monolayer of As at or near the surface of the Ge film [17]. Segregation of a fractional monolayer of As on Ge films up to 2000 Å in thickness was also observed by Katnani, *et al.* [18]. They all find that the As-terminated Ge surface after growth exhibits a surface reconstruction which is a superposition of 2 x 1 and 1 x 2. Unfortunately, this is the same reconstruction present on a clean Ge surface which has single atomic steps, so electron diffraction alone is not able to determine whether the surface is terminated with As. Stucki, *et al.* [19] have studied the GeAs crystal surface as model for the As-terminated Ge surface and find no observable surface states and low surface reactivity, agreeing with the hypothesis of Bauer and Mikkelson. Higher Ge deposition rates are reported to produce clean Ge surfaces at 340 °C on GaAs (110), but the As-enriched surface layers return upon annealing at only 440 °C, presumably due to As diffusion through the Ge film driven

by the large free energy gain upon conversion to the more stable $GeAs_x$ surface [16]. In contrast, Neave, *et al.* [20] have reported x-ray photoemission (XPS) measurements showing clean Ge surfaces even at higher temperatures using higher Ge growth rates. The background As pressures in the experimental chambers are typically not reported in the papers, but presumably in the course of such detailed surface analysis the authors would have verified that the experiments were not being affected significantly by unintended As adsorption.

The presence of As on the Ge surface, intentional or otherwise, is important because of its effects on surface structure. Pukite and Cohen observed that absorption of even fractional monolayer amounts of As catalyzed a dramatic transition in the surface step structure on a 1000-Å Ge film grown on GaAs, with additional four-fold periodicities appearing in the RHEED pattern along [110] direction [15]. The As could be desorbed at higher temperature and the transition in the step structure was reversible with As desorption as observed by RHEED. Unfortunately, the temperature range of this desorption lies in the regime where thinner Ge films would be expected to exhibit clustering effects. In the absence of any clear way to prevent As exposure or remove it subsequently, the probable presence of unintentional As on the Ge surface constrains the epitaxial inversion process. As most previous research into growth of GaAs on Ge used bulk Ge wafers which are presumably free of As contamination, this will limit the direct application of those results to our GaAs/Ge/GaAs heterostructure inversion problem.

3.2.2 Growth of GaAs on Ge(001)

Epitaxial growth of polar on nonpolar materials such as GaAs on Ge or GaAs on Si is a much more complicated problem than that of nonpolar on polar growth, primarily due to the issue of antiphase disorder. In general, both GaAs domains will nucleate and grow on a Ge (001) or Si (001) surface because of the higher surface symmetry of the diamond structure surface. When no steps are taken to control this process, random domain nucleation results in an approximately 50/50 distribution of the two domains and a high density of antiphase boundaries. As thicker GaAs films are grown, the domain boundaries can annihilate with one another and consolidate so that the average domain size increases while the film remains poly-domain [21]. Since these APBs are expected to introduce deep levels into the energy gap, such films will have poor electrical properties and produce poor electronic devices.

The Ge (001) surface, whether intentionally misoriented or not, will have some density of atomic steps separated by terraces. As the misorientation angle increases, the step density will

increase proportionally and the average terrace length will decrease. The step character of a clean, bulk Ge surface changes with thermal history, with single steps predominating in the temperature range of 350 °C to 500 °C and double atomic steps dominating after high temperature annealing above 600°. The terraces in between the steps exhibit a reconstruction of the surface dangling bonds to form rows of dimer chains running in either the [110] or $[1\bar{1}0]$ directions. When two terraces are separated by a single atomic step, their dimer chains run in orthogonal directions, while terraces separated by a double atomic step have dimer chains running in parallel directions. The surface atomic reconstructions of the two terraces are chemically identical, differing only by a 90° rotation about the [001] surface normal. RHEED examination of a Ge single-stepped surface yields an apparent 2 x 2 reconstruction, which is in actuality a superposition of the 1 x 2 and 2 x 1 domains present on the two terraces. The double stepped surface after annealing exhibits a single 1 x 2 domain, since one kind of terrace predominates.

Antiphase disorder is dependent on both the uniformity of the initial layers and the Ge surface step structure. Figure 4a illustrates GaAs growth on a Ge surface with an incomplete or non-uniform prelayer. For example, As present on the surface after Ge growth would cause non-uniform nucleation if GaAs growth were inititated with what was intended to be a uniform Ga prelayer. Note that these prelayer contamination effects are in addition to any other effects the unintentional As would have on the Ge surface step structure. This is important, because another generator of antiphase disorder is single atomic steps present on the Ge surface, as illustrated in Figure 4b. Even when a completely uniform prelayer is applied (As, in this case), different GaAs domains will nucleate on the two terraces if the prelayer atoms bond similarly on the chemically identical but rotated terraces separated by a single atomic step. APBs will then be generated at each single step, and a highly defective initial GaAs film will result. The relative 90° rotation of the reconstructions on the two different Ge terrace surfaces leads naturally to antiphase GaAs, since a 90° rotation about [001] corresponds to a crystal inversion in GaAs. The GaAs phase remains the same across a double step, making a double-stepped Ge surface much more conducive to good quality GaAs growth. APBs are shown in Fig. 3.4 propagating along two different possible planes, {110} and {111}, though there is no expected connection between the APB propagation plane and the origin of the APBs.

Significant improvements in polar-on-nonpolar fabrication occurred in the mid-1980s when Akiyama, *et al.* [22] and Fisher, *et al.* [23] demonstrated that growth on a misoriented surface with the proper nucleation conditions and complete initial prelayers could lead to antiphase-

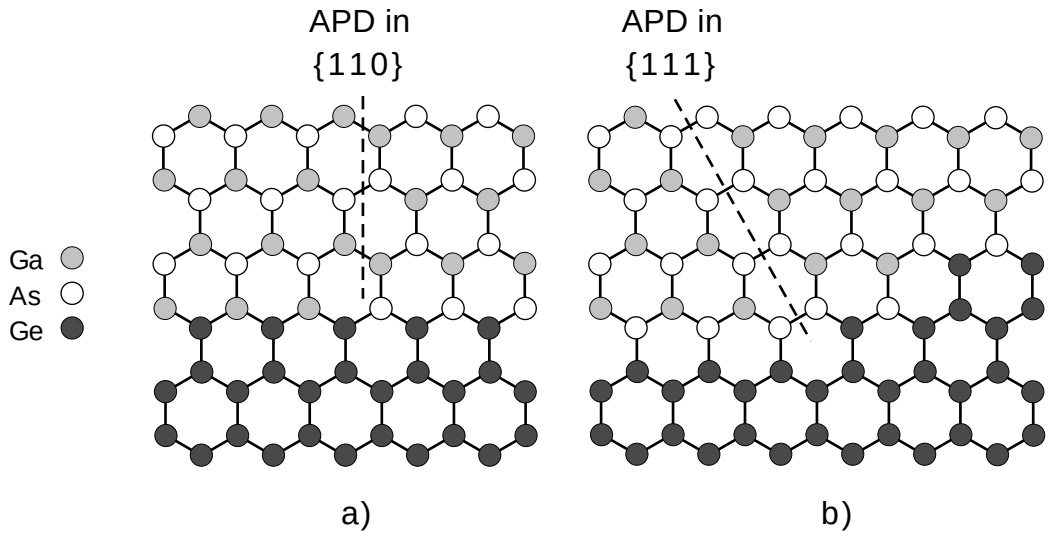

Figure 3.4: Schematic illustrating two hypothesized origins of antiphase domains. Figure 3.4a shows effect on GaAs nucleation of a mixed prelayer on a flat Ge surface, while 3.4b shows effects of single vs double atomic steps on the Ge surface with a uniform prelayer. Two different possible APB planes are illustrated.

domain-free GaAs. One of the important discoveries was that high-temperature annealing of a misoriented Si or Ge surface could dramatically reduce or eliminate the single steps, leaving a double-stepped surface and converting the normally two-domain nonpolar surface into a single domain reconstruction. The uniform-domain surface minimized antiphase domain nucleation and made possible antiphase-domain-free layers of polar materials grown on nonpolar substrates.

APD-free growth was also demonstrated on misoriented Ge surfaces which contained a majority of single steps [15]. In this case the authors proposed that the domain nucleation began at the step edges, then propagated out across the terrace steps. They found that the growth was single-domain from the very beginning of nucleation as observed by RHEED. The explanation proposed was that the atomic bonding configuration at the atomic steps itself favored a particular atom, either Ga or As. Such preferential atomic incorporation at the step edge created an energetically favorable configuration for the same type of atom at the next site and some atomic exchange mechanism swapped such an atom into that site. This process could then continue sequentially across the entire terrace until it was converted into a single domain. By this explanation, the configuration at the atomic steps and the misorientation direction determines which domain of GaAs will predominate. The misorientation angle determines the width of the terraces that the exchange mechanism must uniformize to achieve single domain GaAs. One expects that such a transition would be kinetically limited, with wider terraces requiring more time for the exchange mechanism

to propagate across the surface before the atoms are locked in place by deposition of subsequent layers. Kroemer gives a good review of these and other issues in single-domain nucleation in polar-on-nonpolar epitaxy [9].

Even without APD-free nucleation, however, single phase GaAs films can still be obtained through APD annihilation. This route requires predominant nucleation of one domain due to mis-orientation-related effects followed by eventual annihilation during growth of residual APDs. Obviously, the APD-free nucleation is preferable, but APD annihilation offers a backup solution if such nucleation proves difficult. Ting, *et al.* proposes that two different annihilation mechanisms occur during film growth when antiphase domains are present [24]. The first is self-annihilation, in which a single APD shrinks with continued crystal growth and eventually disappears by propagation of the APBs on the proper crystal planes. This phenenomenon has been explored in detail by Li in the case of MOCVD-grown GaAs films on Ge, and he clearly shows that single APDs annihilate by propagation of APBs on the {110} planes tilted 45° from the (001) surface normal under As-rich MOCVD growth conditions [25, 26]. In this case the APD annihilation height will be roughly comparable to its initial lateral size. This mechanism is most likely when domains are isolated and their density is low. The second annihilation mechanism is a coalescence, in which the APBs of nearby APDs annihilate with one another to form larger overall APDs, something which is more likely when a high density of antiphase domains is present at nucleation. This coalescence mechanism can produce very large antiphase domains, which then require significant film heights to self-annihilate during subsequent crystal growth.

The most detailed investigations of APD-free growth of GaAs on bulk Ge by MBE were performed by a collaboration [24, 27] which included extensive cross-sectional and plan-view TEM analysis of films grown under a variety of conditions. These results will be described in some detail since we adapted their process at points in our exploratory epitaxial inversion experiments. Their optimized process for GaAs growth on Ge consists of deposition of a 1000 Å Ge buffer layer on the Ge substrate to bury contamination and produce a clean Ge surface, followed by annealing of the Ge surface at 650 °C for 20 minutes to produce a primarily double-stepped, single-domain surface. GaAs growth was initiated by either Ga or As prelayers at 350°C with system background pressures < 10^{-9} torr to prevent partial prelayers. The first 10 GaAs monolayers were grown by migration enhanced epitaxy (MEE) at 350 °C to limit Ge diffusion into the GaAs. This was followed by co-deposition at 500 °C to prevent the excess As incorporated at low MBE growth temperatures (350 °C) from precipitating and generating dislocations when the wafers are

heated to the ultimate GaAs growth temperature. This procedure yielded consistently APD-free films, even on surfaces containing a few residual single steps. As-prelayers were preferred, since they self-limit due to desorption, unlike Ga prelayers which must be carefully calibrated. The authors conclude in accord with previous research that the most important issues for minimizing APDs are the pre-anneal to produce a double-stepped surface and the necessity of depositing a uniform prelayer. Their realization of APD-free GaAs in the presence of residual single steps, as well as their observation that the final GaAs orientation is independent of prelayer (Ga vs As), offer strong evidence for some atomic exchange mechanism operating even at the 350 °C nucleation temperature.

Unfortunately, the excellent results obtained by Sieg, *et al.* for GaAs on Ge can only be applied to our problem in a limited way. The essential step is an anneal at 650 °C for 20 min to produce a surface with only double atomic steps. While this works well for a Ge epilayer on a Ge wafer, additional complications arise for Ge films on GaAs. For thin (20 Å) Ge films, clustering effects are expected to be severe in this temperature range. Even if the films are sufficiently thick to be stable under high temperature annealing, it is not clear that the desired double-stepped surface will result. In their paper containing highly detailed observations of surface step structure by RHEED, Pukite and Cohen [15] mention nothing about double stepping behavior on their 1000 Å thick Ge films grown on GaAs, despite working in the same temperature range (> 600 °C) where such annealing is successful on bulk Ge surfaces. Such double-stepping should have been easily observable by RHEED had it occurred. Instead, they observe that the single stepped surface persists up to temperatures of 680 °C provided that the surface is not exposed to an excessive As flux. The reasons for the different observed behavior on bulk Ge and thick Ge films on GaAs in the same temperature range are not clear, but possible candidates include strain or surface As coverages below the detectability limit of Auger spectroscopy. In any case, these results do not offer any clear method for achieving a double-stepped surface on a Ge film grown on GaAs.

3.2.3 Growth of GaAs/Ge/GaAs heterostructures

As is becoming clear, the growth of GaAs/Ge/GaAs heterostructures is significantly more complicated than a simple combination of optimal growth procedures for Ge on GaAs and GaAs on Ge. One of the few investigations of GaAs/Ge/GaAs heterostructures was by Strite, *et al.* [28-30]. They grew 20-Å-thick Ge layers on wafers of both nominal (001) orientation and also (001) misoriented towards [110]. After Ge deposition they ramped the temperature to 500 °C, applied either an As or Ge prelayer followed by 500 Å of GaAs, then ramped to 550 °C for further GaAs

growth. Single-phase GaAs was eventually obtained using various wafer/prelayer combinations with the best quality results obtained with misoriented wafers and the As prelayers, which is not surprising given the considerations of the previous section. For nominally (001) wafers, the orientation of the GaAs depended on the prelayer, with different phases seen for Ga and As. This achievement of single-phase GaAs using nominally (001) wafers is at odds with the majority of similar experiments, so one suspects that some other factor, like accidental slight wafer misorientation, may play a role. When wafers misoriented 4° towards [110] were employed, the GaAs growth on Ge was observed to be single-domain from the initiation of growth by RHEED and the GaAs domain obtained was independent of prelayer. The 2 x 4 pattern indicated some roughening at the outset, but by 100 Å GaAs thickness the RHEED pattern exhibited the streaky character of a smooth surface. This behavior is observed despite clear RHEED observation of a mixed domain 1 x 2 + 2 x 1 Ge surface before GaAs growth containing both surface domains and presumably a high density of single-layer steps. The authors explain their results by an exchange mechanism driven by preferential bonding at the step edges. Finally, the domain observed was the same for both Ga and As prelayers on the 4° misoriented substrates. They used wafers misoriented towards the in-plane [110] and found that the top GaAs had the same phase as the substrate in both prelayer cases. XPS measurements indicated that no As was present on the Ge surface before GaAs growth initiation, though their growth conditions are similar to those of Bauer and Mikkelson [16], who observed segregation of As to the Ge surface.

3.3 Epitaxial inversion: Experimental

Our goals in investigating epitaxial inversion were twofold, corresponding to short and long-term research requirements. The first goal was to demonstrate all-epitaxial inversion and incorporate it into a template of sufficient quality for demonstrating optical frequency conversion devices. This goal we achieved successfully, as the subsequent chapters of this dissertation testify. The second goal was optimization of the template structure for best ultimate device performance, which requires minimization of APD size and density so that template layers can be as thin as possible. We have done some exploration into template optimization; while the results are not complete, our observations point in useful directions. Many of the results discussed here have been reported previously in the dissertation of Ebert [31], but will be reviewed here in order to provide a comprehensive analysis.

From the nonlinear optical device standpoint, we require only that the top film be APD-free by the point the optically important layers are grown. In theory, we could utilize coalescence and self-annihilation following imperfect nucleation to eliminate APDs by that point, since several microns of smoothing layers and cladding will be required before growth of the waveguide core, and even greater thicknesses will separate the APDs from the radiation for bulk devices. In practice, however, we determined that the presence of APDs had deleterious effects on chemical etching processes used to pattern the template, producing pinholes and roughened stripe edges on the templates. Because the inverted GaAs layer on top of the Ge must be thick enough to eliminate all APDs before removal for chemical etching, the APD height ultimately determines the initial template corrugation. Since minimization of this corrugation is essential for producing low-loss waveguides, we have strong motivation for minimizing the APD disorder.

3.3.1 Epitaxial inversion strategy

The results of Strite, *et al.* growing GaAs/Ge/GaAs heterostructures provided the point of departure for our template development. They observed that the top GaAs grew in-phase with respect to the substrate for nucleation at 500 °C on Ge films grown on (001) GaAs wafers misoriented 4° towards the in-plane $[110]$. Since the top-GaAs-layer orientation nominally depends only on the Ge surface structure and the direction of its atomic terrace steps, we can control the relative orientation of the top GaAs and substrate by controlling the misorientation of the Ge surface relative to the orientation of the GaAs substrate underneath. Achieving an antiphase GaAs film-substrate relationship under the same nucleation conditions requires the substrate to be inverted or 90° rotated about the surface normal compared to the work of Strite, *et al.* or misoriented towards the in-plane $[1\bar{1}0]$. We chose a 4° misorientation towards $[1\bar{1}0]$ to provide a similar step density and terrace size. These growth conditions are also consistent in nucleation temperature with the similar process of Pukite and Cohen, though again on substrates with different misorientation directions. We utilized Ge layer thicknesses between 30 Å and 100 Å. No significant differences between 30 Å and 100 Å Ge films were observed, but the effects of this parameter were not examined systematically.

All MBE growth was performed in twin Varian Gen II MBE systems with valved As crackers. All other sources are effusion cells. The two systems are connected by a UHV transfer system which allows wafer transfer between systems with background pressures $< 10^{-9}$. Originally all template growth (both GaAs and Ge layers) were grown in one system (#2), while GaAs

regrowth was performed in the other (#1). Later all GaAs growth occurred in system #1 and the wafers were transferred into system #2 only for growth of Ge layers. No differences were discernable between the two procedures. Growth temperatures reported are those of the thermocouple mounted on the sample holder directly behind the wafer. All template substrates were highly doped n-type ($1\text{-}4*10^{18}$). Typical GaAs/AlGaAs growth rates of ~ 1 μm/hour and typical As:Ga beam equivalent pressure ratios of ~15:1 were used unless noted otherwise. All Ge growth was performed at 350 °C at rates around 200 Å/hr to minimize any possible clustering effects.

We did not take pains to control exposure of the surfaces to As, since we expected from previous research that As would be present on the surface after Ge growth due to segregation. This expectation indicates that As prelayers are preferred, since obtaining a complete and uniform Ga prelayer is likely to be impossible. This expectation is consistent with the observation that all our Ga prelayer experiments (excepting the exploratory ones with high temperature annealing) resulted in very poor quality GaAs films. Unfortunately, neither of the MBE systems have Auger electron spectroscopy (AES) or X-ray photoemission spectroscopy (XPS), so we had no tool to measure independently the As coverage of the Ge surface. We also expect that the RHEED reconstructions from the clean Ge surface and the As-terminated Ge surface will both exhibit the same 1 x 2 + 2 x 1 reconstructions, so RHEED won't be useful in determining the purity of the Ge surface. Ge growth was initiated immediately after the GaAs wafer temperature had stabilized after ramping down from the higher GaAs growth temperature. Similarly, As prelayers and GaAs growth were initiated immediately after the wafer reached the desired temperature following Ge growth.

3.3.2 Surface smoothing

If domain orientation follows the misorientation of the substrate for nucleation on Ge at 500 °C using an As prelayer, then we can obtain the necessary antiphase film by choosing a wafer misoriented towards $[1\bar{1}0]$. Unfortunately, the atomic step structure of GaAs (001) surfaces misoriented towards $[1\bar{1}0]$ (hereafter denoted as "B" surfaces or steps) is different from that of GaAs (001) misoriented towards the [110] ("A" surfaces or steps) [32-34]. This is in contrast to Ge, where misorientation towards [110] and $[1\bar{1}0]$ is equivalent. This difference caused signficant problems in adapting our strategy to achieve all-epitaxial inversion.

On GaAs, the As-stabilized B steps are more reactive than A steps since they have dangling bonds extending out from the step rather than extending parallel to the step as on A steps. As

a result, A surfaces tend to incorporate Ga atoms at kink sites, which preserves a smooth step structure, while B surfaces tend to grow at the step edges themselves, which decreases step smoothness and regularity [35]. In addition to roughening, the higher reactivity of the B-type steps makes them more likely to react with impurity atoms which then inhibit the subsequent propagation of the step, leading to further roughening [36, 37].

We found the APD quality of the top GaAs layers to be a very sensitive function of the underlying GaAs surface, making the transition from [110]-misorented to $[1\bar{1}0]$-misoriented wafers more complicated than expected. Attempts to duplicate the GaAs/Ge/GaAs heterostructure of Strite on $[1\bar{1}0]$-misoriented wafers resulted in poor quality films with huge APDs extending more than 1 μm through the top GaAs film. After oxide desorption, growth started with a buffer layer of GaAs underneath the Ge to smooth the surface and bury any residual contamination. We used an As_4 flux following Strite, *et al.* because other research had indicated that the GaAs nucleation phase depended on the type of As flux (dimeric vs tetrameric) [15]. We used 350 °C as the Ge growth temperature to avoid clustering effects and performed initial nucleation of GaAs at 500 °C to minimize any Ge clustering while encouraging as much as possible the hypothesized exchange mechanism. The large APD density in the initial films indicated some roughness in the underlying GaAs surface, since only 30 Å Ge growth would not accomplish much smoothing. Preferential etching determined that the films were predominantly single domain, but obviously had very large APDs, evidence of which can be observed in the grooves on the top surface and the very uneven etching of the sidewalls in Figure 3.5. Given the expected sensitivity of top GaAs domain growth to the step structure of the Ge surface and therefore to the step structure of the GaAs, we inferred that the underlying GaAs surface roughness was at fault.

To solve the problem, we first examined growth of 0.5 μm GaAs using dimeric and tetrameric As. On nominally (001) surfaces, the 0.5 μm GaAs films were specular at both 550 °C and 620 °C growth temperatures using both tetrameric and dimeric As (As species were set by the temperature of the As-cracker). In contrast, on wafers misoriented towards $[1\bar{1}0]$, the dimeric As produced a specular surface, while the tetrameric As produced an obviously cloudy surface. Electron microscope observation indicated a high density of small pits across the surface. These results clearly showed that growth using As_2 was necessary to achieve smooth GaAs layers on $[1\bar{1}0]$-misoriented wafers. In contrast, growth of an entire GaAs/Ge/GaAs structure on a [110]-misoriented wafer resulted in smooth layers without pitting or large APDs, indicating that [110]-

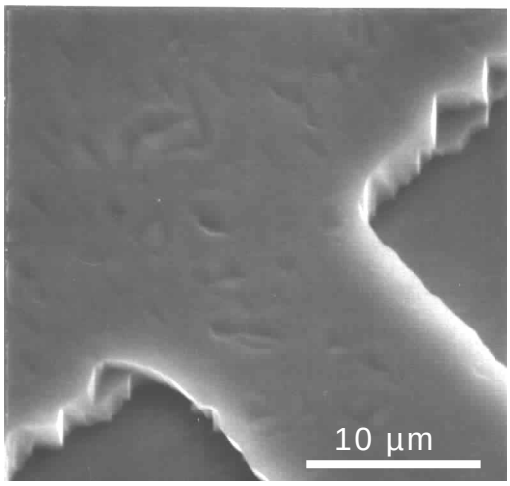

Figure 3.5: 1-µm-thick GaAs film grown on Ge/GaAs containing very large APDs extending through the film. Film has been anisotropically etched to observe the presence and impact of APDs.

misoriented surfaces are much less sensitive to the arsenic species. From this point, we utilized As_2 for growth of layers underneath the Ge, while retaining As_4 for layers above the Ge.

The improvement in the $[1\bar{1}0]$-misoriented surface with As_2 made possible higher quality films that revealed the origin of more APD problems. Suspecting that surface smoothness was still an issue, we placed AlAs marker layers slightly underneath the Ge layer for wafer #126. SEM observation of cleaved films revealed that under each large APD reaching the surface was a ripple in the AlAs layer, as shown in Figure 3.6. Clearly, with a sufficiently large pit or ripple in the GaAs wafer, we could easily have a local misorientation of the Ge surface different from our desired global misorientation, which would promote local nucleation of the undesired phase. Elimination of the GaAs buffer layer under the Ge was not a solution, since a high density of APDs was still observed, presumably because the surface is rough with a high concentration of impurities after desorbing the oxides from the wafer surface.

The solution to this problem involved growth of a superlattice buffer rather than just a simple GaAs buffer. Previous research has demonstrated that superlattices are effective in smoothing GaAs surfaces. This effect is attributed to trapping of contamination at compositional boundaries, and particularly to bonding of oxygen with Al [38]. Introduction of superlattice buffers with 15 periods of (450Å GaAs / 50Å AlAs) with periodic 500 Å AlAs marker layers after every five periods eliminated the rippling underneath the Ge layers along with the associated large

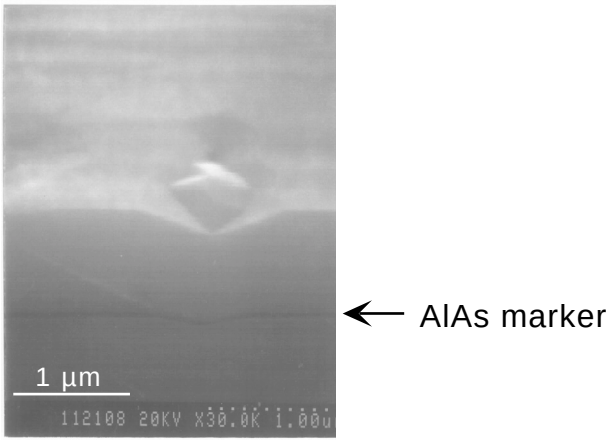

Figure 3.6: Cross-section through isolated APB with underlying AlAs marker layer.

APDs. It is worth noting that while we didn't perform all the same experiments on [110]-misoriented wafers, the fact that the huge APDs weren't observed in the absence of the superlattice means that they are presumably smoother and less susceptible to generation of APDs.

3.3.3 APD size reduction

The orientation of the top GaAs films in GaAs/Ge/GaAs heterostructures were observed both by RHEED and by chemical etching in conjunction with scanning electron microscopy (SEM). The directions of the two and four-fold periodicities in the reconstruction of the As-terminated GaAs surface provide clear indication of the GaAs orientation. Anisotropic chemical etching also allows determination of GaAs orientation, since many etches have large differences in the etch rates on (111)A and (111)B planes. We utilized 1:1:6 (NH_3OH:H_2O_2:H_2O) at room temperature for anisotropic etching, as it has approximately an order of magnitude higher etch rate on (111)B than on (111)A. When a GaAs surface with a photoresist stripe is etched, the cross-section of the etched ridge will develop either an obtuse or acute facet depending on which crystal planes are exposed, as is illustrated in Figure 3.7a. Beyond determining the GaAs orientation, we found that anisotropic etching also provided a convenient method for characterizing APD disorder in the film without resorting to cross-sectional transmission electron microscopy (TEM) examination. Figure 3.7b illustrates etching of a slowly-etching (111)A sidewall which has small (111)B-exposing APDs present at the GaAs/Ge interface. When the etchant reaches the APD, it quickly etches into the fast-etching (111)B APD sidewall, creating a small cave near the Ge layer. Even very tiny disruptions in an otherwise smooth facet can easily be observed at reasonable magnification in an

SEM. A qualitative comparison of the APD size and density can be inferred from the degree of disruption at the sidewall. Note that while this etching reveals the density of APDs and some indication of their relative size, the height of the etched out cave doesn't directly give the APD height. After an APD is etched out, (111)B surfaces will be exposed at the roof of the cave and will cause the disruption to propagate up the sidewall. For this reason comparisons of APD height can reasonably be made only between films of the same top GaAs thickness which have been etched the same length of time. While quantative comparison between films with significant APD densities is not possible, the contrast between films with high densities and low densities of APDs is very clear.

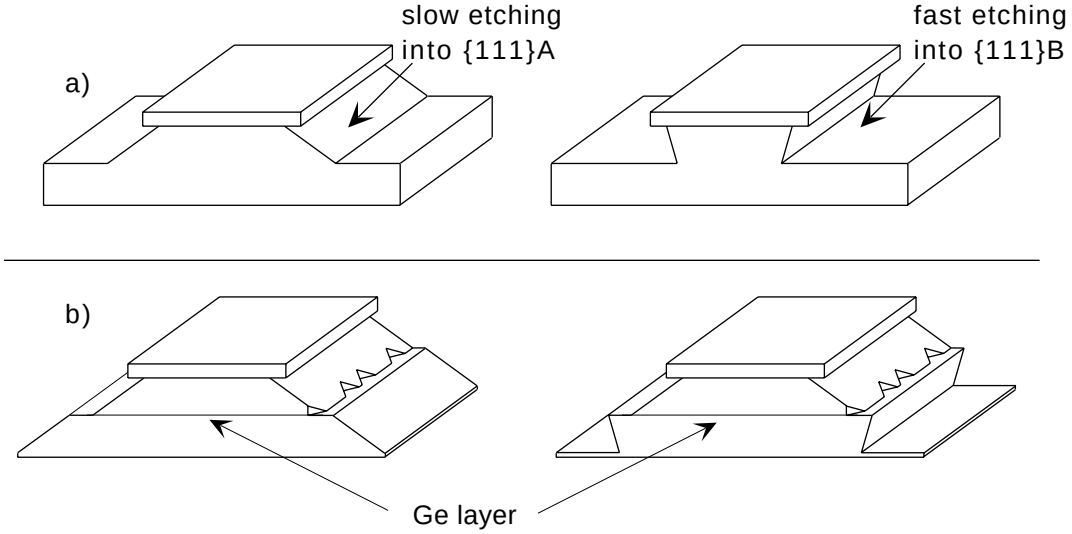

Figure 3.7: Anisotropic profiles for photoresist-masked stripes etched into GaAs. a) shows etch profiles for plain GaAs, while b) shows etch profiles for GaAs films in-phase and antiphase to the GaAs substrate, illustrating effects of APDs.

Figure 3.8a shows etched GaAs facets of wafer #146, which was grown with the aforementioned superlattice buffer layer using As_2. The wafer has 1 μm of GaAs grown on top of the 30-Å Ge layer. The top GaAs layers were grown using As_4 and the first 500 Å were grown at 1500 Å/hr. The pictures show significant disruption of the (111)A sidewall due to APDs. Compare this with Figure 3.8b, which shows wafer #148. Wafer #148 is identical to #146 except that the first 500Å GaAs was grown at 500 Å/hr rather than 1500 Å/hr. One can clearly see that the APD-disrupted region on sample #148 is significantly reduced compared to sample #146, though both were etched for the same amount of time. From this we conclude that the slower initial GaAs

growth rate at 500° decreased the APD disorder. Further reductions in GaAs growth rate down to 180 Å/ hr on wafer # 191 did not make noticeable changes in the appearance of the etched sidewalls. Wafer #171 was grown under the same conditions as #148, but As_2 was employed for the entire structure, both below and above the Ge. While there was no clear effect of the As_2 on etched sidewall appearance and APD density, the films had improved RHEED patterns indicating a very smooth surface and were free from the visible cloudiness which had plagued previous wafers to varying degrees. We therefore utilized As_2 for all GaAs growth from that point onward. Note that we observed the same top GaAs phase for both As_2 and As_4 nucleation and growth under these conditions, which is in contrast to the work of Pukite and Cohen [15].

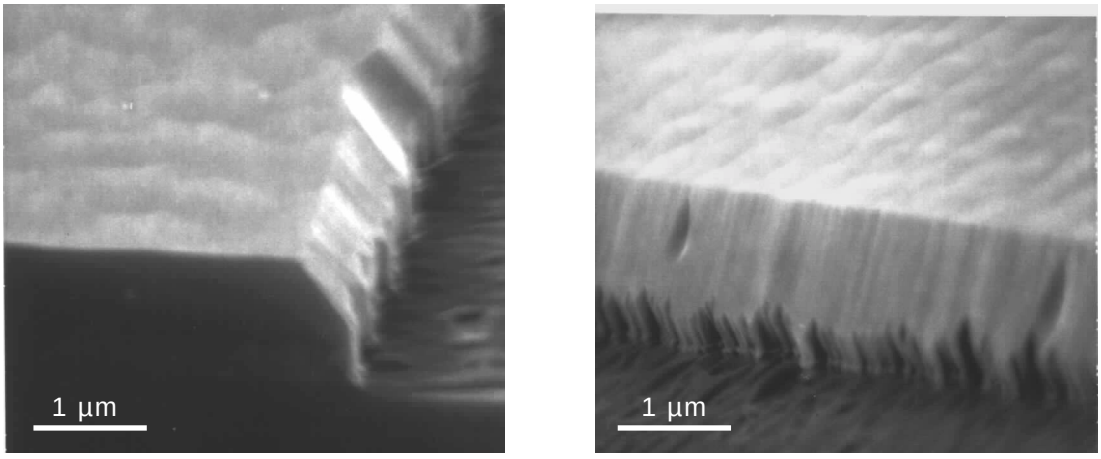

a) wafer #146 b) wafer #148

Figure 3.8: Anisotropic etch profiles of 1-µm-thick GaAs layer grown on Ge/GaAs. a) shows wafer #146. b) shows wafer # 148.

3.3.4 Template recipe

These conclusions about growth rate and As species were incorporated into the template growth recipe ultimately used for fabrication of both the waveguide and bulk nonlinear optical devices. Starting with a GaAs wafer (n-type ~ $2*10^{18}$) misoriented 4° towards $[1\bar{1}0]$, the structure began with a 15-period (450 Å GaAs / 50 Å AlAs) superlattice with three interspersed marker layers of 500 Å AlAs. This superlattice was followed by an $Al_{0.8}Ga_{0.2}As$ etch stop and 100-Å GaAs layer, all grown at 620 °C at typical (~1 µm/hr) MBE growth rates. A 30-Å-thick Ge layer was then deposited at 350 °C at a rate of 200 Å/hr. A 200-Å-thick GaAs layer was nucleated on the Ge surface at 500° with an As prelayer and a growth rate of 500 Å/hr and that layer was fol-

lowed by another $Al_{0.8}Ga_{0.2}As$ etch stop. The thickness of the GaAs layer above the Ge was subsequently extended to 1000 Å when it was found that APDs extended up through the layer and were intersecting the etch stop, causing pitting during template etching. Eventually we placed a 100 Å GaAs cap layer on top of the $Al_{0.8}Ga_{0.2}As$ etch stop to prevent oxidation of the AlGaAs. The $Al_{0.8}Ga_{0.2}As$ etch stop layer thicknesses varied between 100 Å and 500 Å in various samples. Further discussion of the etch stops and the complete template structure appears in Section 3.5 after template etching has been described. This epitaxial structure has proved adequate for seeding orientation-patterned growth of both waveguide and bulk semiconductor devices. The large (1000Å) residual template corrugations necessitated by the remaining APDs have minimal impact on thick film growth, but will cause significant scattering problems in waveguide devices.

3.3.5 Further orientation/APB studies

With a workable template technology in place, further investigations into surface preparation, nucleation conditions and inverted GaAs growth were undertaken to improve the template by further reducing APD density and lowering the template corrugations. We explored the effects of different substrate orientations (misoriented toward [110] rather than $[1\bar{1}0]$), varying nucleation temperatures, varying prelayer type, and annealing samples at high temperatures before GaAs nucleation. The experiments are not sufficiently comprehensive to determine an optimal growth process, but do give significant indications about how best to proceed and demonstrate that better quality inverted films are possible with lower APD densities. Again, many of these results have been discussed previously [39], but are reviewed here with the goal of comparing them in more detail with the literature and drawing conclusions about improving template fabrication processes.

In exploring alternative GaAs nucleation conditions, we cast our net widely. One of the clear complicating issues in our epitaxial inversion process was the possible uncontrolled presence of As on the Ge surface before GaAs nucleation, especially since we had no technique available for characterizing it. Pukite and Cohen observed that high temperature annealing eliminated adsorbed As from a 1000 Å thick Ge film grown on GaAs. As part of our exploration, we included high temperature annealing to explore whether such annealing might improve our APD-related problems. One could imagine it helping in one or both of two ways, either by removing surface As or by altering the surface step structure to enhance uniform GaAs nucleation. It was unclear, however, whether such high temperature annealing with a much thinner (100Å) Ge film would produce clustering. We therefore also performed high temperature annealing with an As flux incident

on the wafer, as we had previously observed that an incident As flux was effective in stabilizing thin Ge films against clustering during high temperature annealing. This effect is likely associated with the observed relative stability of $GeAs_x$ surface layers. We had also observed very low APDs in a few exploratory films which utilized annealing of the Ge surface under an As flux before GaAs growth, so we decided to explore this effect more systematically. In choosing annealing conditions and growth temperatures we were guided by the initial work of Ting, *et al.* and Sieg, *et al.* on GaAs/Ge [24, 27].

The exploratory growth process started with growth of a 1000 Å GaAs buffer layer followed by 100 Å Ge at the usual 350 °C substrate temperature and 200 Å/hr rate on wafers misoriented by 4° towards either [110] or $[1\bar{1}0]$. Next came annealing of the Ge surface at 640°, either with or without an As flux, after which the wafer temperature was lowered to between 350° and 500° for GaAs nucleation with either an As or Ga prelayer. This prelayer was initiated as soon as the wafer reached the nominal GaAs growth temperature. The first 10 monolayers of GaAs were grown by migration-enhanced epitaxy (MEE) at the GaAs nucleation temperature, after which the temperature was ramped to 500 °C if not already there and 1000 Å GaAs was grown by co-evaporation at 1000 Å/hr. Finally, 9000 Å GaAs was grown at 620 °C at 6000 Å/hr to ensure development of a smooth facet during anisotropic etching for examination of the APDs density. The films were examined by RHEED and by chemical etching with the 1:1:6 etch after lithography.

Table 3.1 summarizes the effects on ultimate GaAs phase of varying the growth parameters. The clearest observation is that the GaAs orientation relative to the Ge depends on nucleation temperature. The phase of the top GaAs layer is reversed for nucleation above 400 °C vs. below 400 °C whenever the Ge surface is exposed to As before commencing GaAs growth, whether from the anneal or from the prelayer. The sample nucleated at 397 °C after As exposure is of very poor quality with huge antiphase domains extending through the 1 μm GaAs film, while the samples nucleated at 350 °C and 500 °C are much better, with lower APD densities as determined by anisotropic etching. A number of samples of nucleated at temperatures between 350 °C and 500 °C exhibit APD size and densities that increase with proximity to 397 °C. It appears that there is a critical temperature around 400 °C at which the top GaAs orientation switches domain. To the extent examined, the results are consistent on wafers misoriented towards [110] and $[1\bar{1}0]$, as expected. Additionally, the GaAs phase observed for nucleation at 500 °C is the same as that observed for the previous template process without annealing or MEE. When growth is nucleated with a Ga prelayer after annealing without an As flux, such an orientation change with temperature

is not observed. This observation of opposite phase nucleation at 350 °C on wafer # 363 opens a new possibility for achieving inversion with [110] misoriented substrates in addition to the previously developed inversion process utilizing $[1\bar{1}0]$-misoriented substrates and 500 °C nucleation temperatures. With the greater regularity and smoothness of atomic steps on [110]-misoriented surfaces compared to $[1\bar{1}0]$ misoriented surfaces, it may be possible to achieve lower APD nucleation densities, which would, in turn, make possible thinner template layers and ultimately better performing waveguide devices.

Wafer	Anneal	Nucleation	Prelayer	Substrate misorientation	Tilt of GaAs film phase	Comments
171	none	500 °C co-evap	As	4° to (111)B	(111)A (antiphase)	template recipe
177	with As	500 °C co-evap	-	4° to (111)B	(111)A (antiphase)	comparable to 171
257	with As	500 °C MEE	-	4° to (111)A	(111)A (in phase)	lower APD density
264	with As	425 °C MEE	-	4° to (111)A	(111)A (in phase)	comparable to 257
283	with As	397 °C MEE	-	4° to (111)A	mixed	very poor quality
167	with As	350 °C MEE	-	4° to (111)A	(111)B (antiphase)	large APDs
303	with As	350 °C MEE	-	4° to (111)B	(111)B (in phase)	no buffer - cloudy
365	w/o As	500 °C MEE	As	4° to (111)A	(111)A (in phase)	lower APDs
363	w/o As	350 °C MEE	As	4° to (111)A	(111)B (antiphase)	lowest APDs
353	w/o As	500 °C MEE	Ga	4° to (111)A	(111)A (in phase)	huge APDs
304	w/o As	350 °C MEE	Ga	4° to (111)A	(111)A (in phase)	lower APDs

Table 3.1: Growth conditions for exploration of orientation and APD dependence.

The effects of simply adding the As_2 anneal can be seen in Figure 3.9, which shows the anisotropically-etched cross-sections of wafers grown under a variety of growth conditions. Wafers #171 and #177 were grown on $[1\bar{1}0]$-misoriented wafers using our standard template fabrication process with 500 °C nucleation and As prelayer followed by co-evaporation of GaAs at 500 Å/hr. The only difference between them is that #177 was annealed for 15 mins at 640 °C under an As_2 flux prior to GaAs growth initiation. No significant change in the APD density results from the additional anneal. These wafers illustrate our state of the art with templates grown on $[1\bar{1}0]$-misoriented wafers. Evidence of the APDs begins to appear when we etch to approximately 1000 Å from the Ge surface. Wafer #167 was grown on a [110]-misoriented wafer with As-annealing and nucleation at 350 °C using MEE, and has similar APD disruption on the sidewalls as wafers #171 and #177, indicating that a simple switch to [110] misorientation and reduced growth temperatures doesn't eliminate APDs, though it does achieve inversion. Wafer #264 is identical to #167 except that the nucleation and MEE temperature is 425 °C (wafer # 257 at 500 °C

behaved similarly, but the pictures didn't scan well) and we see a significant decrease in the domain disruption on the etched sidewall, despite the longer etching time. The longer etch time is clear from the greater overall etch depth. The As anneal appears to have improved the APB quality only for nucleation temperatures above the 400 °C critical temperature.

Next we examine the impact of the presence and absence of As during the anneal. We can compare wafer #167 to wafer #363 which had the same growth conditions (anneal 15 mins @ 640°; As prelayer and nucleation at 350°) except that # 363 had no As flux incident on the wafer during the anneal. While there is no impact on the orientation, APD characteristics of # 363 are much better, with no evidence of APD disruption of the etched facet. This is the single cleanest etched facet we have seen on any sample. It is more impressive because this sample was deeply etched, approximately 1 μm into the GaAs underlying the Ge, which means that any APD disorder present should have propagated a large distance up the facet. Additionally, the top film is clearly inverted with respect to the substrate, so that this same process could produce an orientation template. In this case, the absence of As during the annealing significantly improved the APD quality of the GaAs film.

For films nucleated above the critical temperature, at 425 °C or 500 °C, the difference between annealing with and without As is less clear. Wafers #257 (500 °C) and #264 (425 °C) received an As flux during the 640° anneal, while wafer #365 (350 °C) did not. The wafers have roughly comparable APD densities and magnitudes, indicating that the As presence during annealing had less impact for higher temperature nucleation. The high quality of several films annealed without As indicates that clustering of the 100 Å Ge films during annealing was most likely not a problem, but this issue was not investigated independently. We observed only that RHEED examination of the surface after anealing didn't reveal any signs of 3-D surface features or clustering. It seems highly unlikely we could have obtained an inverted film, let alone one with the domain quality of # 363, if any significant mass atomic migration or clustering were occurring during annealing.

Finally, samples were grown using Ga prelayers instead of As prelayers at both nucleation temperatures. Obviously, a uniform Ga prelayer is only possible when As is absent during the annealing step. As Figure 3.9 shows, the sample #304, which had 350 °C nucleation with a Ga prelayer, is of much better APD quality than sample #353, which had 500 °C nucleation with a Ga prelayer and contains enormous APDs which even reach the surface in some places.

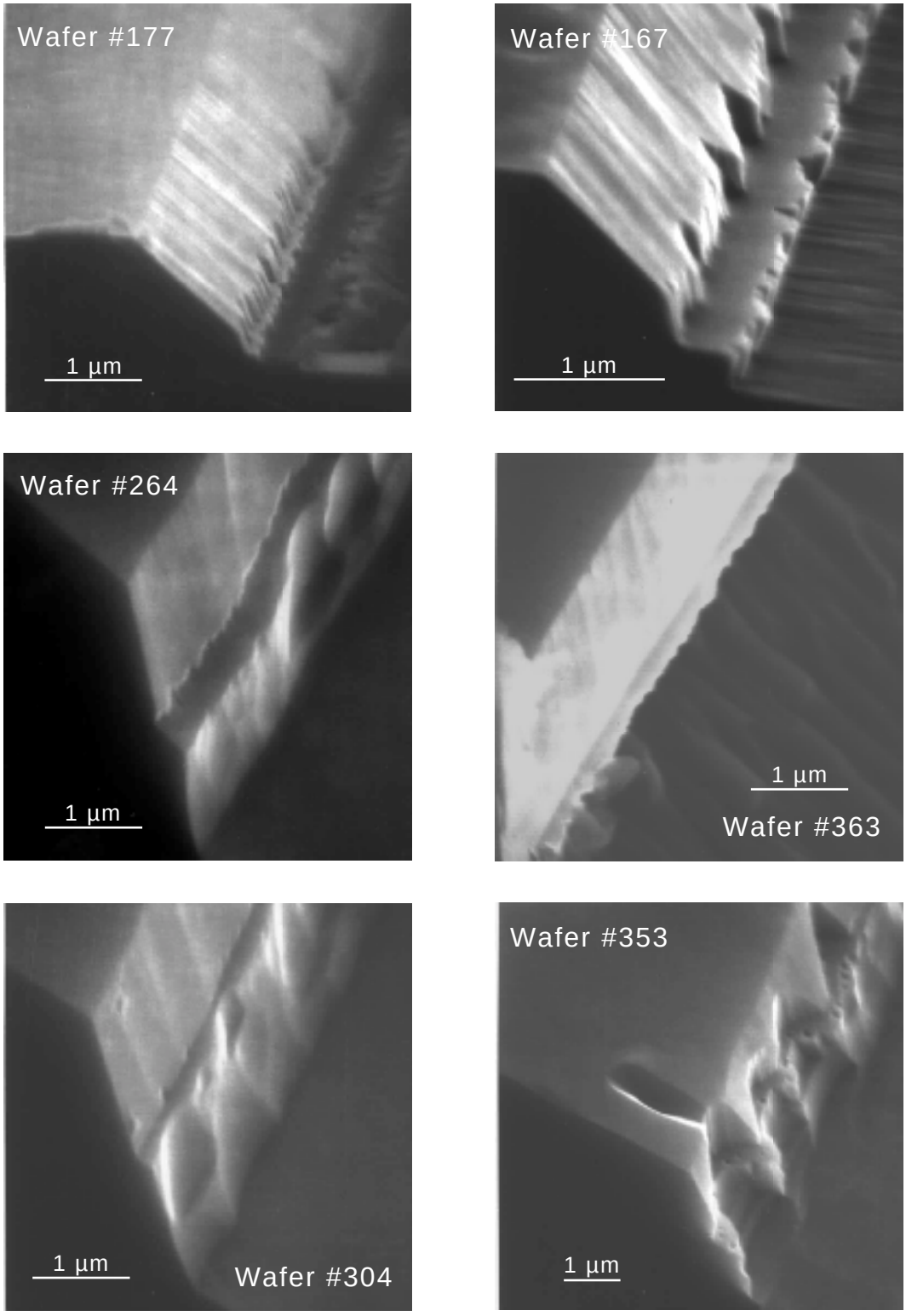

Figure 3.9: Etched sample cross-sections showing APD densities for various wafer misorientations and growth conditions.

A number of empirical conclusions can be made from this incomplete data set. Nucleation using MEE doesn't change the orientation of the top GaAs film. All samples with Ge surfaces intentionally exposed to As exhibit an orientation reversal as a function of nucleation temperature. Annealing under As_2 leads to improvements in the APD density only at 500 °C nucleation, while annealing without As improves APD density for nucleation at 350 °C. Nucleation with Ga yields better results at 350 °C than at 500 °C and no orientation reversal is observed with temperature. Overall, we see lower APD densities on several films with [110]-misoriented substrates, As-free annealing, and 350 °C nucleation, but can't determine the individual effects of each factor from the limited set of experiments performed.

3.3.6 Thin buffer exploration

In the interest of fabricating templates using the lift-off process outlined in the introduction, we also attempted to grow inverted GaAs films using much thinner superlattice buffer layers under the Ge. When using a lift-off technique, the entire film thickness grown while the mask is in place contributes to the ultimate template corrugation. Our optimized inversion process on GaAs wafers misoriented towards $[1\bar{1}0]$ described above required a 1-µm-thick GaAs/AlGaAs superlattice for smoothing, which would produce a ridiculously large corrugation in the orientation template and very poor quality regrown layers. We tried to produce a thinner (~ 500 Å) buffer structure which would smooth the wafer surface sufficiently to allow growth of Ge and inverted GaAs with acceptable APD quality on top. We tried thin layer superlattices (50Å GaAs / 30 Å AlGaAs) and migration enhanced epitaxy, both separately and in combination. Unfortunately, all attempts to grow inverted GaAs films using these thin buffers on $[1\bar{1}0]$-misoriented wafers appeared cloudy to the eye, an indication we previously correlated with a high density of antiphase domains. Note that such a cloudy appearance is only visible once several thousand Ångstroms of inverted GaAs have been grown. While the APD disorder is present from the initiation of growth on Ge, only after some amount of GaAs growth does evidence of the resulting surface roughness become visible to the eye or under an optical microscope. None of the films obtained by this process was of sufficient quality for incorporation into a useful template for subsequent regrowth. The roughening associated with growth on $[1\bar{1}0]$-misoriented wafers is probably responsible for much of the APD disorder. If epitaxial inversion processes on the generally smoother [110]-misoriented surfaces were perfected, thin buffer structures might become feasible and allow lift-off template strategies.

3.4 Epitaxial inversion: Discussion

This section will compare our observations with those of the literature in more detail, speculate about possible explanations, then make recommendations for future research. There are three major points of comparison between our work and others': APD disorder, orientation, and As-exposure effects.

3.4.1 APD disorder

The results of Strite, *et al.* [29] are again the easiest to compare with ours with respect to the antiphase disorder. They report antiphase-domain-free layers from the beginning of growth for 500 °C nucleation with As prelayers on (111)A misoriented wafers. While showing some evidence of 3-D growth initially, their RHEED patterns after 100 Å GaAs growth indicate only a single 2 x 4 reconstruction which is highly improved and streaky. Cross-sectional TEM examination of these films revealed no evidence of APDs. Nucleation under the same conditions but with Ga prelayers produced a visible density of APD at the GaAs-Ge interface as observed by TEM, a result which was attributed to incomplete prelayers. In contrast, anisotropic etching of our films nucleated at 500 °C with As prelayers using $[1\bar{1}0]$ wafers reveals a layer of APD defects at the GaAs-Ge interface. Without the smoothing superlattice, this APD disorder can extend through 1 μm of the GaAs film, while with the buffers it is confined to a region of <1000 Å above the Ge. We have observed RHEED evidence of APDs during the initial stages of growth and of their annihilation during subsequent growth, but find that anisotropic etching provides much more easily interpreted results. In contrast, many of our exploratory growths on wafers misoriented towards [110] have much lower APD densities with only occasional evidence of an APD in the etched cross-section, even in the absence of any smoothing superlattice. As a result, it is likely that much of the difference between our results and those of Strite, *et al.* result from the use of $[1\bar{1}0]$- vs. [110]-misoriented wafers, which is not surprising given the roughening nature of the GaAs B surface steps. Pukite and Cohen [15] also grew on [110]-misoriented wafers and so may have had the advantage of the A-step smoothing behavior when they observed APD-free GaAs from the initiation of growth. Additionally, after growing the 1000-Å-Ge layer, any effects of the underlying GaAs surface would likely be mitigated by the more isotropically growing Ge.

Ting, *et al.* [24] also investigated GaAs growth on misoriented and unannealed Ge wafers containing two-domain surfaces and a majority of single steps. These results were published after the majority of our investigations into epitaxial inversion were completed, so we did not take

advantage of them in designing our experiments. RHEED patterns before GaAs growth showed the mixed 2 x 1 + 1 x 2 surfaces expected from an unannealed bulk Ge surface. However, they observed dramatic differences between GaAs films when the nucleation temperature was varied between 350 °C and 500 °C. GaAs nucleated at 500 °C with As prelayers had high APD densities which varied dramatically across the surface of a single wafer, with some regions having APDs that annihilated after ~ 1000Å, while other regions had many APDs extending through 1 μm of GaAs. The variation in size and density of the APDs across the wafer was attributed to disparities in initial APD nucleation density due to an uncontrolled variable in the experiments, which the authors suspect is the duration and pressure of the As_2 flux. In contrast, films nucleated at 350 °C had "a conspicuous absence of APDs" as observed by both plan-view and cross-sectional TEM, exhibiting only a few scattered APDs and none of the huge APDs. Their results point to the potential importance of the surface As exposure conditions as a factor in determing the quality of the GaAs film, a topic which will be taken up in more detail in section 3.4.3.

3.4.2 Orientation

For GaAs nucleation at 500 °C on misoriented substrates with no annealing, we see the same behavior as Strite, *et al.* [29] growing GaAs/Ge/GaAs heterostructures. They observe GaAs films in phase with the substrate on [110]-misoriented wafers and we confirm that the GaAs film orientation follows the Ge surface misorientation, obtaining antiphase films for growth on $[1\bar{1}0]$-misoriented substrates under the same growth conditions. Their paper doesn't specify whether As_2 or As_4 was used for the prelayer, but we observe the same GaAs phase for both As_2 and As_4 prelayer species for 500 °C nucleation. This independence of prelayer species differs from the observation of Pukite and Cohen [15], who grew GaAs/Ge/GaAs heterostructures on much thicker 1000Å Ge layers with 500 °C nucleation and observed opposite GaAs phases for nucleation using As_2 and As_4 on Ge surface. They observed that exposure to As_4 resulted in the two-fold reconstruction with the electron beam oriented down the Ge surface staircase, while As_2 produced a twofold reconstruction with the beam directed perpendicular to the staircase. Our results with As_2 and As_4 take the orientation of Pukite's As_4 case, which is the same as the observation of Strite, *et al.* Sieg, *et al.* [27], working with annealed, double-stepped Ge surfaces and nucleating at 350 °C, observed that As_2 and Ga prelayers produced one phase, while As_4 prelayers nucleated the opposite phase, again observing domain rotation for the different As species. This differs from our observation that Ga and As_2 prelayers nucleated at 350 °C after high temperature annealing pro-

duce opposite GaAs phases. Interestingly, Sieg, *et al.* observe exactly the opposite dependence on prelayer as Pukite and Cohen, with As_2 producing a two-fold reconstruction with the electron beam oriented down the Ge surface staircase and As_4 producing the two-fold looking perpendicular to the staircase. We unambiguously observe a reversal in GaAs orientation between nucleation temperatures of 350 °C and 500 °C for As prelayers on annealed Ge layers, which may reconcile to some degree the apparently contradictory observations of Pukite and Cohen compared to those of Sieg, *et al.* regarding As prelayer-initiated growth at 500 °C and 350 °C, respectively. Our results also appear to be consistent with the results of Koh, *et al.* [8] who observed GaAs inversion with Ge buffer layers using $[1\bar{1}0]$-misoriented GaAs wafers nucleated at 580 °C with an As prelayer.

3.4.3 Complications from arsenic exposure

The observed differences in APD and orientation behavior between our results and those of other researchers may also complicated by unintentional As-exposure of the surface before initiation of GaAs growth. Both Strite, *et al.* and Pukite and Cohen report that the Ge surfaces were As-free before initiation of GaAs growth. In contrast, we had no tools for observing the chemical composition of the surface (AES or XPS) and reasonably suspect the surfaces contained some As given the many observations of As segregation during Ge growth on GaAs reviewed in Section 3.2.1. While it might seem that unintentional As exposure of a Ge surface before intentional exposure with an As prelayer would not be important, since a uniform prelayer would be obtained in either case, there are indications that unintentional As exposure may have additional complicating effects. These effects go beyond the previously described reversible changes in step structure upon exposure to an As flux observed in single-stepped Ge surfaces [15].

Unfortunately, there has been very little direct investigation into As-exposed Ge surfaces, so one can only extrapolate from observations of Si surfaces exposed to As and the chemical similarity of the two materials. Several experiments have found that the surface reconstructions of As-exposed Ge surfaces depend on temperature and As flux. On Si double-stepped, single-domain surfaces with adsorbed As, a 2 x 1 reconstruction was observed by RHEED at low temperatures (< 450 °C) and a 1 x 2 reconstruction was observed at high temperatures (> 600 °C) by Kawabe, *et al.* [40]. Becker, *et al.*[41] observed by scanning tunneling microscopy (STM) a similar reversal of the surface reconstruction between a 1 x 2 at 400 °C and 2 x 1 at 600 °C, though the observed reconstructions are opposite of those of Kawabe, *et al.* for the same temperatures. The detailed

investigations of Bringans, *et al.* [42] explain this discrepancy as the result of kinetic limitations and reveal the complexity of As-exposed Si surfaces.

Bringans, *et al.* performed a well-controlled series of experiments in which double-stepped Si surfaces were exposed to As at various temperatues ranging from room temperature to the approximate As-desorption temperature around 700 °C. They then examined the surfaces by low energy electron diffraction (LEED) and measured the ratios of the two possible As-Si surface reconstructions, 1 x 2 and 2 x 1. They observe that the surface reconstruction is a function of the temperature at which the surface is first exposed to As, with predominantly 1 x 2 observed for initial exposure temperatures below 350 °C, a mixed reconstruction for temperatures between 350 °C and 400 °C , and predominantly 2 x 1 for initial exposure temperatures between 400 °C and 600 °C. For first exposure over 650 °C a mixed domain surface is again observed along with As desorption from the surface. Interestingly, once locked-in at the initial exposure temperature, the corresponding reconstruction is stable upon annealing up to 650 °C - 700 °C. The explanation given for this behavior is that while the higher temperature (2 x 1) reconstruction is the lower energy configuration, kinetic limitations on transformation of the reconstruction and step structure can preserve the higher energy 1 x 2 reconstruction at higher temperatures. Examining the bonding configuration at the surface, they find that the 1 x 2 surface reconstruction can occur by simple bonding of As dimers directly on the original double-stepped Si surface, but obtaining the 2 x 1 reconstruction requires rearrangement of the Si surface by mass-migration, since only 1 monolayer of As is observed on the surface by XPS. This implies that exposure to As between 400 °C and 600 °C catalyzes the migration of half of the surface Si atoms to achieve the 2 x 1 reconstruction, which has a double-stepped Si surface but with the opposite terrace exposed as the original Si surface. Finally, but perhaps most importantly, they observe that when GaAs is grown on the As-exposed, double-stepped Si surface, the ultimate GaAs orientation follows the surface reconstruction set during initial As exposure, independent of the subsequent GaAs nucleation and growth conditions. The orientation of the GaAs film is thus determined by the As exposure history of the Si surface, not by the explicit GaAs nucleation and growth conditions.

I discovered the Bringans, *et al.* reference while preparing this dissertation, so we were not able to take advantage of its conclusions in the design of our exploratory inversion experiments. This is unfortunate, in retrospect, because if the Ge surface behaves at all similarly to the Si surface, this model would have made and will in the future make possible much better directed exploratory growth experiments. Expecting unintentional As exposure of the surface but not subsequent hysteretic behavior of the surface reconstruction with temperature, we took no pains to

control factors which may turn out to be critical for determining both the orientation and APD density. The model is, however, immediately helpful for speculatively interpreting our and others' experimental results. The rotation of the top GaAs phase and our observed critical temperature could be explained by such As-exposed Ge surface reconstructions. The transition between the reconstructions could be kinetically limited at these temperatures like Si, or it could be in equilibrium and reversible. All the exploratory samples were annealed at 640 °C, some under As flux and others without an As flux, before cooling to the nominal GaAs nucleation temperatures between 350 °C and 500 °C. Our clear observation of rotation for different nucleation temperatures would seem to argue for a reversible process rather than a kinetically-limited one, at least in this temperature range. Note that the same orientation behavior was observed for annealing both with and without As, so the presence or absence of As at the anneal temperature doesn't seem to have changed the dominant reconstruction. The improved domain quality on the As-free annealing samples might indicate some improved homogenization of the surface reconstruction, but it may also just reflect [110]-misoriented surface smoothness, as discussed above. Though interpretation along these lines is appealing, it is important to remember that our surfaces, unlike those of Bringans, *et al.* had mixed domain terraces and single atomic steps which might behave very differently than single domain, double-stepped surfaces.

Ting, *et al.* [24] propose that the As-exposed Ge surface exhibits similar behavior to the As-exposed Si surface with a transition in the surface structure that occurs around 500 °C. This proposal is then employed to explain the much higher APD density present in their films grown around 500 °C, either because the transition is to a mixed domain surface, or because the transition to a new state was kinetically limited at 500 °C. This explanation could also reconcile the apparently contradictory results of Pukite and Cohen and Sieg, *et al.* regarding the prelayer dependence of the final GaAs orientation, since they nucleated at 500 °C and 350 °C, respectively. Clearly, more knowledge about the behavior of As-exposed Ge surfaces and their temperature-dependence will be extremely important for intepreting the results of these and future GaAs/Ge growth experiments.

3.4.4 Recommendations

From the results of our experiments and suggestions out of the associated background literature, we can make some recommendations about how best to proceed in improving the epitaxial inversion process. The most promising short-term route for improving template fabrication would involve a combination of [110]-misoriented substrates and 350 °C nucleation. We have demon-

strated that films grown under these conditions can achieve inversion with relatively low APD densities, and other research also finds a relative resistance to APD formation for these conditions. The inherently smoothing properties of type-A steps should be helpful in producing a smooth, uniform Ge surface that should assist APD suppression. If successful, this process might allow lift-off templates with shallow backetching, which would give a very elegant template process and reduce corrugation amplitudes from those possible in etched template schemes. However, this approach is finally purely empirical, not one which is based on a fundamental understanding of the factors controlling inversion or APD formation. Given the probable dependence of the Ge surface step structure on As exposure conditions and the subsequent dependence of orientation behavior and APD density on this Ge surface, any real understanding of these processes will require systematic investigation into the reconstructions and thermal behavior of As-exposed Ge films. Such an investigation need not reproduce all the detail in the literature regarding As-exposed Si surfaces, but should determine the dominant reconstructions as a function of thermal and As exposure history. It could be performed on bulk Ge surfaces originally, where there would be no complications from unintentional As exposure, then compared to results using Ge films. A number of questions left unanswered by the literature could be resolved in these experiments, including whether it is possible to obtain a double-stepped, single-domain reconstruction on a thin Ge film by high temperature annealing or by As-enhanced mass migration effects. Finally, obtaining such a double-stepped Ge surface is probably the only way to eliminate APD disorder with its deleterious effects on film morphology and frequency conversion performance, particularly for waveguide devices.

3.5 Template etching

Several features are desirable in the processes used to pattern the inverted GaAs and form the template. First, it should ultimately allow minimum waveguide corrugation amplitudes to minimize waveguide losses. In addition, the fabrication process should be scalable from larger corrugation to very thin corrugation so that one can take advantage of reductions in APD height without requiring development of a new process. We also need to leave a clean surface in the trenches and on top of the ridges to achieve high quality MBE regrowth.

These goals must be achieved in the face of several potentially problematic factors. Bulk measured etch rates are generally given for much deeper etches where the effects of any surface impurities, non-equilibrium conditions at the beginning of etching, and immersion/removal are mitigated by the long etching times. Etching of very thin layers (< 1000 Å) can often be unpre-

dictable and difficult to reproduce. Layers of oxide and other impurities on the wafer can slow the initial etching rates significantly below the bulk etch rate. Often a definite etch rate can only be measured after achieving an equilibrium between the various adsorption, reaction, dissolution and diffusion mechanisms. Immersion and removal effects can also affect shallow etching disproportionally. Accurate measurement of very thin etch depths is also more difficult than for deeper etches. Additionally, the presence of APDs at the top GaAs/Ge interface in our template samples will have unpredictable effects if etching cuts through the GaAs and Ge layers. We observed etching inhomogeneities such as pinholes and roughened layers on GaAs/Ge/GaAs heterostructures which were correlated with the height and density of APDs.

Since these problems become more complicated as one tries to etch shallower trenches, we ruled out simple etching through the GaAs/Ge/GaAs heterostructure as both unscalable to very small corrugations and unsuitable for producing the smooth surfaces required for regrowth. We developed two alternative solutions to the patterning problem, one of which utilized masked epitaxial growth and another which utilized selective etching and etch stops. We demonstrated both, but concentrated on the etch-stop solution for reasons which will become clear as the discussion proceeds.

3.5.1 Lift-off templates

The first approach is to use some kind of in-situ mask to pattern the Ge and overlying GaAs layers during epitaxial growth. The mask would be placed on or adjacent to the surface so that epitaxial growth would occur only in the mask openings, after which the mask would be removed to expose the underlying GaAs substrate. This mask would have micron scale grating features and would have to be aligned to the GaAs over a wide temperature range to insure that the Ge and GaAs layers ended up in the right place. In an ideal world, this mask would be removable in-situ after growth of GaAs/Ge/GaAs so that regrowth could proceed without exposure to atmospheric contamination. Unfortunately, we couldn't figure out such an in-situ removal scheme, so we had to rely on ex-situ mask removal and lift-off of the unwanted GaAs/Ge layers. The most obvious choices for easily depositable, patternable and removable materials compatible with UHV epitaxial growth are silicon dioxide and nitride. Both dissolve in HF-containing solutions, while GaAs does not in the absence of an oxidizer like H_2O_2. With a patterned oxide or nitride layer on the GaAs surface, epitaxial GaAs grows in the mask trenches while polycrystalline GaAs grows on the mask surface. This polycrystalline film then needs to be etched away or be lifted-off in conjunction with removal of the masking layers.

We made a number of increasingly sophisticated attempts to test the lift-off of these layers. The first utilized a 1000 Å thick oxide layer which was patterned using photoresist and etching in 6:1 BOE. After resist removal in acetone, 3-solvent cleaning, and an oxygen plasma descum to remove carbon, we etched the exposed GaAs for 40 sec using 3:1:50 H_3PO_4:H_2O_2:H_2O to etch an approximately 500-Å-deep trench into the GaAs. This rate-limited etch is one of the best for etching very thin trenches. The goal of this etching was to pre-compensate for the thickness of the smoothing layers below the Ge and achieve a template with nominally no corrugation. This wafer was then rinsed and loaded into the MBE chamber where 500 Å of GaAs/AlGaAs were grown by a combination of MEE and co-evaporation. After removal from the MBE, the liftoff was performed by soaking in 6:1 BOE. We observed that the majority of stripes tended to stick down instead of lifting off, even when surfactants were added to the BOE. The unsupported polycrystalline GaAs films originally deposited on the subsequently dissolved oxide layer were very susceptible to disintegrating and spreading debris across the wafer. Ultrasonic agitation to encourage liftoff made this debris problem much worse.

As a result, we tried a different strategy with strained silicon nitride layers. By including two Si_3N_4 layers of different strain on top of a SiO_2 release layer, we created a structure that would intrinsically curl up once the SiO_2 layer was etched away. This moved the stripe out of the fluid flow boundary layer next to the wafer and up into the flow where it could easily be flushed away. Additionally, the polycrystalline GaAs would now be supported on the intact Si_3N_4 layers to minimize any disintegration and associated debris. The liftoff dielectric structure is shown in Figure 3.10 and consisted of 1000 Å of SiO_2, 2500 Å of low stress Si_3N_4, and 3500 Å of tensile-strained Si_3N_4. Photolithography was used to define stripes across the surface, after which CF_4 plasma etching was used to etch through the nitride layers and halfway through the oxide layer. Dry etching was used to preserve the width of the trenches in the dielectric structure which otherwise would have widened during etching through the Si_3N_4. To prevent exposure of the GaAs surface to the flourine-contaning plasma and any associated regrowth complications, we used 6:1 BOE to etch through the remaining oxide and expose GaAs in the trenches. The sample was prepared for regrowth in the same way as the oxide samples. In this case the strained nitride layers worked as expected with virtually all features lifting off except where they were too wide for the 6:1 BOE to undercut completely in the time allowed. The only undercut lines remaining on the surface were pinned in place by lithography defects which weren't undercut completely during the 6:1 BOE etching. The undercut distance of the 1000 Å SiO_2 layer in 6:1 BOE was around 35 μm in the first

hour and 55 μm after the second hour. When the sample was flushed with BOE uniformly to remove the curled-up stripes, this process produced very clean samples with only a few localized remaining line segments which were always clearly attached to regions with lithography defects. A small amount of ultrasonic agitation was useful for removing the maximum number of these segments. This strained nitride liftoff process itself worked very well for patterning simple GaAs films.

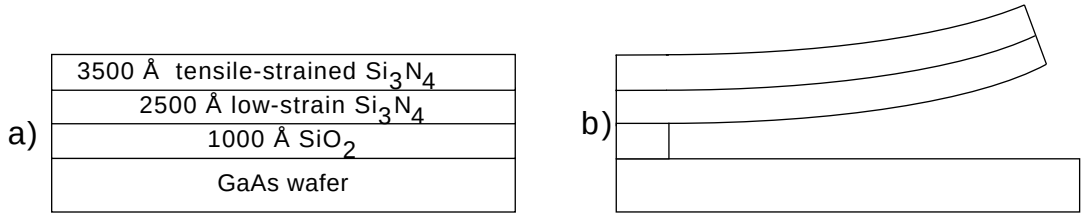

Figure 3.10: Schematic diagram of strained nitride dielectric liftoff structure a) before and b) after undercutting.

Unfortunately, we never observed high quality MBE regrowth on GaAs surfaces which had been exposed to SiO_2. The GaAs films had a visibly cloudy appearance and SEM examination showed significant surface roughening, even after 1 μm MBE regrowth. The origins of this roughening were not determined. Additionally, as discussed in Section 3.3.6, attempts to grow high-quality inverted GaAs films using only thin (500 Å– 1000 Å) GaAs buffers underneath the Ge layers yielded poor quality films with large APD densities and cloudy surfaces. As a result, we did not combine the lift-off mask and inverted GaAs growth to make an orientation template, as it would clearly have resulted in templates of poorer quality than those we obtained by other techniques. However, if an alternative template fabrication processes can eventually produce smoother layers utilizing very thin GaAs buffer layers and issues with regrowth on oxide-masked surfaces can be addressed, such a lift-off process could be an elegant method for fabricating a template with no nominal corrugation.

3.5.2 Etch-stop templates

The alternative to using a lift-off process is employing etch stops. The advantage of this method is that one can easily achieve very precise corrugation heights and nominally smooth surfaces after etching by stopping the etch on layers which are defined during MBE growth. This

approach mitigates the previously disussed issues of shallow etching and nonuniformities associated with APDs. Also, it solves a problem caused by the relative etch rates of Ge and GaAs. All wet etches we investigated (peroxide-based, varying pH from 1 to 14) had significantly higher etch rates (> 3x) for GaAs than for Ge. The presence of the more etch-resistant layer on top of a less-resistant layer will produce a "badlands" effect. Small variations in etching through the Ge layer will cause much larger roughing in the GaAs layer. In general, we found the literature on Ge wet chemical etching both sparse and often unreliable. By moving to etch-stops we ensured that the etched trenches would be smooth regardless of the relative GaAs and Ge etch rates. Such etch-stops could be used in combination with either wet or dry etching processes, though we only used them with wet etching. Note that selective etching of Ge over GaAs should be possible using fluorine-containing plasmas, but we were reluctant to complicate our fabrication process by involving another complicated piece of equipment with uncertain operational duty cycle. In principle, though, use of dry etching could allow extremely thin corrugations and clean surfaces for regrowth.

Given the sources available in our MBE system, the obvious candidate for etch stops is clearly high-aluminum-fraction AlGaAs, which has high selectivity in both directions relative to GaAs using different etch solutions. The more constrained problem of the two is finding a hydrogen-peroxide-containing etch that will stop on AlGaAs layers after etching through GaAs and Ge. Two candidates have been used previously, the NH_3OH:H_2O_2 system and the citric acid:H_2O_2 system. The NH_3OH:H_2O_2 system is very sensitive to pH and only offers limited selectivity [43, 44]. In contract, selectivities of up to 1450 to 1 for etching GaAs over AlAs have been demonstrated with citric acid/hydrogen peroxide mixtures of 4:1 citric acid: hydrogen peroxide (1:1 citric acid monohydrate: water by weight; 30% H_2O_2) [45, 46]. The high selectivity is attributed to the low solubility of Al_xO_y in the citric acid solution. The AlGaAs layer oxidizes quickly, but dissolves slowly, protecting the layers beneath. Carter-Coman discusses complications due to film stress using this process for thick AlGaAs layers [47], but that is unlikely to be an issue for our desired thin layers. GaAs etch rates with the 4:1 solution are measured to be ~ 4000 Å/ min, while the Ge etch rate is on the order of 500 Å/min.

Finding etchants to remove AlGaAs while not etching GaAs is not difficult. Many acids such as HCl, HF, and H_2SO_4 will dissolve AlGaAs with aluminum fractions greater than 0.4, which corresponds roughly to the direct to indirect transition in the bandgap. We chose 1:1 HCl(30%):H_2O for template etch stop removal to avoid the complications of using HF solutions.

Unfortunately, the etch rate is low, around 500 Å/ minute for $Al_{0.7}Ga_{0.3}As$. The rate can be increased by adding H_2O_2 [48], but the addition of an oxidizer enables GaAs etching in the same solution and so is not suitable for our application. More complicating was the non-uniform dissolution across the surface of the wafer. Empirically we found that two process details were necessary for uniform AlGaAs removal. The first was agitation of the etchant or sample by swirling the beaker. The second was always blowing dry the wafer surface before immersion in the $HCl:H_2O$. No such dependence on process detail was observed with the citric acid/hydrogen peroxide etch, which was very robust and always uniform. The color of the wafer surface was always monitored during AlGaAs removal to check on uniformity. With the proper attention to process detail we could obtain uniform AlGaAs removal from the surface when viewed either by eye or under a microscope.

Despite apparently uniform AlGaAs removal, however, strange effects occurred repeatedly on nominal GaAs surfaces after removing overlying AlGaAs etch-stop layers. The trenches looked entirely clear and clean, but after ~ 30 minutes small bright points visible through an optical microscope would appear across the surface in high density. These points would grow in size over several days until they could be observed as microscopic faceted crystallites, the density of which varied dramatically across the surface of a wafer. These particles were present in some density regardless of the thickness of the AlGaAs layers before removal. Fig 3.11 shows an SEM micrograph of an etched template with nominally removed AlGaAs and a high density of the unknown particles on the surface. On template wafers these particles tended to nucleate on the orientation stripe sidewalls, as seen in Figure 3.11. All attempts to extend etching time or use alternative etchants (HF, H_3PO_4, H_2SO_4) left a similar residue except for boiling H_2SO_4, which removed the residue but left a severely pitted wafer surface. Under microscopic observation it appeared that there was an originally uniform, red-yellow film across the surface of the GaAs which then coalesced to form the particles, eventually crystallizing, perhaps as the films dried. When wafers with this contamination were subjected to MBE regrowth, the resulting films suffered from a haziness which varied across the wafer surface. Microscopic examination of the surface revealed enhanced roughness and pitting compared to regrowth on plain GaAs.

We performed XPS analysis of the nominal GaAs surface immediately after overlying AlGaAs removal to determine the composition of this undesired residual film. The surfaces were examined by XPS immediately after loading into the vacuum system, then ~ 5 Å of material was removed from the wafer surface by sputtering with Ar+ before re-examination of the surface by

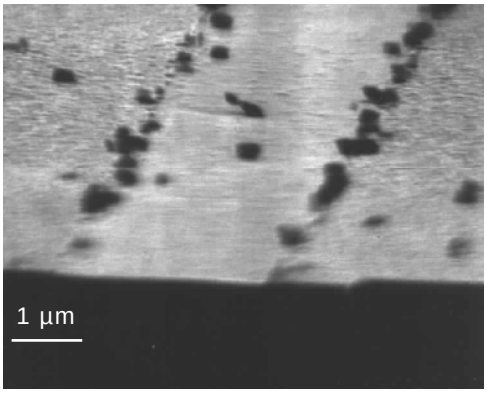

Figure 3.11: Al-O particles on template surface after nominal AlGaAs removal.

XPS. Repeating this removal and examination, we mapped the composition of the near-surface region as shown in Figure 3.12a. The concentrations were obtained by integrating under the 3p peaks for various elements. There is a clear enhancement of aluminum and oxygen concentrations in the near-surface region compared to plain GaAs wafers. It is not clear whether the decrease in signal with depth is due entirely to sputtering removal of atoms from the surface or whether contaminant coalescence into particles might also contribute by reducing the fraction of the surface covered by Al-O compounds. In either case, however, excess Al and O are clearly present and will cause regrowth problems, as Al-O compounds, unlike Ga-O and As-O compounds, are not volatile at typical MBE growth temperatures and so will not desorb from the surface.

Many attempts were made to remove the Al-O scum layer, but the only successful route found to date resulted from a random conference discussion [49]. Following this suggestion, we found that a 15 sec dip of the surface into H_2O_2 after the AlGaAs etch and before drying the film, followed by another 10 sec dip into HCl was sufficient to remove the contamination layer and eliminate particle formation. The dip times were not optimized and much shorter times might be just as effective. XPS depth-profiling analysis of a template surface after the additional H_2O_2 and HCl dips is shown in Figure 3.12b.

Here we see no indications of Al above the ~ 5% noise level for our integration time. The oxygen signal drops very quickly to the noise while the Ga and As signals rise quickly to the expected 50% values. While we don't understand precisely the effect of the H_2O_2 dip, we can gain some insight by examining the solubility of various Al-oxide and hydroxide compounds. Table 3.2 shows the solubilities of various Al and O containing compounds in acids and bases.

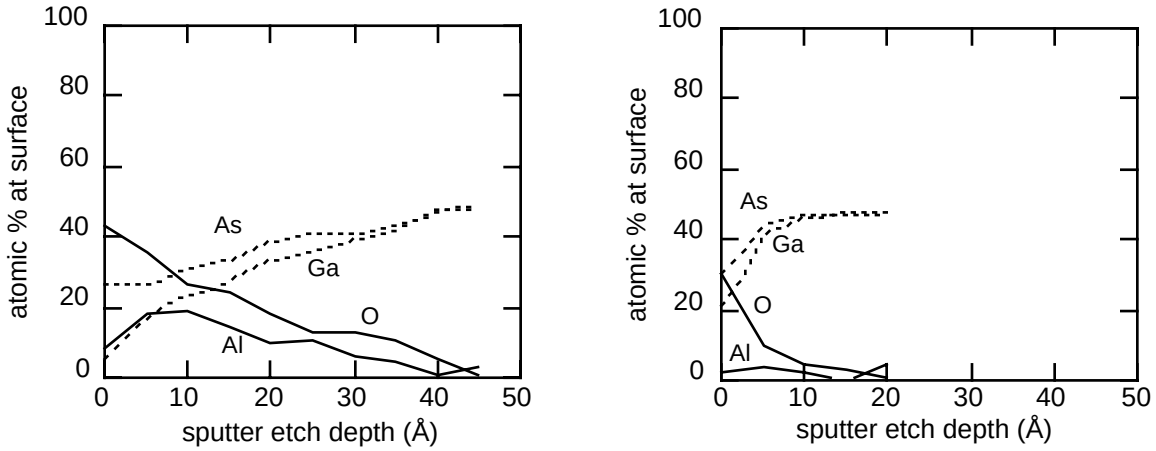

Figure 3.12: XPS depth profiles of GaAs surfaces after etch stop removal.
a) shows enhanced Al and O concentration on samples after AlGaAs removal in HCl.
b) shows the same surface with additional H_2O_2 and HCl dips and dramatically-reduced Al concentration.

The solubility of the compounds varies widely depending on the exact chemical composition. Most likely, exposure to H_2O_2 converts the scum layer from a less soluble composition to a different one which is more soluble in HCl. Such a compositional change is also consistent with our observation that when the surfaces with Al-O contamination films are dipped in H_2O_2, they no longer coalesce into particles upon subsequent exposure to air. The H_2O_2 dip may also oxidize a layer of GaAs underneath the Al-O layer so that subsequent oxide dissolution in the HCl assists removal of the aluminum-containing layer from the surface. Our observation of transformation from a uniform layer to small crystallites over a few days when the films are exposed to air is consistent with similar phase transformations previously observed in aluminum oxide and hydroxide gel compounds upon drying or hydration. Addition of the H_2O_2 and HCl dips eliminated the parti-

cle-generating behavior and resulted in our standard wet-etched-template process. Figure 3.13

hydroxide type	**composition**	**solubility limit in %**			
		HCl		NaOH	
		cold	hot	cold	hot
Orthohydroxide					
alpha	$Al(OH)_3$	0.1	0.1	0.4	0.1
beta	$4Al(OH)_3 - 3H_2O$	10	0.1	0.4	0.1
gamma	$Al(OH)_3$	37	1	insol.	0.1
Polyhydroxide					
Dihydroxide	$2Al(OH)_3 - H_2O$	insol.	5-10	insol.	4
A	$4Al(OH)_3 --3H_2O$ to $8Al(OH)_3 --7H_2O$	insol.	37	insol.	30
Metahydroxide	AlOOH	insol	insol	insol	--
table data taken from [50]					

Table 3.2: Table of solubilities for aluminum hydroxide compounds

illustrates the complete structure and the process used to pattern it. The layer thicknesses are representative; layer thicknesses varied over the course of template development. As improvements are made to the APD properties of the inverted GaAs films, the etch-stop layers, the inverted GaAs layer, and the resultant template corrugations can easily be reduced. In order to ensure a smooth GaAs surface for subsequent regrowth, we utilized etch stop layers both above and below the Ge layer. The lower etch stop provides a smooth surface for regrowth in the trenches and deals with the Ge etch-rate issue, while the upper etch stop and the GaAs cap above it provide sacrificial layers to keep photoresist and other contamination away from any surface which will be exposed to MBE regrowth. We found it essential that the top etch stop layer be located above the extent of the APDs in the inverted GaAs film, which is why the top GaAs layer is ~ 1000 Å thick. Otherwise, we observed a high density of etch pits across the surface where the etch presumably penetrated the etch-stop at the APD. The fact that we use a series of selective etches to pattern the template makes pitting a significant problem, since accidental exposure of the wrong layer at a pit makes possible dramatic unintended layer undercutting during subsequent etch steps.

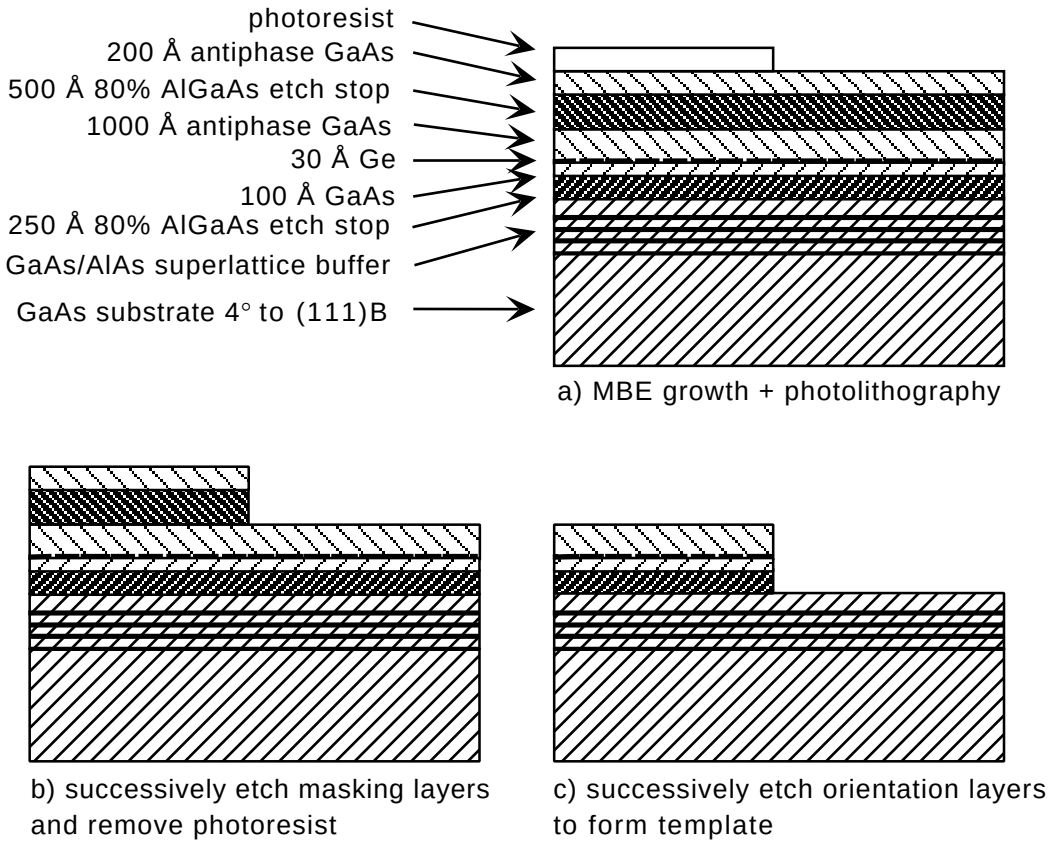

Figure 3.13: Final template fabrication process showing layer thicknesses.

3.6 MBE regrowth

Regrowth by MBE is usually less favored than regrowth by MOCVD, as MOCVD is less sensitive to surface contamination. It is well established that even very small concentrations of impurities like carbon can degrade the quality of MBE growth. However, the lack of any regularly available MOCVD capability motivated us to develop a workable MBE regrowth process. There is a very large body of literature on MBE regrowth and we followed procedures similar to those of others [51, 52]. Regrowth of orientation-patterned films, in contrast, is in its infancy, and we made a number of interesting observations. This section outlines the procedures we used for MBE regrowth of orientation-patterned films and presents our observations about domain boundary propagation, domain boundary disorder, and grating orientation effects.

3.6.1 Surface preparation

Typical regrowth surface preparation includes cleaning in a series of hot solvents (trichloroethane, acetone, isopropanol) to degrease and remove any organics from the surface, followed by a back-etch to remove oxides and contamination. Some groups follow the back-etch by intentional growth of a passivating oxide layer. Detailed discussion about the effects of various etching [53, 54] and passivation techniques [55, 56] is available. Our only addition to a standard regrowth preparation was the sacrificial layers on top of the template to protect the GaAs surface from photoresist and atmospheric contamination. Removal of these layers during patterning of the templates substituted for back-etching. We used a thin AlGaAs etch-stop layer comparable in thickness to the etch-stop layer underneath the Ge with a thin (100Å) GaAs cap on top to protect the AlGaAs from oxidation. By placing the photoresist on the top GaAs cap and etching through the first two (sacrificial) layers, we could then remove the photoresist and perform the solvent cleaning knowing that the entire surface would be subsequently etched before loading into the MBE. The sacrificial layers were then etched away in the same steps that cut through the Ge and removed the underlying AlGaAs etch stop. In this way, all layers exposed to photoresist or solvents are removed before regrowth. Unfortunately, the purity of the citric acid is not as high as acids such as HCl and it obviously contains carbon, so it may be the source of some impurities which create roughness and oval defects. We also determined that oxygen plasma ashing of the sample was necessary to obtain the highest quality regrown films, as regrown GaAs was rougher in the absence of the oxygen plasma exposure, probably due to carbon contamination. The oxygen plasma exposure was performed after removal of the photoresist and subsequent 3-solvent cleaning, but before the final etching through the Ge layer and underlying etch stop. After etching we performed a long DI water rinse, then blew the wafers dry and loaded directly into the UHV system. We did not use an oxide blow-off before initiating regrowth, as the resulting films appeared similar with and without the blow-off and we were concerned about potential surface roughening during extended exposure at high temperature. Regrowth always began with migration-enhanced epitaxy (MEE), which was intended to bury residual impurities on the surface and help smooth the surface during the initial stages of growth.

3.6.2 Orientation-patterned regrowth

For nonlinear optical devices, it is necessary that the domain structure be preserved up though the layers in which the frequency conversion will be performed to obtain the maximum nonlinear coefficient. This means that the optimal direction for APB propagation will be vertical

relative to the substrate plane. APBs have been observed to propagate along several different planes, including {100} and {110} [3]. The energy associated with the incorrect nearest neighbor bonding for APDs lying in each plane has been estimated by Petroff [57]. From his calculations, we see that the lowest energy plane for APDs is {110}. This makes some intuitive sense, since an APD lying in {110} will have an equal number of As-As and Ga-Ga bonds and the APB will be net charge neutral, unlike APBs lying in other planes. Because {110} is also the cleave plane in GaAs, it makes sense to orient our waveguide and bulk devices for propagation along <110>, so that we want the APBs to lie in the {110}. The detailed work of Li [26] found that APDs annihilated with their APBs in {110} for MOCVD growth in As-rich environments. For MBE growth conditions, we observed that the APBs propagate approximately in the desired {110} for all the growth conditions we have explored, with temperatures from 450° to 600° and AlGaAs compositions containing Al fractions from 0% to 70%. We have observed domains with aspect ratios up to 10:1 (5 μm tall: 0.5 μm wide) grown by MBE. It is clear from research into growth of thick, orientation-patterned GaAs films, discussed in chapter 5, that the APB plane is a function of the growth conditions and particularly the III/V ratio. All our orientation-patterned films were grown under large As overpressures of approximately 15:1 As/Ga beam equivalent pressures, as is typical for MBE. Thus, it appears fortunate that typical MBE growth conditions promote APB propagation in {110} and the vertical domain boundaries required for quasiphasematched frequency conversion devices.

While the domain boundaries themselves grow vertically, faceting at the domain boundaries is a significant problem. Figure 3.14 shows the top surface view of a regrown orientation-patterned GaAs film with clearly visible faceting at the boundaries compared to the surrounding regions of both orientations. This faceting affects ~ 1 μm on each side of the APB boundary. This faceting is perhaps not such a problem for widely-spaced boundaries, but for a grating with 2-μm-wide domains, the coherence length we used for harmonic generation with a 1.55 μm fundamental wavelength, the disruption affects the entire surface. Needless to say, such disruption is particularly bad for waveguide devices, where any inhomogeneties at the dielectric boundaries will cause scattering losses.

It is not clear yet whether this faceting results from the growth conditions, or whether it is generated by defects in the orientation template. Different crystal planes will be exposed at the two corners of the APB, and it is possible that the different growth rates on these planes or at the APB itself will produce a faceted surface. For example, inhibited Ga incorporation in the vicinity of the APD could lead to enhanced growth in nearby regions, thereby creating a groove. Once formed, such a groove might be subsequently enhanced by diffferences in growth rates on the now existing

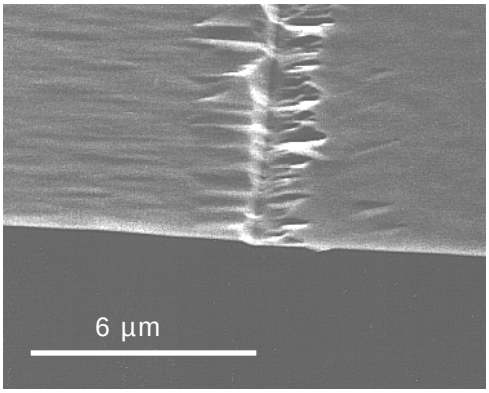

Figure 3.14: SEM micrograph showing disorder at the APB boundary.

facets. The work of Yoo, *et al.* doing MOCVD regrowth on wafer-bonded templates provides some indications that such faceting can be suppressed by changing the growth conditions. In their original devices, corrugations similar to what we observe are clearly visible at the waveguide core-cladding boundaries [1]. In subsequent devices, such corrugations were dramatically reduced through improved growth conditions, though the conditions themselves were not reported. Similar improvements are likely to be possible in these fiilms on all-epitaxial templates, whether using MBE or MOCVD regrowth.

Alternatively, the APB disorder may result from nonidealities on the template. In Figure 3.14, the in-plane surface misorientation direction points toward the viewer, so that the surface grows primarily by step-flow down the long dimension of the domains (toward the viewer). In the center of the relatively flat areas between domains, steps are free to flow smoothly down the surface, but near the boundary the faceted and uneven character of the surface prevents such uniform step flow. As a result, once some faceting or inhomogeneity appears, it might be further enhanced by disruption of step flow growth. We can then speculate about how the original roughening develops. Looking back at Figure 3.11, the template surface just prior to loading into the MBE has very rough edges at the stripe boundaries where the APBs will nucleate. On the right and left is the inverted GaAs material, slightly roughened due to the presence of APDs and associated non-uniformity in etching and etch stop layers. In the middle is the surface etched down to the substrate orientation, which is much smoother because it lies below any APD-related disorder. The boundary between orientations is jagged, varying laterally about ~ 0.25 µm along the stripe edge.

These edges have much greater roughness than the photoresist used to mask the etching, so some other process is responsible for the jagged appearance. The most likely candidate is again the presence of APDs at the GaAs-Ge interface. When we etch through the APD-containing layer, there will necesarily be some lateral etching at the stripe edges. Since the citric acid/hydrogen peroxide etchant used to remove the GaAs and Ge etches GaAs anisotropically, it will encounter randomly distributed regions of slow and rapid etch rate on the trench sidewalls depending on whether (111)A or (111)B is exposed. This could easily produce the jagged stripe sidewalls. Subsequent regrowth on a template with such jagged stripe sidewalls will encounter the previously descibed problems with step flow growth. Smooth step flow growth in the initial stages of growth near the template APB would be impossible, since this would require nucleation across the wandering APB. While it appears that the APB itself can minimize its energy and relax into a straight boundary during subsequent MBE growth, the morphological disorder left behind from the nucleation could well be enhanced by subsequent growth. The solution to this problem is again to reduce the size and density of the APDs at the interface and minimize the amount of non-uniform lateral etching into the sides of the inverted stripes. APD size reductions will allow thinner template layers and reduction of overall etch times and associated lateral etching. Clearly, elimination of the Al-O particles is also critical to improving these boundaries.

The final issue of orientation-patterned regrowth is the asymmetry between gratings oriented in the two orthogonal directions across the template surface. Figure 3.15 shows an SEM micrograph of a regrown wafer surface a with 2-μm domain period and the misorientation direction of the surface parallel to the k-vector of the orientation grating. One can clearly see that the surface contains relatively large steps every 2 μm. This case is in contrast with Figure 3.14, in which the grating k-vector was perpendicular to the surface misorientation direction and no step is visible beyond the simple groove at the APB. When the k-vector and surface misorientation directions are orthogonal, the domain can grow step flow down the length of a single domain. When the k-vector and misorientation direction are parallel, however, step-flow growth across the wafer will repeatedly encounter APBs, across which nucleation of new layers of inverted orientation will presumably be more difficult. This leads to a pileup of steps at the APBs and the stepped surface profile of Figure 3.15. We observed the same phenomenena in HVPE growth of thick GaAs films, with k-vectors parallel to misorientation directions producing films with larger surface roughness and a higher probability of domain overgrowth. Our results indicate that the grating k-vectors should be oriented perpendicular to the surface misorientation direction to achieve the smoothest possible layers. Moving to wafers with smaller misorientation angles would also

reduce this problem provided high quality epitaixal inversion was still possible. This topic is examined in more detail in chapter 5, where the relative orientations of the grating k-vectors and surface misorientation have larger impacts on film quality.

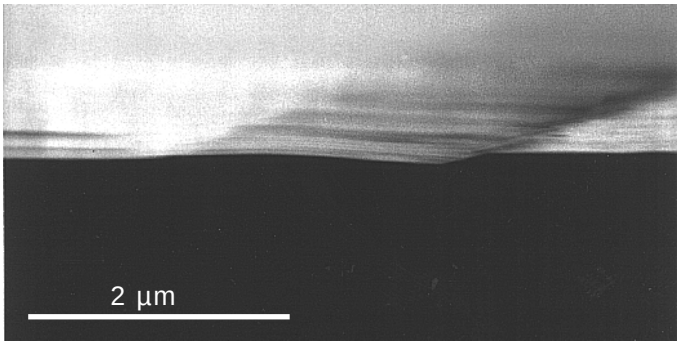

Figure 3.15: Cross-sectional SEM micrograph showing surface with large steps at the APDs.

3.7 Conclusion

We have investigated all-epitaxial fabrication of orientation templates using GaAs/Ge/GaAs heteroepitaxy and a variety of patterning techniques. This investigation produced successful orientation templates after some optimization of the growth conditions and the selective etching process. Additionally, we have explored ways of improving these templates further, including variations in nucleation temperature, substrate misorientation, and high temperature annealing, as well as possible lift-off technologies, with the ultimate goal of reducing the APD density and lowering template corrguation heights. While the results did not provide a conclusive recipe for optimal templates, they indicate that better quality templates are possible and offer some indications of how to achieve them.

References

1. S.J.B. Yoo, R. Bhat, C. Caneau, and M.A. Koza, "Quasi-phase-matched second-harmonic generation in AlGaAs waveguides with periodic domain inversion achieved by wafer-bonding," Appl. Phys. Lett. **66**, 3410-3412 (1995).

2. M.J. Angell, R.M. Emerson, J.L. Hoyt, J.F. Gibbons, L.A. Eyres, M.L. Bortz, and M.M. Fejer, "Growth of alternating <100>/<111>-oriented II-VI regions for quasi-phase-matched nonlinear optical devices on GaAs substrates," Appl. Phys. Lett. **64**, 3107-3109 (1993).

3. N.-H. Cho, B.C. De Cooman, C.B. Carter, R. Fletcher, and D.K. Wagner, "Antiphase boundaries in GaAs," Appl. Phys. Lett. **47**, 879-881 (1985).

4. P.K. Larsen and D.J. Chadi, "Surface structure of As-stabilized GaAs(001): 2 x 4, c(2 x 8), and domain structures," Phys. Rev. B **37**, 8282-8288 (1988).

5. K. Adomi, S. Strite, H. Morkoc, Y. Nakamura, and N. Otsuka, "Characterization of GaAs grown on Si epitaxial layers on GaAs substrates," J. Appl. Phys. **69**, 220-225 (1991).

6. K. Adomi, S. Strite, and H. Morkoc, "Antiphase-domain-free GaAs grown on pseudomorphic Si(100) surfaces by molecular beam epitaxy," Appl. Phys. Lett. **56**, 469-471 (1990).

7. S. Koh, T. Kondo, T. Ishiwada, C. Iwamoto, H. Ichinose, H. Yaguchi, T. Usami, Y. Shiraki, and R. Ito, "Sublattice reversal in GaAs/Si/GaAs (100) heterostructures by molecular beam epitaxy," Jpn. J. Appl. Phys. **37**, L1493-L1496 (1998).

8. S. Koh, T. Kondo, M. Ebihara, T. Ishiwada, H. Sawada, H. Ichinose, I. Shoji, and R. Ito, "GaAs/Ge/GaAs sublattice reversal epitaxy on GaAs (100) and (111) substrates for nonlinear optical devices," Jpn. J. Appl. Phys. **38**, L508-L511 (1999).

9. H. Kroemer, "Polar-on-nonpolar epitaxy: progress and new problems," Inst. Phys. Conf. Ser. **91**, 21-26 (1987).

10. M.A. Herman and H. Sitter, *Molecular Beam Epitaxy: Fundamentals and Current Status*, Springer Series in Materials Science, U. Gonser, A. Mooradian, K.A. Muller, M.B. Panish, and H. Sakaki eds. (Springer-Verlag, Heidelberg, 1989).

11. E.H.C. Parker, ed., *The Technology and Physics of Molecular Beam Epitaxy* (Plenum, New York, 1985).

12. W. Braun, *Applied RHEED: Reflection High-Energy Diffraction During Crystal Growth*, Springer Tracts in Modern Physics (Springer, New York, 1999).

13. X.-S. Wang, K.W. Self, and W.H. Weinberg, "Growth mode of Ge on GaAs(100)," J. Vac. Sci. Technol. A **12**, 1920-1923 (1994).

14. X.-S. Wang, K.W. Self, V. Bressler-Hill, R. Maboudian, and W.H. Weinberg, "Initial stages of Ge/GaAs(100) interface formation," Phys. Rev. B **49**, 4775-4779 (1994).

15. P.R. Pukite and P.I. Cohen, "Suppression of antiphase domains in the growth of GaAs on Ge(100) by molecular beam epitaxy," J. Cryst. Growth **81**, 214-220 (1987).

16. R.S. Bauer and J.C. Mikkelsen, "Surface processes controlling MBE heterojunction formation: GaAs(100)/Ge interfaces," J. Vac. Sci. Technol. **21**, 491-497 (1982).

17. B.J. Mrstik, "LEED and AES studies of the initial growth of Ge epilayers on GaAs(100)," Surface Sci. **124**, 253-266 (1983).

18. A.D. Katnani, P. Chiaradia, H.W. Sang, P. Zurcher, and R.S. Bauer, "Microscopic effects at GaAs/Ge(100) molecular-beam-epitaxy interfaces: Synchrotron-radiation photoemission study," Phys. Rev. B **31**, 2146-2156 (1985).

19. F. Stucki, G.J. Lapeyre, R.S. Bauer, P. Zurcher, and J.C. Mikkelsen, "Photoemission study of GeAs(201): A model for the As-stabilized Ge surface on GaAs/Ge heterojunctions," J. Vac. Sci. Technol. B **1**, 865-870 (1983).

20. J.H. Neave, P.K. Larsen, B.A. Joyce, J.P. Gowers, and J.F. van der Veen, "Some observations on Ge:GaAs(001) and GaAs:Ge(001) interfaces and films," J. Vac. Sci. Technol. B **1**, 668-674 (1983).

21. S.N.G. Chu, S. Nakahara, S.J. Pearton, T. Boone, and S.M. Vernon, "Antiphase domains in GaAs grown by metalorganic chemical vapor deposition on silicon-on-insulator," J. Appl. Phys. **64**, 2981-2989 (1988).

22. M. Akiyama, Y. Kawarada, and K. Kaminishi, "Growth of single domain GaAs layer on (100)-oriented Si substrate by MOCVD," Jpn. J. Appl. Phys. **23**, L843-L845 (1984).

23. R. Fisher, N.C. Chand, W.F. Kopp, H. Morkoc, L.P. Erickson, and R. Youngman, Appl. Phys. Lett. **47**, 397-399 (1985).

24. S.M. Ting, E.A. Fitzgerald, R.M. Sieg, and S.A. Ringel, "Range of Defect Morphologies on GaAs grown on offcut (001) Ge substrates," J. Electron. Mater. **27**, 451-461 (1998).

25. Y. Li, G. Salviati, M.M.G. Bongers, L. Lazzarini, L. Nasi, and L.J. Giling, "On the formation of antiphase domains in the system of GaAs on Ge," J. Cryst. Growth **163**, 195-202 (1996).

26. Y. Li and L.J. Giling, "A closer study on the self-annihilation of antiphase boundaries in GaAs epilayers," J. Cryst. Growth **163**, 203-211 (1996).

27. R.M. Sieg, S.A. Ringel, S.K. Ting, E.A. Fitzgerald, and R.N. Sacks, "Anti-phase domain-free growth of GaAs on offcut (001) Ge wafers by molecular beam epitaxy with suppressed Ge outdiffusion," Jour. Electron. Mater. **27**, 900-907 (1998).

28. S. Strite, D. Biswas, N.S. Kumar, M. Fradkin, and H. Morkoc, "Antiphase domain free growth of GaAs on Ge in GaAs/Ge/GaAs heterostructures," Appl. Phys. Lett. **56**, 244-246 (1990).

29. S. Strite, M.S. Unlu, G.-B. Gao, A. Agarwal, A. Rockett, and H. Morkoc, "GaAs/Ge/GaAs heterostructures by molecular beam epitaxy," J. Vac. Sci. Technol. B **8**, 1131-1140 (1990).

30. S. Strite, D. Biswas, K. Adomi, and H. Morkoc, "Study of sublattice orientation of GaAs on Ge," J. Appl. Phys. **67**, 1609-1612 (1990).

31. C.B. Ebert, "Quasi-phasematched waveguides for infrared nonlinear optics using GaAs/Ge/GaAs heteroepitaxy," Ph. D. dissertation (Stanford University, Stanford, 1998).

32. M.D. Pashley, K.W. Haberern, and J.M. Gaines, "MBE growth on vicinal GaAs(001) surfaces studied by scanning tunneling microscopy," Surface Sci. **267**, 153-160 (1992).

33. T. Shitara, J. Zhang, J.H. Neave, and B.A. Joyce, "Ga adatom incorporation kinetics at steps on vicinal GaAs (001) surfaces during growth of GaAs by molecular beam epitaxy," J. Appl. Phys. **71**, 4299-4304 (1992).

34. T. Shitara, D.D. Vvedensky, M.R. Wilby, J. Zhang, J.H. Neave, and B.A. Joyce, "Misorientation dependence of epitaixal growth on vicinal GaAs(001)," Phys. Rev. B **46**, 6825-6833 (1992).

35. A. Poudoulec, B. Guenais, C. D'Anterroches, M. Baudet, and A. Regreny, "Comparative study of interface structure in GaAs/AlAs superlattices grown by molecular beam epitaxy on (001) GaAs substrates misoriented towards $(111)_{Ga}$ or $(111)_{As}$ plane," Appl. Phys. Lett. **60**, 2406-2408 (1992).

36. N.C. Chand, S.N.G. Chu, and M. Geva, "Effects of substrate misorientation on incorporation of ambient oxygen and interfacial roughness in AlGaAs/GaAs heterostructures grown by molecular-beam epitaxy," Appl. Phys. Lett. **59**, 2874-2876 (1991).

37. D.C. Radulescu, G.W. Wicks, W.J. Schaff, A.R. Calawa, and L.F. Eastman, "Influence of substrate misorientation on defect and impurity incorporation in GaAs/AlGaAs heterostructures grown by molecular beam epitaxy," J. Appl. Phys. **63**, 5115-5120 (1988).

38. P.M. Petroff, R.C. Miller, A.C. Gossard, and W. Wiegmann, "Impurity trapping, interface structure, and luminescence of GaAs quantum wells grown by molecular beam epitaxy," Appl. Phys. Lett. **44**, 217-219 (1984).

39. C.B. Ebert, L.A. Eyres, M.M. Fejer, and J.S. Harris, "MBE growth of antiphase GaAs films using GaAs/Ge/GaAs heteroepitaxy," J. Cryst. Growth **201**, 187-193 (1999).

40. M. Kawabe, T. Ueda, and H. Takasugi, "Initial stage and domain structure of GaAs grown on Si(100) by molecular beam epitaxy," Jpn. J. Appl. Phys. **26**, L114-L116 (1987).

41. R.S. Becker, T. Klitsner, and J.S. Vickers, "Arsenic-terminated silicon and germanium surfaces by scanning tunneling microscopy," J. Microsc. **152**, 157-165 (1988).

42. R.D. Bringans, D.K. Biegelsen, and L.E. Swartz, "Atomic-step rearrangement on Si(100) by interaction with arsenic and the implication for GaAs-on-Si epitaxy," Phys. Rev. B **44**, 3054-3063 (1991).

43. J.J. LePore, "An improved technique for selective etching of GaAs and $Ga_{1-x}Al_xAs$," J. Appl. Phys. **51**, 6441-6442 (1981).

44. R.A. Logan and F.K. Reinhart, "Optical waveguides in GaAs-AlGaAs epitaxial layers," J. Appl. Phys. **44**, 4172-4176 (1973).

45. M. Tong, D.G. Ballegeer, A. Ketterson, E.J. Roan, K.Y. Cheng, and I. Adesida, "A comparative study of wet and dry selective etching processes for GaAs/AlGaAs/InGaAs Pseudomorphic MODFETs," Jour. Electron. Mater. **21**, 9-15 (1992).

46. H.G. Lee, M.S. Tse, K. Radhakrishnan, K. Prasad, J. Weng, S.F. Yoon, X. Zhou, H.S. Tan, S.K. Ting, and Y.C. Leong, "Selective wet etching of a GaAs/$Al_xGa_{1-x}As$ heterostructure with citric acid-hydrogen peroxide solutions for pseudomorphic GaAs/$Al_xGa_{1-x}As$/$In_yGa_{1-y}As$ heterojunction field effect transister [sic] fabrication," Mater. Sci. Eng. B **35**, 230-233 (1995).

47. C. Carter-Coman, R. Bicknell-Tassius, R.G. Benz, A.S. Brown, and N.M. Jokerst, "Analysis of GaAs substrate removal etching with citric acid:H_2O_2 and NH_4OH:H_2O_2 for application to compliant substrates," J. Electrochem. Soc. **144**, L29-L31 (1997).

48. K. Bacher and J.S. Harris, "A wet etching technique for accurate etching of GaAs/AlAs distributed Bragg reflectors," J. Electrochem. Soc. **142**, 2386-2388 (1995).

49. P. Moran, personal communication to J.S. Harris (1998).

50. Gmelins, *Aluminium Teil B: Die Verbindungen des Aluminiums*, Gmelins Handbuch der Anorganischen Chemie (Verlag Chemie, Berlin, 1934).

51. H.P. Meier, E. Van Gieson, W. Walter, C. Harder, M. Krahl, and D. Bimberg, "Molecular beam epitaxy of GaAs/AlGaAs quantum wells on channeled substrates," Appl. Phys. Lett. **54**, 433-435 (1989).

52. J.S. Smith, P.L. Derry, S. Margalit, and A. Yariv, "High quality molecular beam epitaxial growth on patterned GaAs substrates," Appl. Phys. Lett. **47**, (1985).

53. Z.H. Lu, C. Lagarde, E. Sacher, J.F. Currie, and A. Yelon, "A surface analytical study of GaAs(100) cleaning procedures," J. Vac. Sci. Technol. A **7**, 646-650 (1989).

54. J. Massies and J.P. Contour, "Substrate chemical etching prior to molecular-beam epitaxy: An x-ray photoelectron spectroscopy study of GaAs {001} surfaces etched by the H_2SO_4-H_2O_2-H_2O solution," J. Appl. Phys. **58**, 806-810 (1985).

55. J.P. Contour, J. Massies, H. Fronius, and K. Ploog, "An XPS study of the passivating oxide layer produced on GaAs (001) substrate by heating in air above 200°C," Jpn. J. Appl. Phys. **27**, L167-L169 (1988).

56. J. Saito, N. Kazuo, T. Ishikawa, and K. Kondo, "GaAs surface cleaning by thermal oxidation and sublimation in molecular-beam-epitaxy," J. Appl. Phys. **63**, 404-409 (1988).

57. P.M. Petroff, "Nucleation and growth of GaAs on Ge and the structure of antiphase boundaries," J. Vac. Sci. Technol. B **4**, 874-877 (1986).

CHAPTER 4: Fabrication and Characterization of Orientation-Patterned Waveguide Devices

The first nonlinear optical frequency conversion devices we investigated were orientation-patterned AlGaAs waveguide devices. These first devices were strip waveguides suitable for WDM frequency shifting, although they were characterized using simpler second harmonic generation experiments. After an introduction to nonlinear optical waveguide devices, this chapter will describe the design of the devices, their fabrication, and finally the evaluation of their optical properties, both linear and nonlinear. The chapter closes with a discussion of the present limitations on these devices and strategies for reducing the performance-limiting waveguide losses. Some of the results have been previously published in [1].

4.1 Introduction

Waveguide nonlinear-optical-frequency-conversion devices have advantages over bulk-focused devices for some applications. Since the propagation is determined by a dielectric structure rather than diffraction, one can achieve a tightly focused spot over long device lengths and achieve orders of magnitude higher gain. This higher gain makes possible high conversion efficiencies at much lower pump powers than with bulk-focused devices (~ 10^3 as derived in Chapter 2). In particular, nonlinear optical waveguides are well-suited to the powers obtainable from single-stripe diode lasers (~ 10s to 100s of mW). The suitability of diode lasers as pumps offers potentially compact, robust, and efficient nonlinear optical systems. One eventual dream for frequency conversion in semiconductors would be to integrate monolithically the pump diode/s and the nonlinear waveguides on the same substrate to achieve the ultimate in size, robustness and packaging simplicity.

However, accompanying these efficiency advantages come some limitations. The most obvious of these is the inherent limitation on power handling due to the small area of the waveguide endfacet and the finite optical damage threshold of the material. A more subtle complication is the necessarily multi-moded nature of nonlinear optical waveguides. Since any three-frequency interaction requires that two of the wavelengths involved differ by at least a factor of two, a typical dielectric waveguide will support multiple transverse modes at one or more of the relevant frequencies. So long as only wavelengths where the guide is single-moded are coupled into

the waveguide and the shorter wavelength modes are generated in the guides, as in SHG, this is not usually a significant problem. When shorter wavelength pump radiation must be coupled into the multi-moded waveguides, as is the case for some WDM mixer configurations and for all mid-IR generation devices, things become more complicated. Some fraction of the input power is coupled into modes other than the desired one, usually the lowest order transverse mode; this sensitive coupling reduces the effective pump power driving the frequency conversion process and makes the overall device extremely sensitive to mechanical stability, since slight misalignment of the input beam redistributes the input power among the waveguide modes.

By examining the present state of the art in waveguide nonlinear optical devices, one can gain an idea where semiconductor waveguides would be useful. The most widely and successfully used nonlinear optical waveguide fabrication process to date has been the annealed proton exchange (APE) in periodically-poled lithium niobate (PPLN) [2, 3]. The first major area of APE:PPLN application has been for optical communication system devices where the absolute power levels are constrained by propagation through optical fibers and where issues of cost necessitate diode laser pumps. Examples of such applications include wavelength shifting for conversion between WDM channels [4-6], mid-span spectral inversion for dispersion compensation [7], all-optical switching [8, 9], and time-division multiplexing [10]. For these applications, semiconductor devices could offer higher efficiency conversion at lower pump power levels and also offer straightforward polarization-independent wavelength conversion [11] simply by proper selection of pump polarization [12]. Another important APE:PPLN application where semiconductors would offer advantages is mid-IR generation for spectroscopic applications. Difference frequency generation of two diode lasers has been used to generate tunable mid-IR radiation for molecular spectroscopy [13, 14]. The much wider transparency range of semiconductors could allow such mid-IR generation out to the 12 μm wavelength range, much further than is possible with ferroelectric materials. For both of these applications, one of the critical breakthroughs for realizing efficient device performance was finding a solution to the previously mentioned higher-order mode coupling problem using tapered waveguides and integrated directional couplers [15].

In semiconductor waveguides, many techniques other than QPM have been used to phase-match frequency conversion and take advantage of semiconductors' favorable characteristics, though none has yet proven clearly superior. Boyd proposed modal phasematching for optical parametric oscillators in AlGaAs waveguides, though the devices have poor mode overlap and very high thresholds [16]. Van der Ziel and coworkers demonstrated form-birefringent phase-matching in AlGaAs superlattice waveguides, but the birefringence obtainable by this technique

($\Delta n_{TE-TM} = 0.033$) is not sufficient to phasematch most of the interesting device applications [17]. Oxidation of high Al-fraction AlGaAs in similar superlattices has recently provided an alternative technique which offers sufficient birefringence ($\Delta n_{TE-TM} = 0.6$) for phasematching useful interactions. Harmonic generation of a 1.5 μm laser was demonstrated in such an oxidized multilayer with ~8 dB/cm loss around 1.55 μm, but it was limited in efficiency by the 2000 dB/cm loss at the harmonic wavelength [18]. Mid-IR generation experiments were similarly limited by high losses of 217 dB/cm at the long wavelength [19, 20].

Spatial modulation of the magnitude of the nonlinear susceptibility in GaAs/AlGaAs superlattices after epitaxial crystal growth has been accomplished by two techniques. Impurity-free vacancy disordering has produced a 17% modulation in the magnitude of the nonlinear susceptibility with sufficient resolution to allow first-order quasiphasematching of 1.55 μm-pumped frequency doubling [21]. Losses reported for waveguides fabricated with this techniques are ~ 8 dB/cm [22]. Ion implantation techniques have also been used to modulate the nonlinear susceptibilities of asymmetric quantum well waveguides [23, 24], but measured susceptibilities in the near-IR wavelength range were small. Semiconductor surface emitting devices were also explored with phasematching obtained in the vertical direction by modulation of the waveguide core composition and/or resonant enhancement from a vertical cavity [25-27], but the non-collinear propagation inevitably limits the obtainable conversion efficiency.

By far the most impressive waveguide device results in semiconductors have been obtained by Yoo and coworkers at Bellcore. They demonstrated both SHG [28] and WDM channel shifting in AlGaAs waveguides [12] regrown on wafer-bonded template structures. Devices had waveguide losses of 5 dB/cm at 1550 nm and 25 dB/cm near 750 nm which limited the conversion efficiency of the wavelength conversion to -19 dB. Despite the high losses at short wavelength, such devices were used to demonstrate functions such as polarization filtering [29], spectral inversion, and multi-channel conversion. The waveguiding layers were grown using two MOVPE regrowth steps to produce fully buried heterostructures with more symmetric modes and better coupling efficiencies to fibers.

4.2 Waveguide Design

For initial demonstration of orientation-patterned waveguide devices, it was unclear which factors would limit the performance, though we anticipated that high waveguide losses were likely. As a result, we focused our design primarily on ease of fabrication and testing, leaving issues of noncriticality and mode coupling to fibers for a later time when the limitations would be better understood. Initial design choices were made according to fundamental considerations, after which more detailed numerical calculations were used to predict efficiencies and tuning behavior.

4.2.1 Considerations and constraints

One of the most important considerations for waveguide design is for the devices to be single-transverse-moded to simplify mode launching. At the same time, the mode needs to be sufficiently large to allow decent endfire coupling efficiency at reasonable numerical aperture. Ultimately, tapered waveguides like those used in APE PPLN devices would allow independent optimization of input coupling and QPM regions, but for the current devices both of these must be accomplished within the constraints of epitaxial growth and lithographic patterning of a single MBE-grown structure. For MBE, layer thickness is limited pratically to a maximum of between 5 μm and 10 μm depending on composition and grower disposition. For lithography, we observed that photoresist stripes with linewidths < 3 μm suffered much higher rates of delamination across typical wafers, an issue that could certainly be improved with optimized lithographic processes, but which constrained our waveguide widths in devices fabricated to date. Another constraint is that doing a second regrowth to form a completely buried heterostructure was not feasible, both because of the additional demand placed on the MBE system, and because MBE regrowth on Al-containing layers does not produce good quality layers. Aluminum oxides, which will form when AlGaAs layers are exposed to air, are not volatile at temperatures compatible with GaAs and MBE. Thus, the growing layers will nucleate on the amorphous oxide surface rather than a clean semiconductor surface, resulting in significantly degraded material quality. With access to MOVPE regrowth capability, this constraint would be relaxed and buried heterostructure devices could be fabricated as demonstrated by Yoo and coworkers [12]. As a result, we must fabricate the device with a single growth of a vertical waveguide structure followed by some etching step to provide lateral confinement. The vertical transverse mode properties will thus be dominated by the epitaxial structure, while the lateral transverse mode properties will be determined by a combination of the epitaxal structure and the etching profile.

The composition of the waveguide core was selected so that the device would be transparent at the harmonic wavelength around 775 nm for a fundamental 1.55 μm pump laser. The bandgap of $Al_xGa_{1-x}As$ as a function of Al fraction exhibits a sharp discontinuity at the transition between the direct and indirect transition, so that the increase in bandgap with Al composition is much lower above x = 0.45. We chose an $Al_{0.5}Ga_{0.5}As$ core to insure transparency and low residual bandtail absorption at the short wavelength. To determine the remaining parameters for the waveguide including core thickness, cladding thicknesses, and cladding composition, we can refer to the results derived in Section 2.2.3. Since we will be utilizing diffusion-limited wet chemical etching and we will need to etch through both the top cladding and the core to achieve our desired degree of lateral confinement, we choose a cladding composition of $Al_{0.6}Ga_{0.4}As$ so that the etching rates of the core and cladding will not differ too significantly. Choosing a smaller core-cladding composition difference is also possible, but would require core and cladding of correspondingly greater thickness. We see from Figure 2.4 that a normalized top cladding thickness equal to the core thickness ($w = 1$) will yield an approximately symmetric mode for normalized confinements $V \geq 1.7$.

The thickness of the lower cladding is also important to prevent excessive radiation losses from the waveguide core into the substrate, since the waveguide core layer will have a refractive index lower than the GaAs substrate. We can estimate the leakage into the substrate by the perturbation technique of Stultius and Streifer [30], approximating our 4-layer structure with $w = 1$ as a symmetric 3-layer waveguide on a high index substrate. They first calculate the modes of the structure in the limit that the lower cladding is infinitely thick, then perturb the eigenvalue equation with $\beta = \beta_\infty + \delta\beta$ to calculate a correction to the mode index when the lower cladding is finite. They derive an expression for the perturbed TE mode index .

$$\delta\beta = 2k_2^2 k_3 \left(\frac{k_4 - ik_3}{k_4 + ik_3}\right) \frac{\exp(-2k_3 t_3)}{\beta_\infty t_{eff}(k_2^2 + k_3^2)} \tag{4.1}$$

where

$$t_{eff} = t_2 + 1/k_1 + 1/k_3 \tag{4.2}$$

$$k_1 = (\beta^2 - k_0^2 n_1)^{1/2} \tag{4.3}$$

$$k_2 = (k_0^2 n_2 - \beta^2)^{1/2} \tag{4.4}$$

$$k_3 = (\beta^2 - k_0^2 n_3)^{1/2} \tag{4.5}$$

$$k_4 = (k_0^2 n_4 - \beta^2)^{1/2} \tag{4.6}$$

from which we can calculate the power attenuation in dB

$$\alpha(\text{dB/cm}) = 8.68\,\text{Im}(\delta\beta) = \left(\frac{34.7k_2^2k_3^2k_4}{k_4^2+k_3^2}\right)\frac{\exp(-2k_3t_3)}{\beta_\infty t_{eff}(k_2^2+k_3^2)} \tag{4.7}$$

Originally we used lower-cladding layers of 2-μm thickness, but found that this planar leakage model predicts 5 dB/cm losses. A cladding layer of 3 μm for these waveguide compositions and 1 μm core thickness will serve to reduce losses below the 0.21 dB/cm level. This calculation is only for TE modes, but for our SHG devices the TM mode will be at the harmonic wavelength and the radiation losses will be negligible. The total thickness of the waveguiding layers is thus 5 μm, to which we will add a 1 μm thick superlattice buffer layer before the waveguiding layers to smooth the surface before waveguide growth. Our vertical waveguide structure is thus like that of Yoo and coworkers [28], allowing direct comparison with their results.

Lateral confinement will be achieved by etching through a planar waveguide structure. Sufficient confinement to make the waveguide single-moded in the horizontal direction can be obtained over a range of rib widths, since we can trade rib width vs. etch depth to yield the same normalized confinement. However, one important consideration pushes us in the direction of deep etching. Practically, coupling of the fundamental radiation into the ridge waveguide is greatly simplified by insuring that the surrounding planar waveguide is cut-off at the fundamental wavelength. Input coupling and observation of the desired mode is much easier when not complicated by a background of radiation transmitted through the planar waveguide. The desirabiliy of this criterion was determined empirically by working with waveguides of both designs. This is particularly true when one examines devices with short lengths where the planar mode radiation has little distance over which to diffract in the plane.

Unfortunately, the case where lateral cladding is formed by etching a planar waveguide to or beyond cutoff is the most complicated case to model. For very weak confinement, one can use the effective index approximation [31] (and references therein) to estimate the degree of lateral confinement, but as the planar region approaches cutoff this method diverges from the actual solution [32]. Below the planar mode cutoff, no mode index exists to use in the approximation. To allow comparision between theory and experiment we therefore modeled this device using a numerical 2-D finite-difference-equation (FDE) analysis described in the next section.

4.2.2 Finite difference equation (FDE) modelling

To predict the efficiency and tuning behavior of this waveguide device we utilized a numerical FDE solution for quasi-TE and quasi-TM modes implemented using Matlab. The method follows that described by Stern [33, 34]; our implementation was compared to the test cases contained in these papers to an accuracy in the modal index of approximately $2*10^{-4}$. Since the waveguide mode is always symmetric or antisymmetric about the center of the waveguide, we modeled only half of the mode to minimize computational time. Figure 4.1 shows the FDE-solved, lowest-order fundamental and harmonic modes of the previously described waveguide structure with vertical sidewalls. Using this model, we can obtain the results shown in Figure 4.2

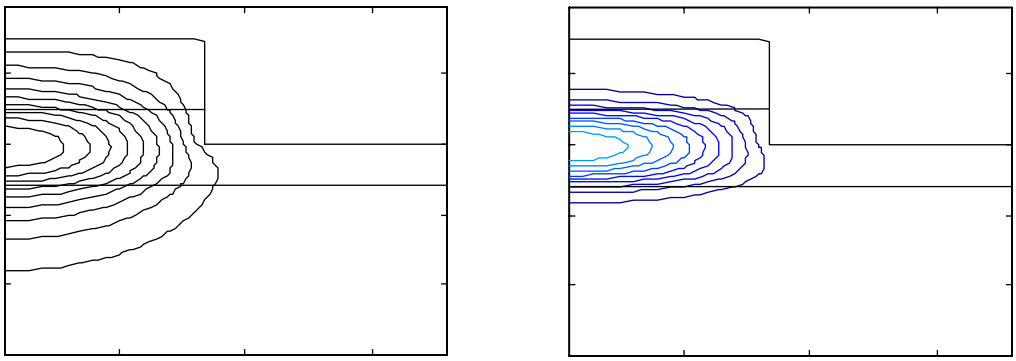

Figure 4.1: Fundamental and harmonic modes of FDE-modelled ridge waveguides consisting of air/$Al_{0.6}Ga_{0.4}As$/$Al_{0.5}Ga_{0.5}As$ /$Al_{0.6}Ga_{0.4}As$ layers with 1-µm-thick core and top cladding layers and 5 µm stripe width. Contours are in increments of 10% of the peak field amplitude.

for the harmonic generation effective area as a function of etch depth and waveguide width for the vertical structure described above. The transition to double-moded behavior is shown by the approximately horizontal dotted line. This line is approximate, as the FDE solver loses accuracy as the waveguide mode approaches cutoff and the mode extends much further from the core region. The vertical dashed line shows the etch depth required for achieving cutoff of the planar mode. By placing stripes of widths ranging from 3-8 µm on the waveguide mask, we can ensure that at least some of the devices will be single-moded. This allows for some variability in the etching process, as well as some in the undercut which will occur for isotropic etches and which will reduce the waveguide width an amount comparable to the etch depth on each side. The actual

range of apparent single mode behavior will be wider than that marked by the dashed line, since higher order modes near cutoff will have high modal fields at dielectric boundaries and therefore suffer from very high waveguide losses.

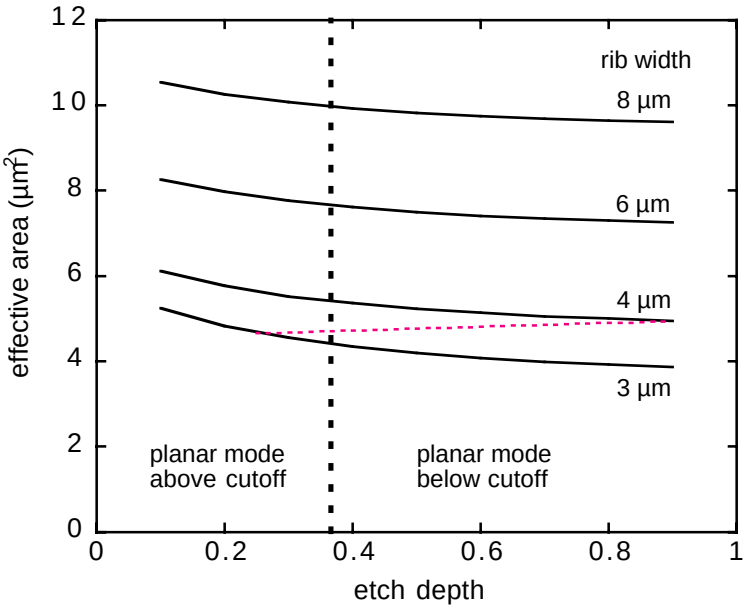

Figure 4.2: Effective area of etched-rib waveguides for second harmonic generation using a 1.55 μm fundamental as a function of rib width and etch depth. Vertical line shows cutoff for planar waveguide mode. Approximately horizontal line shows limit of single-mode transverse behavior

4.3 Orientation-patterned waveguide fabrication

Our orientation-patterned waveguide devices were fabricated using a combination of MBE to grow a planar waveguiding layer and wet chemical etching to provide lateral confinement. There is a large literature on semiconductor waveguide fabrication of which some examples are available in [35] and [36].

4.3.1 MBE regrowth of waveguide structures

The channel waveguide devices were fabricated by the epitaxial inversion/patterned regrowth technique described in Chapter 3. After regrowth preparation, waveguiding layers were grown by MBE. A GaAs/AlGaAs superlattice buffer identical to that used in Chapter 3 was grown on the template before growth of the waveguiding layers. This buffer is useful because regions of the surface clearly have B-type steps exposed and we expect roughening similar to that observed

on the much cleaner $[1\bar{1}0]$-misoriented wafers. In the absence of those buffers, the regrown film regions are much rougher. The exact composition of the superlattice layers is most likely not significant, so that the compositions can be adapted to be compatible with the growth rates set for the cladding and core layers. After the superlattice buffer, the waveguide cladding was grown, followed by the core and top cladding layers. Typical regrowth rates were 0.5 μm/hour with two different Ga sources, with one flux set for the core composition and the other flux set for the difference between the core and cladding compositions.

A cleaved and stain-etched SEM cross section of the waveguide structure grown by the above process is shown in Figure 4.3. After cleaving, the sample was stain-etched in a potassium ferricyanide solution to reveal the domain boundaries and composition differences. The exposed surface is misoriented towards the in-plane $(1\bar{1}0)$, so that the grating k-vector lies along [110] and we have no macroscopic "stair-stepping" of the surface. The APBs can be clearly seen running almost perfectly vertically up through the GaAs, superlattice, and AlGaAs layers. In the region of vertical propagation, the APBs lie in or approximately in {110}. This vertical propagation was observed under all growth conditions examined, with compositions from GaAs to 70% AlGaAs, growth temperatures from 450 °C to 600 °C, and varying growth rates. Some authors have hypothesized [37] that APB propagation plane is a function of the vapor concentrations above the substrate. If there were some dependence of the APB propagation direction on the environment, we would not have observed any effect since we were always regrowing under As-rich (~ 15:1 As:Ga ratio) conditions, consistent with the propagation of the APBs observed by Li [38] for MOCVD growth under As-rich conditions.

Observing the character of the APBs as a function of height, we see some variation shortly after initiation of regrowth, followed by vertical propagation up though many microns of material. The variations at the beginning are likely due to the APD equilibration mechanism discussed in the previous chapter. After some distance during which the originally rough and wandering APB minimizes its energy and surface area, it can then propagate in the nominal {110} plane through the rest of the film. On regrown samples with only GaAs rather than AlGaAs, the APBs were much more difficult to discern in the SEM after stain-etching the same length of time. This may be evidence of compositional variations in the vicinity of the APB. In MBE, Al and Ga have significantly different average surface diffusion lengths before incorporation. The Al length has been measured to be approximately 10 nm, while Ga has a diffusion length closer to 1 μm under typical MBE conditions [39]. If there is a difference in incorporation probability for Al and Ga at the APB

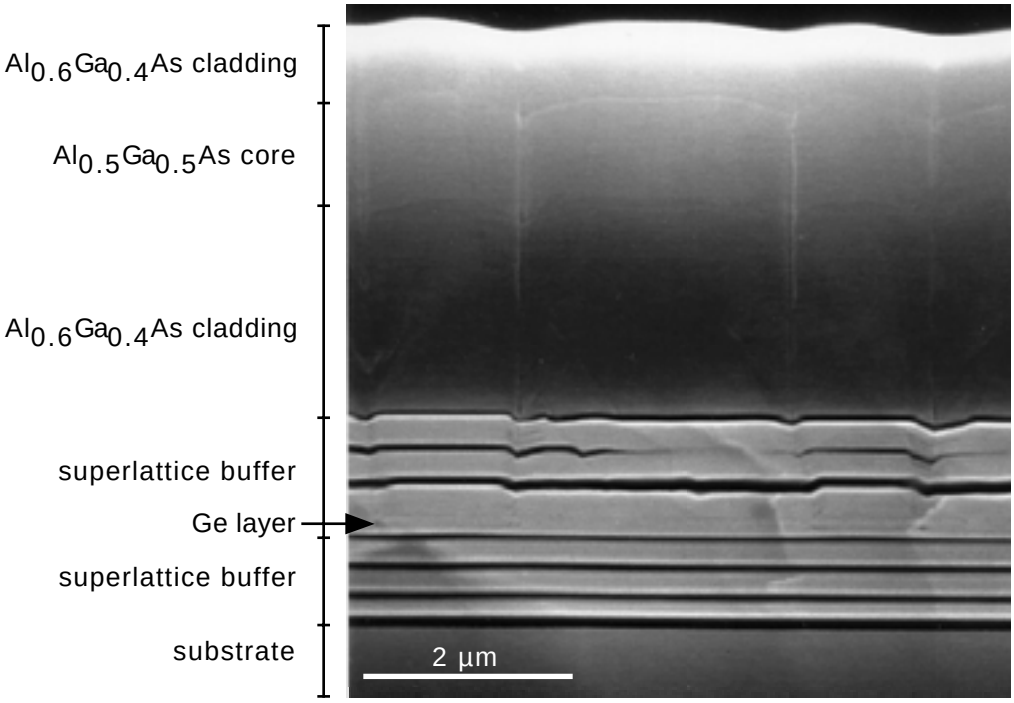

Figure 4.3: Stain-etched cross-section of orientation-patterned AlGAs waveguide structure exhibiting vertical antiphase domain boundaries and grooves at the APBs.

itself, or on the facets which develop adjacent to it, it would not be surprising to find enhancement of the Al concentration near the APB, since the Ga atoms could diffuse elsewhere while the Al atoms would incorporate near where where they adsorbed. From the micrograph, it is likely that growth is inhibited in the vicinity of the APD, since we see a groove at each boundary and this groove is enhanced with increasing film thickness. However this growth may be complicated by the lateral spreading effects of regrowth containing morphological inhomogeneities, as was proposed at the end of Chapter 3. Similar grooves surrounding APDs are observed in plain GaAs growth, as was visible back in Figure 3.14. The faceted grooves here are too small to allow unambigous determination of the possible atomic planes on which the grooves manifest themselves.

Some corrugation of the boundaries between the core and cladding is observed, particularly at the APBs. Occasional inhomogeneties are also visible in the smoother regions between APBs. Note that the corrugations and defects are all much larger than any corrugation of the original template, so that they have developed at points during the MBE growth process. The original corrugation was 1000 Å. This again argues for the estabilshment of surface and APB corrugations in the initial phases of epitaxial growth, followed by their preservation during subsequent growth.

All the issues of step-flow-caused disruption near that APB region certainly apply to this situation, as well as do the issues of the Al-O contamination, since all waveguide devices tested to date were fabricated before the the Al-scum layer had been eliminated. As a result, the disruption at the APBs visible in Figure 4.3 probably have contributions from multiple sources.

4.3.2 Diffusion-limited wet chemical etching

Etching to produce lateral confinement for a ridge waveguide with low-losses ($\leq$ 1 dB/cm) has been performed by a variety techniques including wet chemical etching [40-44], reactive ion etching [45-47], and ion milling[32, 48]. For our applications etching is complicated by the presence of different crystal planes on the exposed waveguide sidewall. Many wet etchants exhibit strongly anisotropic etch rates into {111}A and {111}B facets. While this was an advantage for determining the presence of APDs, such behavior would be an unmitigated disaster in etching orientation-patterned waveguides. The alternating orientation would leave alternating {111}A and {111}B faceted waveguide sidewalls along the length of the waveguide. Use of the most common rate-limited etchants would produce a large corrugation on the waveguide sidewalls and very high waveguide losses.

To eliminate these complications, we utilized diffusion-limited wet chemical etching, which etches nominally isotropically. Many individual steps make up the overall chemical etching reaction for GaAs, including diffusion of reactants to the surface, the oxidation reaction, dissolution of the reaction products, and their diffusion away from the surface [49]. A particular etchant can be limited by any one or more than one of these processes. For example, the citric acid/peroxide etchant used for the template fabricated and described in chapter 3 is limited by the solubility of the Al-oxide reaction products [50]. In contrast, the diffusion-limited etch is, as the name suggests, limited by diffusion of oxidant (H_2O_2) to the GaAs surface. The isotropic nature of this etch is due to the fact that once the proper boundary layers have been established, the local etch rate is limited by the diffusion independent of the intrinsic etch rate on the particular facets exposed. Globally, this diffusion length is a function of the etchant concentration, while locally the etch rate can be enhanced or inhibited by morphological features such as photoresist stripes [51, 52]. No peroxide is consumed on top of the photoresist stripe, so that excess peroxide is present along the edges of the stripe leading to deeper etching adjacent to the stripe than in the center of a large etched region. However, the etch profile should be uniform along the length of an otherwise uni-

form stripe regardless of GaAs orientation, which is what we require for preventing etch-induced corrugation. Adachi gives an overview of many different GaAs etches, their rates, and anisotropy [53].

To produce lateral confinement, photoresist stripes were first patterned using Shipley 1813 photoresist and a standard exposure/development process. The (80:4:1) $HCl:H_2O_2:H_2O$ system is one of a few chemical etches for GaAs/AlGaAs known to be diffusion-limited [49]. We found this etchant was unstable and that it decayed with time, so it had to be re-mixed before each use and the delay time between mixing and etching tightly controlled. Using the etch 1 minute after mixing, we found an etch rate of ~ 0.4 μm/ min for $Al_{0.5}Ga_{0.5}As$, but the rate exhibited some yet unexplained variability between etching attempts. In the face of this variability, the use of multiple width photoresist stripes insured that some of the devices would be single-moded. Also, we found that the etch decays much more quickly in glass containers, probably due to some catalytic effect on the peroxide from the glass, so only plastic beakers could be used. Figure 4.4 shows an SEM micrograph of a cleaved facet from an AlGaAs channel waveguide fabricated using such etching. The sidewall profile is smooth, indicating that the diffusion-limited etching has not caused any additional roughing or corrugation on the sidewalls. Residual corrugation from the top surface is visible, however, both on the top and sidewalls of the waveguide, though if anything it is attenuated by the diffusion-limited etch. The diffusion-limited etch was sometimes used to smooth the surface slightly before lithography in order to reduce the surface roughness and corrugation and improve the lithography uniformity. The etch exhibits a somewhat higher etch rate near the edges of the the etched piece where 2-dimensional rather than 1-dimensional diffusion governs the peroxide concentration. As a result, large (quarter-wafer) pieces were subjected to waveguide etching, then smaller pieces were cleaved from the center of the quarter wafers to make uniform waveguide samples for optical testing.

4.3.3 Additional fabrication

After waveguide etching, endfacets were formed by cleaving after thinning. Wafer pieces were first mounted onto a polishing block with wax and the substrates were lapped until $<$ 150 um total thickness remained. The fragile sample pieces were demounted, cleaned, and finally cleaved by rolling a curved scalpel blade onto the sample edge while it sat on top of a stack of filter paper. The goal of the filter paper was to provide a flexible surface which would support the sample and allow it to bow slightly under pressure from the scalpel blade, resulting in relatively uniform strain across the sample. The sample was placed on the filter paper with the waveguide side down. That

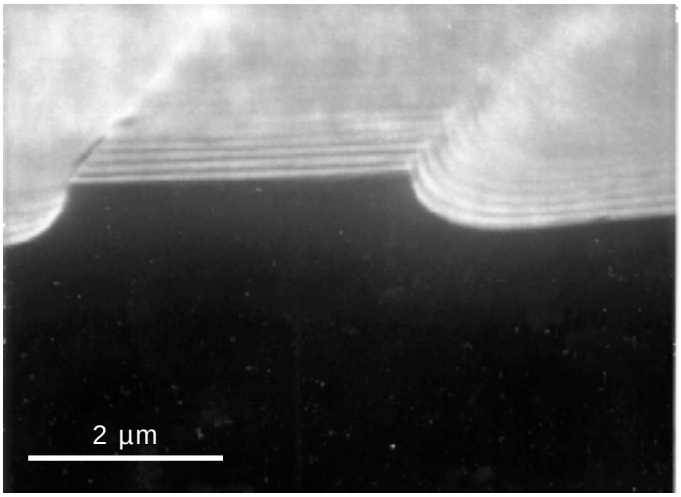

Figure 4.4: Cleaved facet of orientation-patterned AlGaAs waveguide structure.

way, when the scalpel blade rolled onto the edge and bends the wafer, the surface containing the waveguides is under tension rather than compression, while the wafer backside is under compression. We found that significantly better end-factets resulted near the surface under tension, which makes intuitive sense. The waveguide end-facets of optical samples were examined under an optical microscope to insure good cleaving before any optical testing was performed. The cleaving yield varied with sample length. For 5 mm long samples yields were near 100%. Devices with waveguide lengths down to ~1 mm were produced by this process, though the cleaving yields dropped to around 50%.

4.4 Optical characterization

Both linear and nonlinear optical properties of these waveguide devices were characterized at fundamental and harmonic wavelengths. Linear optical losses were measured by two different techniques. At 1550 nm, the waveguides supported a single-mode, so we could utilize the Fabry-Perot technique, while at 780 nm we tried a variation on the standard cut-back technique. Second harmonic generation measurements were also performed, allowing comparison of the efficiencies with our predictions given the large waveguide losses observed.

4.4.1 Optical attenuation

A single-mode waveguide with input and output facets acts as a Fabry-Perot cavity and will exhibit interference fringes similar to an etalon in the transmitted beam when the input wavelength is varied [54]. Defining a fringe contrast *K* in terms of the maxima and minima of the fringe pattern,

$$K = \frac{I_{max} - I_{min}}{I_{max} + I_{min}} \tag{4.8}$$

we can express *K* as

$$K = \frac{2\tilde{R}}{1 + \tilde{R}^2}, \tag{4.9}$$

where

$$\tilde{R} = R\exp(-\alpha L). \tag{4.10}$$

The waveguide losses can then be expressed as

$$\alpha = \frac{4.34}{L}(\ln(R) - \ln(\tilde{R})) \tag{4.11}$$

where α is the attenuation of the waveguide, *L* is the sample length, and *R* is the modal reflectivity at the facet. It is optimal to extract the reflectivity by measuring devices with varying waveguide lengths and fitting a line to the attenuation vs. length data; however, our limted sample number and the large variability between adjacent waveguides made this technique ineffective. For a weakly confining waveguide, the endfacet reflectivity can be approximated as

$$R = \left(\frac{n_{eff} - 1}{n_{eff} + 1}\right)^2 \tag{4.12}$$

where n_{eff} is the modal effective index. If we assume this value for the reflectivity while the actual facet reflectivity is lower due to facet imperfections or other factors, equation 4.11 indicates that we will determine an upper bound on the propagation losses. To estimate the reflectivity, we used the effective index calculated by the FDE solver described in Section 4.2.2 in equation 4.12.

Radiation from a 1.55 μm tunable external cavity diode laser was amplified in a erbium-doped fiber amplifier and coupled into the waveguide using a microscope objective. A similar microscope objective was used to image the mode from the output facet onto a Ge photodiode. Results for a simple GaAs/$Al_{0.1}Ga_{0.9}As$ waveguide of 4 mm length having a 1-μm-thick core but no top cladding are presented in Figure 4.5. This sample had no orientation patterning or MBE regrowth and was intended to determine what loss values we could achieve using simple MBE

growth and wet chemical etching. A pattern with waveguide widths of 3 μm, 4 μm, 6 μm and 8 μm was repeated across the surface of the sample; the attenuation results from two full patterns are shown in figure 4.5. The lowest-loss guides cluster in the neighborhood of 3-4 dB/cm and appear across the whole sample. The large variation in attenuation losses between individual waveguides likely results from discrete defects along the waveguides such as MBE oval defects or lithography imperfections. Additionally, we were unable to observe light through several of the waveguides, perhaps due to large lithography defects. The residual loss mechanism in these guides was not determined, but is likely to be scattering from residual sidewall roughness due to lithography and etching. In these plain MBE-grown waveguides, we achieved losses comparable to those observed by Yoo, *et al.* in waveguides without orientation-patterning [55]. The fabrication processes are thus capable of achieving reasonable waveguide losses in the absence of orientation-patterning.

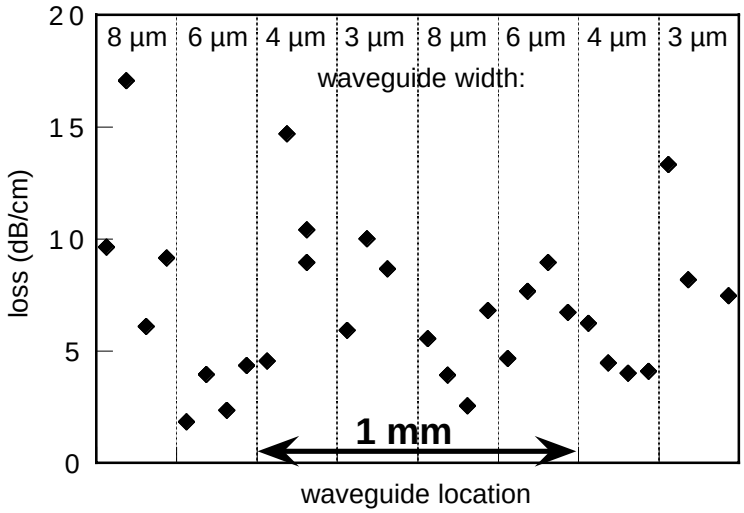

Figure 4.5: Attenuation losses across sample for waveguides of varying ridge width.

Applying this same Fabry-Perot technique to the orientation-patterned GaAs devices, we measured fringe contrasts between 0.087 and 0.124 for 1.8 mm long waveguides containing varying length orientation gratings (from 0.2 mm to 1.6 mm). These fringe contrasts translate into losses of between 35 dB/cm and 60 dB/cm for that sample length. Many of the waveguides on this sample were not observed to transmit any radiation. We observe that the attenuation was not correlated with the fraction of the waveguide contaning orientation patterning, or at least the waveguide-to-waveguide variation is too large to allow clear comparison between samples of

varying orientation grating length. Since similar losses were observed when the orientation-patterned fraction varied between 11% and 89% across the sample, we conclude that the losses in the waveguides are dominated by some overall fabrication issue, not problems particular to orientation patterning. Observation of the waveguide endfacets under an optical microscope shows apparently high quality facets, so the facets were not responsible for the degredation in the fringe contrast. In contrast, miscroscope observation of the waveguide top surface revealed many pinhole defects which could account for the high waveguide losses. These pinholes are likely caused in large part by the coalesced Al-O particles which must have been present on the wafer surface before regrowth, since all waveguide devices were fabricated before solving the Al-O problem.

At the harmonic wavelength the waveguide is not single-moded and we attempted to measure the attenuation by measuring transmission through waveguides having varying grating lengths. Since we had only one surviving sample which phasematched in the range of our tunable laser system, our intent was to correlate the losses in waveguides of equal width with the fraction of the sample occupied by orientation gratings. Unfortunately, the huge waveguide-to-waveguide loss variations again swamped any correlation between orientation grating length and attenuation. Simple ratioing of power transmitted through a particular waveguide to power incident on that same waveguide yielded attenuations ranging from -40 dB to -60 dB. The input coupling efficiency was not determined, but it is likely to have been somewhere between 5% and 50% (-13 dB and -3 dB), indicating that we have very high losses also at the harmonic wavelength. The lack of correlation with the length of the orientation patterned region again appears to reflect a fabrication problem not directly related to the orientation patterning.

4.4.2 Harmonic generation

The nonlinear characterization of these waveguide devices was performed by harmonic generation. An experimental diagram of the harmonic generation apparatus is shown in Figure 4.6. Tunable radiation from an external cavity diode laser was amplified in an erbium-doped fiber amplifier, then endfire coupled into the waveguide using a microscope objective. The output fundamental and harmonic were focused onto Ge and Si diodes, respectively, using another microscope objective. Filters were placed before the Si photodiode to absorb any residual pump wavelength radiation. The fundamental was chopped before the waveguide and the output signal detected using a lockin amplifier. The input fundamental was polarized TE and the output harmonic was polarized TM, as required by the symmetry of d_{14}.

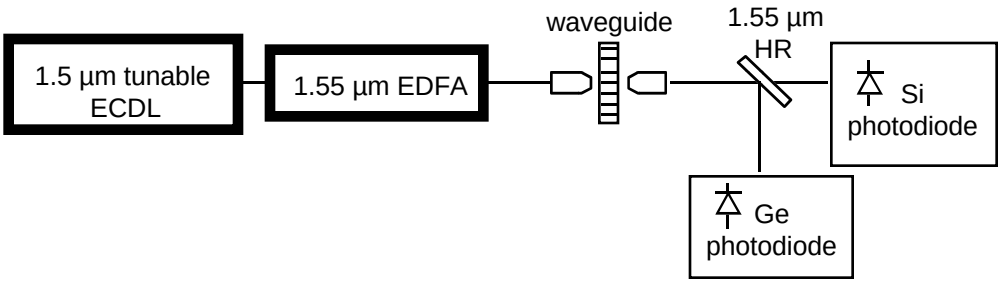

Figure 4.6: Diagram of waveguide harmonic generation experiment.

The data in Figure 4.7 show the measured harmonic outout power as a function of the fundamental wavelength for the best device and the theoretical tuning behavior. The FWHM tuning bandwidth agrees with the predicted 1.7 nm for this waveguide with a 0.84 mm long orientation-patterned grating, since the device is sufficiently short to prevent the high attenuation from broadening significantly the phasematching bandwidth. The effective area for this 5-µm-wide device was calculated to be 7.2 μm^2 using the FDE model described in Se ction 4.2.2. We scale d_{14} using Miller's rule to 76 pm/V for $Al_{0.5}Ga_{0.5}As$ and doubling 1.55 µm. This value is consistent with the measurements of Ohashi, *et al.* [56]. From equation 2.36 we predict a lossless theoretical normalized internal efficiency of 13 $W^{-1}cm^{-2}$. For the 0.84 mm long orientation-patterned-grating section present on this waveguide we tested, this corresponds to a conversion efficiency of 9.2 %/W. We can add corrections as discussed in Section 2.1.5 for the case of significant attenuation at both the fundamental and harmonic wavelengths. Assuming a 40 dB/cm attenuation affecting the fundamental and harmonic wavelengths uniformly along the length of the waveguide, we obtain a reduced theoretical internal efficiency of 2.1 %/W. This agrees to within a factor of 2 with the peak efficiency in Figure 4.7. Of course, the actual effect of the high attenutation is difficult to determine, since the attenuation will be distributed unevenly along the waveguide due to discrete defects such as pinholes. The shoulder on the tuning curve at shorter wavelength occurs because we were operating near the shoulder of the EDFA gain peak. As the single pass gain decreases, the amplified spontaneous emission near the EDFA gain peak (which is closer to the tuning curve peak) increases relative to the signal at the seed wavelength set by the ECDL, so that the power normalization becomes less accurate.

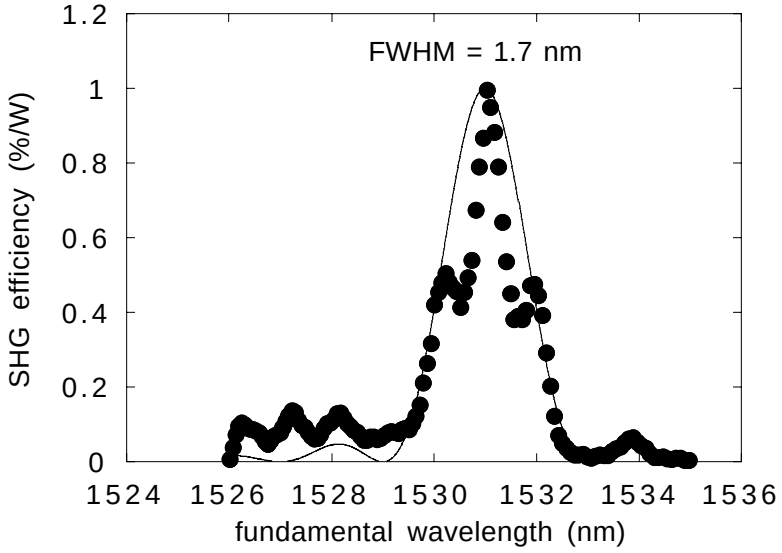

Figure 4.7: Harmonic generation efficiency as a function of fundamental wavelength for orientation-patterned AlGaAs waveguide.

4.5 Discussion

With an internal conversion efficiency of 1 %/W this device is clearly not yet suitable for applications such as WDM conversion or DFG of mid-IR radiation. The usual route of increasing device length to improve efficiency is not possible here, as we are already into a region of significant saturation with length due to the high losses. The very high waveguide losses are clearly disappointing and significant reductions in waveguide loss will be required before orientation-patterned waveguide devices will be practical. The most favorable strategy to improving this device is to improve the quality of the regrown waveguiding layers as outlined in the latter part of Chapter 3. The major candidates for the large waveguide losses observed include incomplete Al-O removal and growth inhomogeneities of various kinds.

All waveguide devices were fabricated before we had solved the problems with Al-O contamination. Since the fabrication process for all the waveguide samples involved removing AlGaAs etch-stop layers above and below the Ge using citric acid/hydrogen peroxide, the templates presumably had Al-contamination exposed all over the top surface. The exact behavior of the Al-O under vacuum drying in the MBE is unclear, but the samples vacuum-dried upon intro-

duction into the XPS system exhibited the same particle coalesence formation as was observed in air. Whether the Al-O was distributed across the surface or concentrated into particles, MBE regrowth would be affected. The regrown waveguide samples exhibited an uneven and streaky haziness even to the naked eye after regrowth. Under microsopic examination a high density of pits and depressions were observed in clear regions across the GaAs surface, presumably correlated with the Al-O particle density before regrowth. Since the entire surface was covered with an etch-stop before the final HCl-H_2O dip, we would expect the surface particle density to be on average roughly constant. This uniform roughness is a likely origin of the very high waveguide losses observed in all waveguides across the sample, both orientation-patterned and single-orientation. With improvements in processing to eliminate this AlO_x contamination, we expect that the next generation of waveguides will have significantly lower waveguide losses.

Beyond those general issues of the material quality, the presence of various longitudinal corrugations along the waveguide will affect the waveguide losses, though those effects were masked in these samples by the presence of additional fabrication-related losses. However, assuming improved regrowth quality, at some point the corrugations will dominate the waveguide losses. From the micrograph in Figure 4.3 we can see that the clearly visible corrugation of the core/cladding boundaries is less like a pure step-function and more like grooves which develop at the boundaries. Whether this effect is due primarily to particle nucleation on the template stripe edges, roughness at the template stripe boundaries, or inherently faceted growth at APBs under these growth conditions is not yet clear. Undoubtedly these corrugations can be reduced and any reductions in corrugation amplitude should result in lower losses once the corrugations become the dominant loss source. Another approach to dealing with corrugation is to utilize waveguide designs which are less sensitive to corrugations of particular spatial frequencies, since the major contributions will exist at well-defined spatial frequencies which are various harmonics of the domain period.

Comparing our waveguide loss results to previous work, we can see the ultimate results of Yoo, *et al.* [29] are much better than ours at 1.55 um, where they measured 5 dB/cm in comparison to our ~40 dB/cm. At 780 nm, the devices are more similar with the Bellcore results having 25 dB/cm, while we see > 40 dB/cm. Yoo, *et al.* attributed waveguide losses to corrugation. Their first generation devices had losses comparable to or greater than the initial results demonstrated here (60dB/cm at the harmonic wavelength) and those losses dropped by orders of magnitude with improved regrowth quality. We anticipate similar improvements here with by solving the issues

complicating regrowth. Such improvements are necessary, as useful nonlinear optical waveguide devices will require losses down into the few dB/cm range at all wavelengths of interest.

4.6 Conclusion

We have designed AlGaAs waveguides for WDM frequency conversion, fabricated them using orientation templates and MBE regrowth, and characterized their linear and nonlinear optical properties. We find high waveguide losses of $\geq$ 40 dB/cm at both pump and signal wavelengths of 1.55 μm and 775 nm. These losses severely limit the device efficiencies to around 1 %/W by limiting the practical waveguide device length. The origins of these losses have been examined and methods of reducing them suggested. Future research will need to focus on reduction of the waveguide losses to the point that the devices are useful for the applications envisioned.

References

1. L.A. Eyres, C.B. Ebert, P.J. Tourreau, J.S. Harris, and M.M. Fejer, "Demonstration of second harmonic generation in all-epitaxially-grown orientation-patterned AlGaAs waveguides," *Advanced Solid-State Lasers*, Topics in Optics and Photonics Vol. 26, M.M. Fejer, H. Injeyan, and U. Keller, eds. (Optical Society of America, Washington, DC, 1999) pp. 689-693.
2. M.L. Bortz and M.M. Fejer, "Annealed proton-exchanged $LiNbO_3$ waveguides," Opt. Lett. **16**, 1844-1846 (1991).
3. M.L. Bortz, "Quasi-phasematched optical frequency conversion in lithium niobate waveguides," Ph. D. dissertation (Stanford University, Stanford, CA, 1994).
4. M.H. Chou, J. Hauden, M.A. Arbore, and M.M. Fejer, "1.5-μm-band wavelength conversion based on difference-frequency generation in $LiNbO_3$ waveguides," Opt. Lett. **23**, 1004-1006 (1998).
5. M.H. Chou, I. Brener, M.M. Fejer, E.E. Chaban, and S.B. Christman, "1.5-μm-band wavelength conversion based on cascaded second-order nonlinear susceptibility in $LiNbO_3$," IEEE Photonics Technol. Lett. **11**, (1999).
6. K. Gallo and G. Assanto, "Analysis of lithium niobate all-optical wavelength shifters for the third spectral window," J. Opt. Soc Am. B **16**, 741-753 (1999).
7. M.H. Chou, I. Brener, G. Lenz, R. Scotti, E.E. Chaban, J. Shmulovich, D. Philen, S. Kosinski, K.R. Parameswaran, and M.M. Fejer, "Efficient wide-band and tunable midspan spectral inverter using cascaded nonlinearities in $LiNbO_3$ waveguides," IEEE Photonics Technol. Lett. **12**, 82-84 (2000).
8. R. Schiek, L. Friedrich, H. Fang, G.I. Stegeman, K.R. Parameswaran, M.H. Chou, and M.M. Fejer, "Nonlinear directional coupler in periodically poled lithium niobate," Opt. Lett. **24**, 1617-1619 (1999).
9. K.R. Parameswaran, M. Fujimura, M.H. Chou, and M.M. Fejer, "Low-power all-optical gate based on sum frequency mixing in APE waveguides in PPLN," IEEE Photonics Technol. Lett. **12**, 654-656 (2000).
10. S. Kawanishi, M.H. Chou, K. Fujiura, M.M. Fejer, and T. Morioka, "All-optical modulation and time-division-multiplexing of 100 Gbit/s signal using quasi-phase matched mixing in $LiNbO_3$ waveguides," Electron. Lett. **36**, 1568-1569 (2000).
11. I. Brener, M.H. Chou, E.E. Chaban, K.R. Parameswaran, M.M. Fejer, S. Kosinski, and D.L. Pruitt, "Polarization-insensitive wavelength converter based on cascaded nonlinearities in $LiNbO_3$ waveguides," Electron. Lett. **36**, 66-67 (2000).

12. S.J.B. Yoo, C. Caneau, R. Bhat, M.A. Koza, A. Rajhel, and N. Antoniades, "Wavelength conversion by difference frequency generation in AlGaAs waveguides with periodic domain inversion achieved by wafer bonding," Appl. Phys. Lett. **68**, 2609-2611 (1996).

13. K.P. Petrov, A.P. Roth, T.L. Patterson, T.P.S. Thoms, L. Huang, A.T. Ryan, and D.J. Bamford, "Efficient difference-frequency mixing of diode lasers in lithium niobate channel waveguides," Appl. Phys. B **70**, 777-782 (2000).

14. K.P. Petrov, A.T. Ryan, T.L. Patterson, L. Huang, S.J. Field, and D.J. Bamford, "Spectroscopic detection of methane by use of guided-wave diode-pumped difference-frequency generation," Opt. Lett. **23**, 1052-1054 (1998).

15. M.H. Chou, M.A. Arbore, and M.M. Fejer, "Adiabatically tapered periodic segmentation of channel waveguides for mode-size transformation and fundamental mode excitation," Opt. Lett. **21**, 794-796 (1996).

16. J.T. Boyd, "Theory of parametric oscillation phase matched in GaAs thin-film waveguides," IEEE J. Quantum Electron. **8**, 788-796 (1972).

17. J.P. Van der Ziel and M. Illegems, "Second harmonic generation in a thin AlAs-GaAs multilayer structure with wave propagation in the plane of the layers," Appl. Phys. Lett. **29**, 200-202 (1976).

18. A. Fiore, S. Janz, L. Delobel, P. Van der Meer, P. Bravetti, V. Berger, E. Rosencher, and J. Nagle, "Second-harmonic generation at lambda = 1.6 μm in AlGaAs/Al_2O_3 waveguides using birefringence phase matching," Appl. Phys. Lett. **72**, 2942-2944 (1998).

19. A. Fiore, V. Berger, E. Rosencher, P. Bravetti, N. Laurent, and J. Nagle, "Phase-matched mid-infrared difference frequency generation in GaAs-based waveguides," Appl. Phys. Lett. **71**, 3622-3624 (1997).

20. P. Bravetti, A. Fiore, V. Berger, E. Rosencher, J. Nagle, and O. Gauthier-Lafaye, "5.2-5.6-μm source tunable by frequency conversion in a GaAs-based waveguide," Opt. Lett. **23**, 331 (1998).

21. M.W. Street, N.D. Whitbread, D.C. Hitchings, J.M. Arnold, J.H. Marsh, J.S. Aitchison, G.T. Kennedy, and W. Sibbett, "Quantum-well intermixing for the control of second-order nonlinear effects in AlGaAs multiple-quantum-well waveguides," Opt. Lett. **22**, 1600-1602 (1997).

22. M.W. Street, N.D. Whitbread, C.J. Hamilton, B. Vogele, C.R. Stanley, D.C. Hutchings, J.H. Marsh, J.S. Aitchison, G.T. Kennedy, and W. Sibbett, "Modification of the second-order optical nonlinearities in AlGaAs asymmetric multiple quantum well waveguides by quantum well intermixing," Appl. Phys. Lett. **70**, 2804-2806 (1997).

23. S. Janz, M. Buchanan, P. Van der Meer, Z.R. Wasilewski, D.X. Xu, P. Piva, I.V. Matchell, U.G. Akano, and A. Fiore, "Patterning the second-order optical nonlinearity of asymmetric quantum wells by ion implantation enhanced intermixing," Appl. Phys. Lett. **72**, 3097-3099 (1998).

24. J.P. Bouchard, M. Tetu, S. Janz, D.X. Xu, Z.R. Wasilewski, P. Piva, U.G. Akano, and I.V. Mitchell, "Quasi-phase matched second-harmonic generation in an $Al_xGa_{1-x}As$ asymmetric quantum-well waveguide using ion-implantation-enhanced intermixing," Appl. Phys. Lett. **77**, 4247-4249 (2000).

25. R. Lodenkamper, M.L. Bortz, M.M. Fejer, K. Bacher, and J.S. Harris, "Surface-emitting second-harmonic generation in a semiconductor vertical resonator," Opt. Lett. **18**, 1798-1800 (1993).

26. A. Fiore, Y. Beaulieu, S. Janz, J.P. McCaffrey, Z.R. Wasilewski, and D.X. Xu, "Quasiphase matched surface emitting second harmonic generation in periodically reversed asymmetric GaAs/AlGaAs quantum well waveguide," Appl. Phys. Lett. **70**, 2655-2657 (1997).

27. S. Janz, Y. Beaulieu, A. Fiore, P. Bravetti, V. Berger, E. Rosencher, and J. Nagle, "Surface-emitted second-harmonic generation from a quasi-phasematched waveguide in an $Al_xGa_{1-x}As/Al_2O_3$ microcavity," Optics Express **2**, (1998).

28. S.J.B. Yoo, R. Bhat, C. Caneau, and M.A. Koza, "Quasi-phase-matched second-harmonic generation in AlGaAs waveguides with periodic domain inversion achieved by wafer-bonding," Appl. Phys. Lett. **66**, 3410-3412 (1995).

29. S.J.B. Yoo, M.A. Koza, R. Bhat, and C. Caneau, "Bidirectionally pumped difference-frequency generation in AlGaAs waveguides: polarization-independent, multichannel wavlength conversion with input signal filtering capabilities," *Conference on Lasers and Electro-Optics*, OSA Trends in Optics and Photonics Vol. 6 (Optical Society America, Washington, DC, 1998) pp. 107-108.

30. J. Stultius and Z. Streifer, "Silicon nitride films on silicon for optical waveguides," Appl. Opt. **16**, 3218-3222 (1977).

31. J. Buus, "The effective index method and its application to semiconductor lasers," IEEE J. Quantum Electron. **QE-18**, 1083-1089 (1982).

32. M.W. Austin, "Theoretical and experimental investigation of GaAs/GaAlAs and n/n+ GaAs Rib waveguides," J. Lightwave Tech. **2**, 688-693 (1984).

33. M.S. Stern, "Semivectorial polarised finite difference method for optical waveguides with arbitrary index profiles," IEE Proc. J **135**, 56-63 (1988).

34. M.S. Stern, "Rayleigh quotient solution of semivectorial field problems for optical waveguides with arbitrary index profiles," IEE Proc. J **138**, 185-190 (1991).

35. H.P. Zappe, *Introduction to Semiconductor Integrated Optics* (Artech House, Boston, 1995).

36. R.G. Hunsperger, *Integrated optics: Theory and Technology* (Springer-Verlag, New York, 1995).

37. V.I. Vdovin, M.G. Mil'vidskii, and T.G. Yugova, "Antiphase boundaries in GaAs layers on Si and Ge," J. Cryst. Growth **132**, 477-482 (1993).

38. Y. Li and L.J. Giling, "A closer study on the self-annihilation of antiphase boundaries in GaAs epilayers," J. Cryst. Growth **163**, 203-211 (1996).

39. T. Yamada and Y. Horikoshi, "Comparison of GaAs facet formation on patterned substrate during molecular beam epitaxy and migration enhanced epitaxy," Jpn. J. Appl. Phys. **33**, L1027-L1030 (1994).

40. E. Kapon and R. Bhat, "Low-loss single-mode GaAs/AlGaAs optical waveguides grown by organometallic vapor phase epitaxy," Appl. Phys. Lett. **50**, 1628-1630 (1987).

41. M. Seto, R.J. Deri, A. Yi-Yan, E. Colas, W.J. Tomlinson, R. Bhat, and A. Shahar, "Fabrication of submillimeter-radius optical waveguide bends with anisotropic and isotropic wet chemical etchants," J. Lightwave Tech. **8**, 264-270 (1990).

42. M.K. Hibbs-Brenner and C.T. Sullivan, "Low-loss AlGaAs optical rectangular waveguides at 830 nm," Appl. Phys. Lett. **56**, 1529-1531 (1990).

43. R.J. Deri, E. Kapon, J.P. Harbison, M. Seto, C.P. Yun, and L.T. Florez, "Low-loss GaAs/AlGaAs waveguide phase modulator using a W-shaped index profile," Appl. Phys. Lett. **53**, 1803-1805 (1988).

44. R.J. Deri, E. Kapon, R. Bhat, M. Seto, and K. Kash, "Low-loss multiple quantum well GaInAs/InP optical waveguides," Appl. Phys. Lett. **54**, 1737-1739 (1989).

45. P. Buchmann, H. Kaufmann, H. Melchior, and G. Guekos, "Reactive ion etched GaAs optical waveguide modulators with low loss and high speed," Electron. Lett. **20**, 295-297 (1984).

46. P.W. McIlroy, P.M. Rodgers, J.S. Singh, P.C. Spurdens, and I.D. Henning, "Low-loss single-mode InP/InGaAsP waveguides grown by MOVPE," Electron. Lett. **23**, 701-703 (1987).

47. R.J. Deri, E. Kapon, and L.M. Schiavone, "Scattering in low-loss GaAs/AlGaAs rib waveguides," Appl. Phys. Lett. **51**, 789-790 (1987).

48. H. Inoue, K. Hiruma, K. Ishida, T. Asai, and H. Matsumura, "Low loss GaAs optical waveguides," J. Lightwave Tech. **LT-3**, 1270-1275 (1985).

49. D.W. Shaw, "Localized GaAs etching with acidic hydrogen peroxide solutions," J. Electrochem. Soc. **128**, 874-880 (1981).

50. M. Tong, D.G. Ballegeer, A. Ketterson, E.J. Roan, K.Y. Cheng, and I. Adesida, "A comparative study of wet and dry selective etching processes for GaAs/AlGaAs/InGaAs Pseudomorphic MODFETs," Jour. Electron. Mater. **21**, 9-15 (1992).

51. H.K. Kuiken, J.J. Kelly, and P.H.L. Notten, "Etching profiles at resist edges I: Mathematical models for diffusion-controlled cases," J. Electrochem. Soc. **133**, 1217-1226 (1986).

52. P.H.L. Notten, J.J. Kelly, and H.K. Kuiken, "Etching profiles at resist edges II: Experimental confirmation of models using GaAs," J. Electrochem. Soc. **133**, 1226-1232 (1986).

53. S. Adachi and K. Oe, "Chemical etching characteristics of (001) GaAs," J. Electrochem. Soc. **130**, 2427-2435 (1983).

54. R. Regener and W. Sohler, "Loss in low-finesse Ti:$LiNbO_3$ optical waveguide resonators," Appl. Phys. B **36**, 143-147 (1985).

55. S.J.B. Yoo, personal communication to L.A. Eyres (1998).

56. M. Ohashi, T. Kondo, R. Ito, S. Fukatsu, Y. Shiraki, K. Kumata, and S.S. Kano, "Determination of quadratic nonlinear optical coefficient of $Al_xGa_{1-x}As$ system by the method of reflected second harmonics," J. Appl. Phys. **74**, 596-601 (1993).

CHAPTER 5: Growth and Characterization of Thick Orientation-Patterned GaAs

5.1 Introduction

Given the excellent vertical domain propagation observed in thin film orientation-patterned semiconductor growth, a natural question arises: can such domain quality be preserved through thicker layers (> 0.5 mm) suitable for bulk-focused frequency conversion? There are significant advantages to having larger apertures for some frequency conversion applications, particularly those requiring high power-handling capability. Also, since the radiation is not confined by a dielectric structure, the attenuation losses and device performance are less dependent on complicated issues of expitaxial growth morphology, making possible faster device development.

This chapter will review our investigations into the growth and characterization of thick orientation-patterned GaAs films. It opens with a discussion of the growth techniques suitable for producing such thick films, focusing particularly the HVPE process. Next, we investigate issues of orientation-patterned film quality and characteristic defects in thick GaAs films, demonstrating that thick orientation-patterned GaAs films with high domain quality are achievable. After discussing the linear optical properties of these films, the chapter will close with the results of harmonic generation experiments that confirm the utility of these films for frequency conversion applications. Many of the results have been published in [1, 2].

5.2 Thick GaAs growth processes

Several techniques are capable of growing significantly thicker GaAs apertures than the ~10 um available in MBE, including MOCVD [3], chloride vapor phase epitaxy (Cl-VPE) [4-6], hydride vapor phase epitaxy (HVPE) [7, 8] and close-spaced vapor transport (CSVT)[9, 10]. The primary issues in extension to much thicker films are the much larger source volumes necessary and the elimination of UHV vacuum requirements and associated overhead on source reloading. We investigated thick orientation-patterned GaAs growth by two of these techniques, Cl-VPE and HVPE. In both cases, the thick growth experiments were performed in collaboration with groups already operating the requisite reactors. To date, only HPVE has demonstrated films with high quality domains, for reasons which are explored in more detail below.

The Cl-VPE and HPVE growth techniques utilize the same chemical reaction to deposit GaAs, though the precursors differ in the two cases. The basic reaction is

$$H_2 + As_x + GaCl \leftrightarrow GaAs + HCl$$

where H_2 serves as the carrier gas. The HVPE process utilizes AsH_3, HCl and metallic Ga as the source materials. The HCl reacts with the metallic Ga in one furnace region to generate GaCl. The GaCl and separately injected AsH_3 enter the second furnace zone where the AsH_3 decomposes into H_2 and some mixture of As_2 and As_4 and the above reaction can proceed to deposit GaAs. An additional HCl inlet with the AsH_3 allows more control over the vapor composition above the substrate.

The Cl-VPE technique relies on the same reaction, but utilizes $AsCl_3$ as a precursor rather than AsH_3. The $AsCl_3$ reacts directly with the metallic Ga to produce As_2 and GaCl, which is simpler because fewer sources are required and because $AsCl_3$ is a liquid at room temperature rather than a gas, making it potentially less dangerous. The drawback is that Cl-VPE offers less control over the vapor composition above the substrates. Most importantly, the As/Ga ratio can't be controlled directly by precursor injection, since the both the As and Ga concentrations are tied directly to the $AsCl_3$ input concentration.

These growth processes and the basic reactions have been investigated in great detail by many authors at both atmospheric pressure and low-pressure for both HVPE and CL-VPE techniques [4-7, 11, 12]. Growth rates in excess of 50 μm/hour are possible, though higher growth rates often produce surfaces with lower homogeneity and higher defect densities. Background doping levels below $10^{15}/cm^3$ have been demonstrated using HPVE [11]. The growth regime can be mass-transport or kinetically limited, depending on the substrate temperature and gas composition above the substrate [7]. Typical substrate temperatures range between 700 °C and 800 °C.

Growth rates for GaAs have been investigated as a function of gas composition, temperature, pressure, and crystal orientation by many investigators. Even in the early work of Shaw [7], one can see that the growth rates vary dramatically as a function of crystal orientation. For example, the growth rate on $\{111\}_{As}$ and $\{111\}_{Ga}$ can differ by more than an order of magnitude under the same growth conditions, between 80 μm/hr and 8 μm/hr. The most relevant results for our application have been recently published by Gil-Lafon, *et al.* [8] as part of a collaboration which includes Bruno Gerard, who performed the HVPE growths described in later sections of this chap-

ter. They investigated the relative growth rates on varying GaAs facets as a function of HVPE growth conditions and resulting morphology of growth on patterned surfaces. With the control over vapor composition afforded by HVPE, they could parametrize the growth rates as a function of substrate temperature, vapor supersaturation, and III/V ratio. They find that for a III/V ratio of 4.5, low supersaturation, and a growth temperature of 730 °C, the growth rate hierarchy is $\{111\}_{Ga} >> \{001\} > \{110\} \geq \{110\}_{As}$. When the III/V ratio is increased or widely decreased, the growth rate of $\{111\}_{As}$ drops significantly below that of {110}. Under high supersaturation conditions, the growth rate of the $\{111\}_{Ga}$ drops below that of {001}. When growth is performed on masked regions or etched stripes, the facets exhibited after HPVE growth naturally correspond to those having the lowest growth rates under those particular growth conditions. Knowledge of these relative growth rates will allow interpretation of the surface morphologies observed on orientation-patterned GaAs films.

5.2.1 Growth by CL-VPE

Our first attempts at thick GaAs growth were performed by CL-VPE in collaboration with researchers at the Ioffe Institute in St. Petersburg, Russia. Orientation templates with 5-μm MBE-GaAs grown on top were used to seed growth of 100-μm-thick GaAs films. Typical results of this growth experiment are shown in Figure 5.1. The antiphase boundary has been marked to make it easily visible. The other vertical lines are artifacts of the sample cleaving. One can see that the APB wanders in direction locally between {111} and {100}, with vertical propagation observed only for short sections. This propagation naturally results in domains closing over in a thickness comparable the original domain width. While the exact antiphase domain boundary cross-section differed from boundary to boundary across the sample, all such boundaries exhibited the same general propagation direction and domain annihilation behavior. The local changes in APB growth direction are likely due to localized changes in growth parameters such as vapor concentration. Having only a single Cl-VPE thick GaAs growth run made it impossible to determine the factors controlling domain behavior. In addition, because the collaborators who performed the thick growth were unwilling disclose details about the growth process, we are unable to speculate about whether changes in the growth parameters would make a significant difference in the APB propagation behavior.

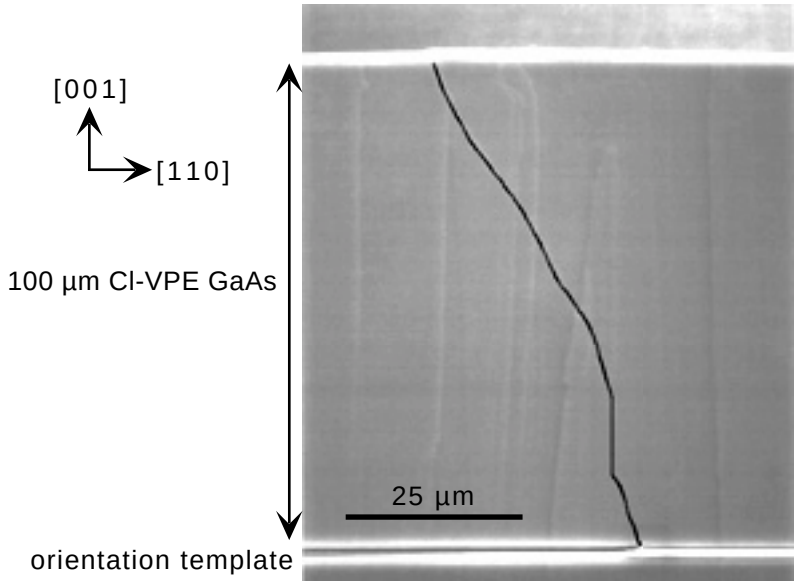

Figure 5.1: Cross-section of 100-µm-thick GaAs film grown by Cl-VPE. APB is marked in black for easier identification.

5.2.2 Growth by HVPE

After the Cl-VPE processs yielded poor domain quality, our focus turned to HPVE growth, which allows more independent control over the vapor composition above the substrate. Templates similar to those for Cl-VPE were fabricated with 5 µm MBE GaAs on top to seed the thick growth. For these experiments, the thickness of the GaAs layer on top of the Ge was increased to 1000 Å in order to eliminate pinholes produced during the template-producing etching steps. The template was cleaved into samples of approximately 1 cm^2 before HVPE growth in order to allow for multiple sample runs from the limited wafer area available. Among the few samples which had thick GaAs grown on top included 212-µm periods, 27-µm periods and several other periods with the grating k-vectors aligned both parallel and perpendicular to the in-plane misorientation direction.

The thick GaAs was grown at Thales (Thomson-CSF) Central Research Laboratory in Orsay, France by Bruno Gerard. The hot-wall horizontal quartz reactor has two inlets, one for the flow of $HCl+H_2$ over the 7N Ga source and the other bypassing the source for AsH_3, main H_2 carrier flow and additional HCl. The total flow was about 1 standard liter/minute. The temperatures of the Ga source and of the GaAs substrate were kept at 850°C and 750°C, respectively, and the growth was carried out at atmospheric pressure. The vertical growth rate was about 10 µm/hr. By

varying the composition of the vapor phase (III/V ratio between 3 to 10), different lateral facets of the stripes growing on (100) or (-100) surfaces can be obtained, either of {011} or {111}types [8, 13, 14]. For the present application, only growth conditions consistent with {011}facets were utilized in order to preserve the width of the anti-phase domains.

After thick GaAs growth, the samples were polished to expose the domain structure. Stain-etching of the domains was attempted using the same potassium ferricyanide etch as was discussed in Chapter 4, but no signs of the domain boundaries were visible in the optical or electron microscopes. Instead we employed a selective etch which attacked different GaAs crystal orientations at different rates, leading to a corrugation visible by optical microscopy on the previously polished surface. An etch of (1:1:100) $NH_3OH:H_2O_2:H_2O$ worked well for this purpose, after which the samples were characterized using an optical microscope.

Figure 5.2 shows a top view and cross-section of a 200-μm-thick GaAs film grown by HVPE with a 27-μm domain period. In comparison to the previous results using Cl-VPE, the domain boundaries here grow almost exclusively vertically, so that the domain duty cycle is preserved up through the thick GaAs. No change in duty cycle was measureable for the majority of domains. This behavior is clearly optimal for use in quasi-phasematched frequency conversion applications, since the desired susceptibility modulation will be preserved in the region of the optical radiation. In this case, the grating k-vector was aligned perpendicular to the surface misorientation direction, so that the APBs lie approximately in {110}. This behavior is consistent with the observations of Li, [15], who observed stable propagation of APBs in {110} for MOCVD growth under As-rich growth conditions. All samples with domain periods from 212 μm to 27 μm with the same grating orientation show similarly vertical boundaries. The reasons for the differences in APB propagation between this HPVE film and the previous results using CL-VPE are not clear given our limited knowledge of the exact growth conditions. However, the previously discussed stability of {110} facets under the HVPE growth conditions utilized is an intuitively appealing condition. Firm conclusions about the APB propagation dependence on growth conditions await more extensive thick growth results, but two things are clear from our limited experiments. First, the same basic reaction can yield GaAs films with radically different APB propagation. More importantly, there exist HVPE conditions under which APBs propagate in stable vertical fashion through film thicknesses useful for bulk frequency conversion.

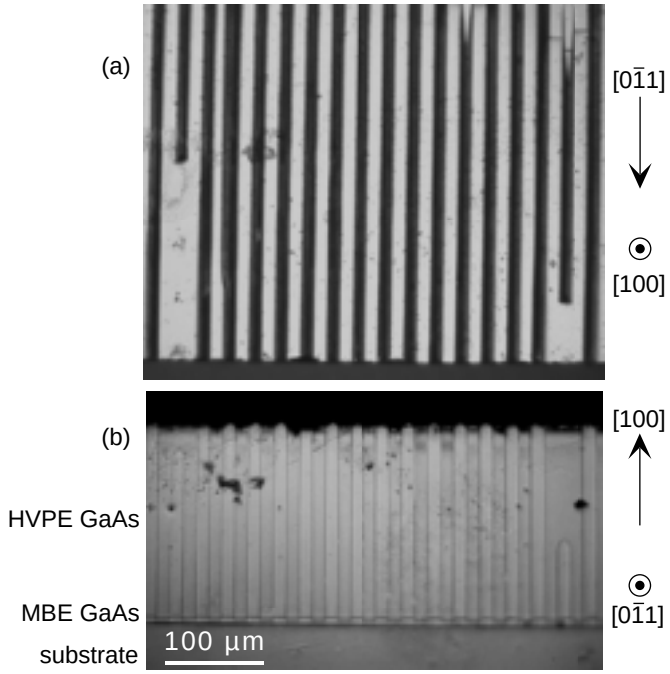

Figure 5.2: Stain-etched 200-µm-thick OPGaAs film with 27-µm domain period grown by HVPE showing a) top view and b) polished cross section. Grating k-vector is aligned antiparallel to in-plane surface misorientation direction.

5.3 Characterization of thick GaAs films

In this section we examine three important aspects of thick GaAs growth which affect the ultimate film and domain quality. We find a dependence on grating direction relative to the surface misorientation, examine the surface morphology and its connection to the growth rate, and observe two types of defects across the surface which degrade the domain quality.

5.3.1 Grating orientation and domain quality

To understand the effects of grating orientation on the domain quality, we can compare the results presented in the last section with gratings having k-vectors aligned in the orthogonal direction, so that the grating k-vectors are parallel to the in-plane substrate misorientation direction $[1\bar{1}0]$. Figure 5.3 illustrates two possible relative orientations of the grating k-vectors with respect to the atomic terrace steps running down the surface. To remove any ambiguity, we take the direction of the steps (misorientation direction) to point down the atomic staircase. Figure 5.3a shows the case of Figure 5.2, with the step direction perpendicular to the k-vector, while Figure

5.3b shows the case with the step direction and k-vector parallel. Unfortunately, the limited number of samples grown precludes us from comparing precisely the same periods, but the differences in behavior are still sufficiently clear to draw conclusions.

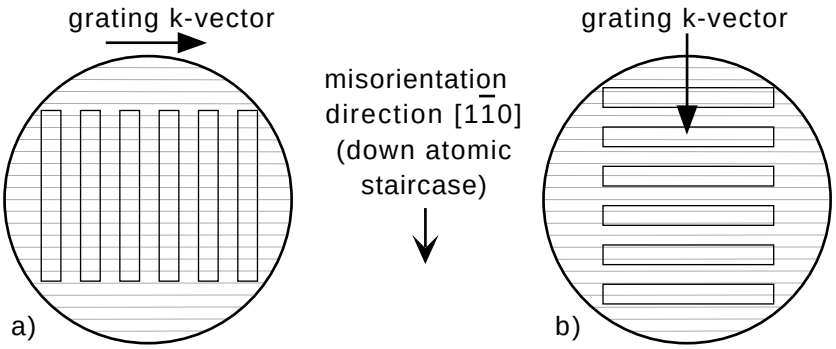

Figure 5.3: Grating k-vector alignment relative to the surface misorientation direction, a) antiparallel, b) parallel.

Figure 5.4 shows the stain-etched cross-section of a sample with misorientation direction parallel to the grating k-vector. The domain boundaries appear to be largely propagating in {110}, but now {110} is tilted with respect to the wafer surface by the 4° misorientation. Despite the fact that this sample has domains almost four times as wide as the domains in Figure 5.2, the domain quality is clearly much worse. Figure 5.4 shows one of the highest quality regions observed with this grating orientation relative to the wafer misorientation; most areas are much worse with a more corrugated surface, more overgrown domains, and more wander in the APB boundary directions. The domain growth is clearly affected by some factor which results in wide variation in domain cross-section, height, and profile. Note also that the domains in Figure 5.4 annihilate by no regular mechanism, in contrast to the symmetric domain overgrowth observed in Figure 5.2.

The most probable explanation for the difference between the two grating orientations is inhibited step flow and problematic nucleation across the APBs. The two cases are nominally identical in crystal orientation, with only the 4° misorientation breaking the symmetry. With the k-vector and the surface misorientation perpendicular, both domains can grow by simple step flow across the wafer and no nucleation of new atomic layers across APB boundaries is required except at the very end of the long domain. In contrast, for the parallel k-vector case, where step flow growth is interrupted by antiphase domain boundaries, nucleation must occur across the APB before step flow growth can proceed further across the next domain. This inhibited nucleation

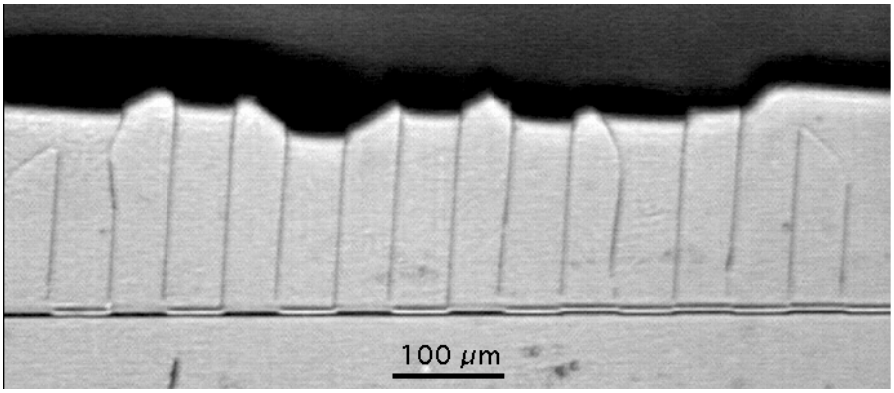

Figure 5.4: Cross-section of domains with grating k-vector parallel to the misorientation direction.

behavior leads to a pileup of grown-out atomic steps at the APB, something which was also observed in MBE growth. With the resulting large height difference at the APB, any 3-dimensional growth perturbation could result in rapid overgrowth of an adjacent domain. Also, statistical variations in the nucleation across the APBs could lead to local variations in domain height. These mechanisms would be consistent with the wide variations in domain height, surface morphology, and domain annihilation profile visible in Figure 5.4. For shorter periods, the variations are greater, such that 27-μm-period gratings do not survive through 200 μm of GaAs growth. The clear conclusion for this case with 4° misoriented wafers is that grating k-vectors should be aligned perpendicular to the misorientation direction to eliminate these problems and obtain the best quality domain gratings, particularly for shorter periods.

5.3.2 Surface morphology

Figures 5.5a and 5.5b show the cross-sections of sample regions containing domain periods of 27 μm and 212 μm, respectively. Figure 5.5a is an unpolished cross-section that shows the surface profile before stain etching, which smooths the surface profile. The profile in Figure 5.5b is clearly visible even after stain etching due to the much larger feature size. From the cross-sections it is clear that angled facets develop on the top surface during HPVE growth. The initial difference in domain height between the two orientations on the template was approximately 1000 Å, so that the much larger height differences visible in Figure 5.2 must result from asymmetry in the HPVE process. Both surfaces develop the same profile and facet angles despite an order of magnitude difference in the period, which is not surprising given that the same crystal planes are

exposed. Comparing to previous HVPE growth experiments on stripes [8, 14], it is likely the 27-μm-period sample exhibits the equilibrium morphology, so that the 212-μm-period sample in Figure 5.4b should develop the triangular profile of Figure 5.4a with additional HPVE growth. The measured angle of the facets with respect to the GaAs wafer surface is approximately 35°, so that the facets lie near {112}.

The faceting behavior observed can be understood by reference to the heirarchy of facet growth rates observed by Gil-Lafon, *et al.* [8] under HVPE growth conditions consistent with primarily {110} sidewalls. Consider first the growth of a uniform <110> stripe of each orientation growing in isolation, with the surrounding surface masked. In this case, Gil-Lafon, *et al.* observed that both of the isolated domains have approximately the same shape as the domains observed in our orientation-patterned film of Figure 5.5a; one orientation has a triangular top and the other has a flat top. For the first stripe orientation, with $\{111\}_{As}$ exposed on the corners, the important facets are the low-index {100} and $\{111\}_{As}$. Since the {100} growth rate is much higher than the $\{111\}_{As}$ rate, the stripe tops exhibit {111} facets and appear triangular in cross-section. For the orthogonal stripe orientation, the important facets are {100} and the $\{111\}_{Ga}$, which would be exposed on the corners. With the high growth rate measured on $\{111\}_{Ga}$, one observes that the stripe corners grow out quickly and leave a flat {100} top, exactly like the flat top domains in Figure 2.5a. The exhibition of approximately {112} on the triangular domains in our orientation-patterned films rather than {111} may result from effects of the nearby APB or adjacent domain of opposite orientation. Either of these could could change the nucleation rate at the bottom of the facet and therefore modify the angle from what one would expect with an isolated stripe. It is unclear exactly how the surface morphology might affect the APD propagation, especially in the presence of defects of the kinds discussed in the next section. The only clear conclusion is that this equilibrium morphology is compatible with overall vertical APB propagation.

One can speculate about the overall growth rate of the orientation-patterned surface by considering the facets exposed on the surface, as illustrated in Figure 2.6. Under these growth conditions, triangular domains would be expected to exhibit a slow growth facet $\{111\}_{As}$ on both sides and therefore necessarily grow slowly. The flat domains would grow vertically at the {001} growth rate and should preserve their rectangular shape due to the presence of the slow growth {110} exposed on the sidewalls. The two isolated domains would thus be expected to grow at significantly different rates, yet in Figure 5.5 the equilibrium angled and horizontal facets of the two domains meet at the APB boundaries. This indicates that the overall growth rate is somehow cou-

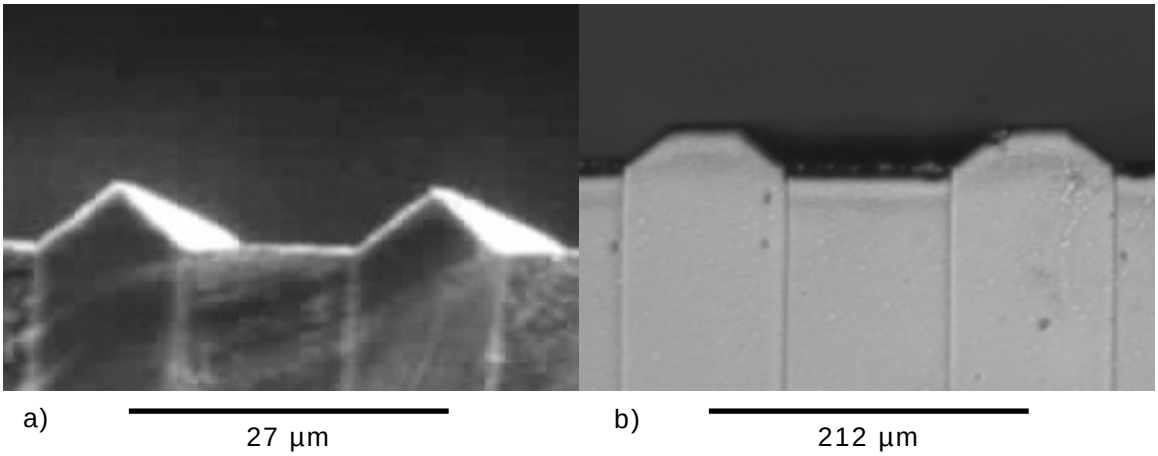

Figure 5.5: Surface morphology of 27-µm- and 212-µm-period OPGaAs films. The 27 µm period sample was cleaved; the 212 µm period sample was polished and stain-etched.

pled across the APB. This overall rate must be dominated by the higher {001} growth rate on the flat surfaces. The flat domain will grow at the rate-limited {100} growth rate, but have straight {110} sidewalls. Thus, it will tend not to overgrow the adjacent triangular domain, bounded as it is by the slow growth {110} which becomes the APB plane, at least in the absence of 3-D surface perturbations. As the rectangular domain grows it might well enhance the probability of nucleation of layers on the angled facet across the APB boundary. Addition of atoms to the flat domain would increase the number of nearest neighbor bonds possible for an atom incorporating at the APB and potentially lower the barrier to nucleation of new atomic planes on the angled facet. It seems reasonable to assume that this nucleation rate at the base of the angled facet would be proportional to the growth rate on the flat (001) surface. Growth on the angled facet could then occur primarily by step flow growth from the APB nucleation region up towards the peak, resulting in an angled facet whose net vertical growth rate matched that of the {001} surface. This explanation could account for the tilt direction of the angled facet away from {111} towards {112} and for the resulting approximately uniform growth rate across the surface.

5.3.3 Domain defects

Figure 5.7 shows the top view of the 27-µm-period domain sample exhibiting a variety of domain defects. Almost all the interrupted domains can be associated with two kinds of defects, individual domain interruptions and pyramidal 3-D growth defects which disrupt multiple domains. On any given cross-section through the 27-µm-period sample, approximately 10% of

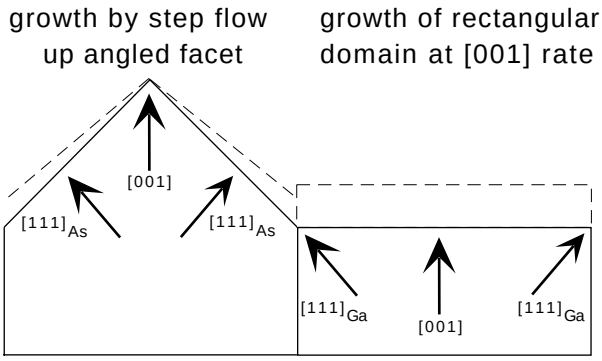

Figure 5.6: Schematic illustrating faceting and growth of adjacent OPGaAs domains.

the domains are interrupted. Figure 5.7 is not representative of the sample as a whole, as it has a much higher density of the pyramidal defects than is present on average across the surface, but it illustrates well the main types of defects and their features.

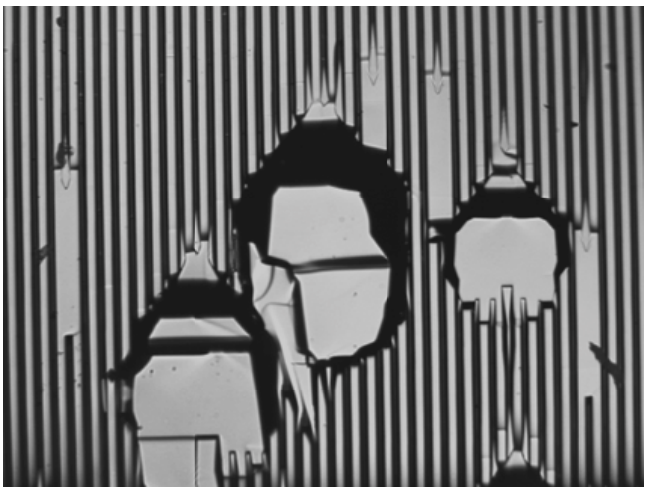

Figure 5.7: Top view of 27-μm-period OPGaAs with domain interruptions and pyramidal defects.

The domain interruptions have exactly the same length in each case, approximately 270 μm. In contrast, the 212-μm-period sample exhibits no such domain interruptions. The presence of interruptions on the 27-μm-period sample and not the 212-μm-period sample argues for some dependence of interruption nucleation on domain width. The polished cross-sections of 27-μm-period samples intersect several interrupted domains, which allows us to determine the cross-

sectional profiles of these defects. For each interrupted domain we can measure the height at which the domain closes over and the remaining interrupted distance between the polished edge and the point where the domain is again observable on the sample surface. Figure 5.8 illustrates these quantities.

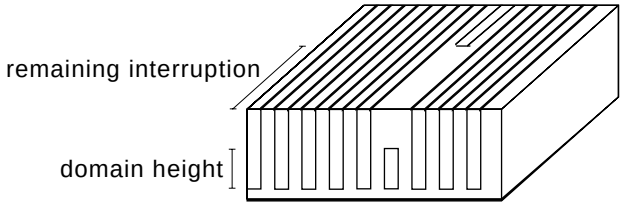

Figure 5.8: Schematic of interrupted domain quantities used to determine domain profiles.

Figure 5.9 shows the interrupted domain heights at the polished cross-section as a function of the distance from the edge of the interruption. The fact that the domain heights fall on a sharp line indicates that each domain interruption has the same cross-sectional profile. The uniform domain interruption length and cross-section indicate a similar origin for the interruptions, while the profile points approximately back toward the template as the origin. The solid line fit in figure 5.9 is at approximately 32.9° with respect to the wafer surface, which when added to the 4° ± 0.5° wafer misorientation corresponds approximately to the 35.3° expected for a boundary propagating in the {112} plane. Note that the asymmetry in the domain interruption must result from the 4° wafer misorientation, since otherwise the domain interruption ought to be symmetric. The dashed line in Figure 5.8 is a guess about the profile of the opposite side of the domain interruption which connects the re-appearance of the domain on the surface with the probable location of the defect in the template. However, no cases were seen in the polished cross-sections with inverted domains suddenly appearing some distance up in the film. Possible origins of the interruptions include oval defects in the original MBE growths (either in template or regrowth), dirt/contamination from wet processing, or lithograpy defects. All three would be consistent with the linewidth dependence we see of the interruptions. The characteristic size of the defect may need to be sufficiently large to interrupt the whole domain, something more probable for narrow domains than wide ones. As this problem appears to originate at the template, improved template processing should result in a reduction of the interruption density.

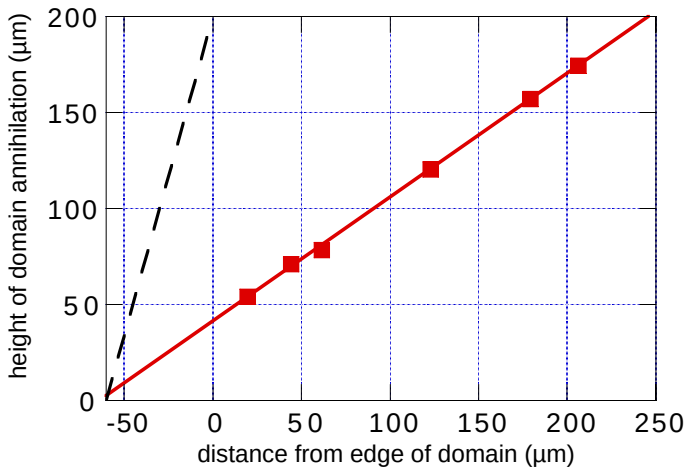

Figure 5.9: Domain interruption shape determined from domain annihilation heights at polished cross section. The solid line shows a linear fit to the observed domain annihilation heights, while the dashed line shows expected profile for the opposite boundary of the interruption.

A "pyramidal" type defect is also visible in Figure 5.7 on the top surface. The density of these pyramidal defect is higher on the 27-μm-period sample than the 212-μm-period sample, though the density varies across the surface of both samples. Such pyramids are also observed in regions without any domain patterning, though insufficient sample area exists to make any quantitative comparison between densities on various patterned and unpatterned regions. Examining the top surface of the film in Fig. 5.7, we see that the pyramidal defects, unlike the single-domain interruptions discussed previously, appear in a range of sizes. Figure 5.10 shows a cross-section of such a pyramidal defect illustrating the typical lateral expansion with increasing film thickness. Provided that the pyramidal defects all have similar cross-section, which seems reasonable given the similarity of their surface appearance and of the few cross-sections available, the size range indicates that the pyramidal defects do not have a uniform origin at the template, but rather nucleate during HVPE process. The higher density on the shorter period samples also suggests that these defects are coupled (though not exclusively) to the presence of APBs.

5.3.4 Projections for thicker films

Thicker OPGaAs layers would clearly have much greater utility for frequency conversion devices, expecially those in the mid-IR regions where diffraction will be greater due to the longer wavelengths involved. The vertical APB propagation observed under these growth conditions should not limit thicker growth, but the observed defects will cause some degradation in domain

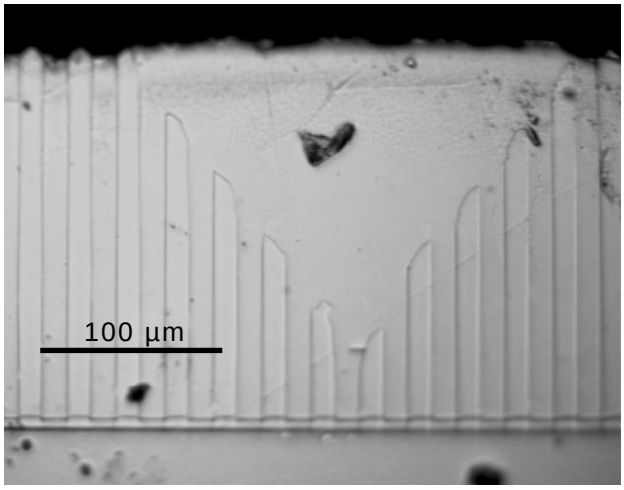

Figure 5.10: Cross-section of pyramidal defect on 27 µm domain HVPE film.

quality unless eliminated. As discussed earlier, the domain interruptions are increasing in size with film thickness. At 200-µm-film-thickness, a typical cross-section through the sample has approximately 10% of the inverted domains interrupted; that fraction appears to increase linearly with increasing film thickness. Assuming that the domain interruptions do not merge, thereby reducing their overall effect, by 0.5 mm thickness the effective nonlinear coefficient at the film surface would be reduced by approximately 25% in a film with similar defect densities, though the center of the film would see only a 12.5% reduction. This fraction is largely consistent with subsequent measurements on 500-µm-thick films, where approximately 20% of the inverted domains have interruptions on a typical cross-section [16]. The pyramidal defects will cause similar problems, since they increase in both size and density with increasing film thickness. In order to grow very thick films (~1 mm) with uniform quality domains and consistent nonlinear coefficient, the quality of the templates must be improved and the HPVE process optimized to minimize pyramidal defect growth.

5.4 Linear optical characterization

We measured optical transmission in OPGaAs at both long and short wavelength to assess usefulness for nonlinear optical frequency converison. The optical absorption in GaAs is dominated by diffferent mechanisms in different wavelength ranges [17]. Just below the band edge the dominant absorption is the intrinsic Urbach edge, which falls exponentially below the band edge

and results from phonon-assisted interband transitions. At long wavelength, free carrier and intraband absorption effects will dominate. In between the free carrier and Urbach regimes the spectrum will be dominated by absorption due to traps, defects, and impurities in the GaAs.

The Urbach tail absorption in the near band edge region can be expressed as

$$\alpha(h\nu) = \alpha_f \exp\left(\frac{h\nu - E_f}{E_0(T)}\right), \tag{5.1}$$

where E_f is the Urbach focus energy, α_f is the absorption at the Urbach focus, and $E_0(T)$ is a temperature dependent Urbach slope parameter [18]. For undoped GaAs at room temperature, E_f = 1.93 eV, $\alpha_f = 2\times10^{33}$ cm^{-1}, and $E_0(T) = 7.5$ meV. At 1-μm wavelength, which is the shortest wavelength likely to be used in OPGaAs, the extrapolated room temperature absorption coefficient due to the Urbach tail is 2×10^{-7} cm^{-1}. Thus, this Urbach tail should not contribute to absorption in the crystal unless the temperature is elevated. Following the same model, raising the crystal temperature to 141°C will result in approximately 1×10^{-2} cm^{-1} absorption at a wavelength of 1 μm. As a result, the absorption magnitude in the near-IR wavelength range will be determined by the concentrations of impurities, defects, and dopants grown into the crystal [17, 18]. These absorptions have complicated frequency dependent spectra and no attempt will be made to discuss them here, except to note that reduction in the concentrations of such extrinsic contributors will reduce the absorption losses in the crystal.

Attenuation at short wavelength was measured in OPGaAs film regions with 27-μm domain periods and adjacent regions with plain GaAs in a 500-um-thick film grown at Thomson-CSF [19]. Beams at wavelengths of 1.064 μm, 1.32 μm and 1.55 μm wavelength were confocally focused through the 2 cm long samples. The transmitted 1.064 μm radiation was measured using thermal detectors and large area photodiodes. Corrections for Fresnel reflections at normal incidence were made using the refractive index model in equation 3 of Pikhtin and Yaskov [20]. The sample endfacets were not polished exactly parallel to one another, so that multiply reflected beams walked off the detector and etalon effects could be ignored. Table 5.1 shows the measured attenuation for various wavelengths.

The attenuations measured in OPGaAs near the band edge are quite low compared to bulk GaAs crystals which typically have absorptions of several cm^{-1}, a fact which is undoubtedly related to the much higher purity crystals obtainable by the HVPE process. While attenuations were consistently measured to be a factor of ~1.7 greater in the orientation-patterned GaAs com-

wavelength (μm)	attenuation in orientation patterned GaAs (cm^{-1})	attenuation in unpatterned GaAs (cm^{-1})	ratio of patterned to unpatterned attenuation
1.064	0.114	0.071, 0.025±0.007*	1.6
1.319	0.058	0.033	1.8
1.56	0.034	0.02	1.7
10.6		0.2 (only upper bound due to beam clipping)*	
* measured in 200 μm thick, 212-μm-period OPGaAs from previous growth run			

Table 5.1: Attenuation in 27-μm-period OPGaAs and HVPE GaAs.

pared to the plain HVPE GaAs, the values are already in the range of other practical nonlinear optical materials such as $ZnGeP_2$. The decreasing attenuation with increasing wavelength would be consistent with both absorption and scattering loss mechanisms, so we can't yet determine which provides the dominant contribution, though it appears free carriers are not implicated, as their absorption would increase rapidly with wavelength. The fact that these low values were obtained after only three thick-OPGaAs growth runs suggests that further optimization is likely to reduce the attenuation even further. Since 27 μm is the proper period for pumping parametric amp1ification with a 1.32 μm pump laser, attenuation values for 1.32 μm and 1.56 μm can be considered realistic worst-case values for modeling device operation. Pumping at 1.064 μm will require shorter periods which might increase further the attenuation. The measurements were not sensitive to the beam location within the crystal until it came close to the top air/GaAs interface or the highly doped substrate. These attenuation results are much larger than the extrapolated limit set by the Urbach tail and are in the range where several effects (impurity absorption, domain boundary scattering, scattering from morphological defects) could contribute to our measured value. Further experiments are necessary to measure in detail the spectral dependence of this absorption and determine its origin.

Long wavelength transmission was measured at 10.6 μm with a CO_2 laser in films with a 212-μm-domain period. The CO_2 laser beam was focused confocally within the OPGaAs to an approximately 50-μm-waist size in a 200-μm-thick crystal. The measured absolute transmission through the 4.6 mm sample was 50.6%. Using the refractive index model of Pihktin and Yaskov [20] for GaAs at 10.5 μm, we calculate the theoretical transmission including two fresnel reflections to be 51.4%. Multiple reflections in the GaAs sample could increase the theoretical transmitted power to a maximum of 55%. We can thus place an upper bound on the losses within the GaAs sample at 10.5 μm to be ~ 0.2 cm^{-1}, assuming unattenuated multiple reflections, or ~ 0.03 cm^{-1} in the more likely scenario where the contribution of multiple reflections is negligible. The attenuation actual value is most likely even lower, since the dominant loss mechanism in this sample is

probably clipping at the interfaces. The beam diameter at the input and output facets was approximately 141 μm and the aperture is only 200 μm wide, so some clipping inevitably occured at the top air/GaAs interface. Additionally, the high doping level of the substrate (n = 1-4 $*10^{18}$) will cause free carrier absorption of the long wavelength beam where it samples the substrate. Repeating of these measurements using thicker films will allow more accurate measurement of the long wavelength absorption and will elucidate whether domain densities required for near-IR pumping have any impact on mid-IR transmission.

5.5 Nonlinear optical characterization

We demonstrated frequency conversion in orientation-patterned thick GaAs by generation of 5-μm second harmonic radiation from a 10 μm fundamental. This interaction was selected because only 212-μm-period samples were available with interaction lengths as large as several mm. The pump laser was a grating tunable CW CO_2 laser with an output power of approximately 2 W. The CO_2 radiation was focused using CaF_2 lenses to a waist of 50 μm in radius inside the 4.6-mm-long GaAs sample, as measured by the razor blade technique. The power at the fundamental frequency was measured with a thermal power meter which could be inserted and removed from the beam. The harmonic radiation was measured using a mechanical chopper and a pyroelectric detector. Sapphire filters were placed before the pyroelectric detector to filter out the residual pump radiation before incidence on the pyroelectic detector. We determined empirically that the sapphire was of sufficient thickness to remove the residual pump radiation. The pump beam was aligned through the 200-μm-thick sample by observing the beam reflected from the facet and by measuring the pump radiation through the sample. The pump radiation was polarized in the plane of the GaAs wafer surface, while the harmonic radiation was polarized normal to the GaAs wafer surface. While this polarization combination didn't offer the highest possible nonlinear coefficient (polarized along {111}), it did allow straightforward alignment with the optics available. Figure 5.11 shows the measured internal conversion efficiency as a function of the internal harmonic power at 10.5-μm fundamental wavelength. The efficiency exhibits a parabolic dependence on input power and from it we can extract an effective nonlinear coefficient of 48 pm/V, which should be compared to the 57 pm/V we predict for this polarization configuration assuming d_{14} = 90 pm/V. This calculation and the ones following utilize equation 2.63 with a confocally focused TEM_{00} beam so that $h(0,\xi) = 0.8$. In practice, we observed the pump laser mode to have some

asymmetry, which may account for some of the difference between the theoretical prediction and experiment .

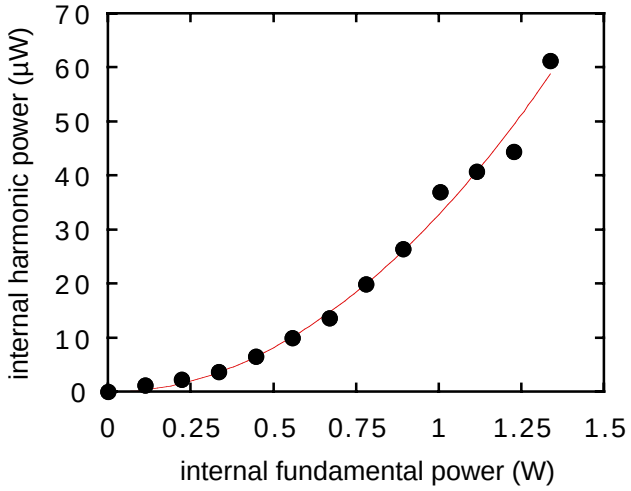

Figure 5.11: Harmonic power as a function of 10.5 μm fundamental power for 4.6 μm orientation-patterned GaAs with 212 μm domain period.

Figure 5.12 plots the normalized conversion efficiency of this crystal as a function of pump wavelength, both experimental and theoretical. As expected, the observed efficiency falls off away from the optimal phasematching point of 10.6 μm, though somewhat more quickly than would be predicted by theory. Unfortunately, the CO_2 laser was insufficiently tunable to observe an unambiguous efficiency peak, so it is possible the actual peak differs in wavelength from the predicted one. The solid theoretical curve shows the tuning behavior expected from the dispersion model of equation 3 in Pikhtin and Yaskov [20]. This prediction is quite sensitive to small changes in the dispersion; changing the dispersion between fundamental and harmonic by $\Delta n = 0.0003$ results in the dashed curve. Note that subsequent work has found equation 4 of Pikhtin and Yaskov to predict phasematching wavelengths more accurately. In any case, reference [20] quotes an RMS deviation between data and model of 0.004, larger than that necessary to explain the discrepancy between model and data. If the dispersion relation used to generate the dashed curve is correct, the best fit value is 55 pm/V, which is very close to the 57 pm/V expected if d_{14} equals 90 pm/V. Thus, we demonstrate a harmonic generation efficiency near that expected theoretically in the first nonlinear optical experiment in thick orientation-patterned GaAs.

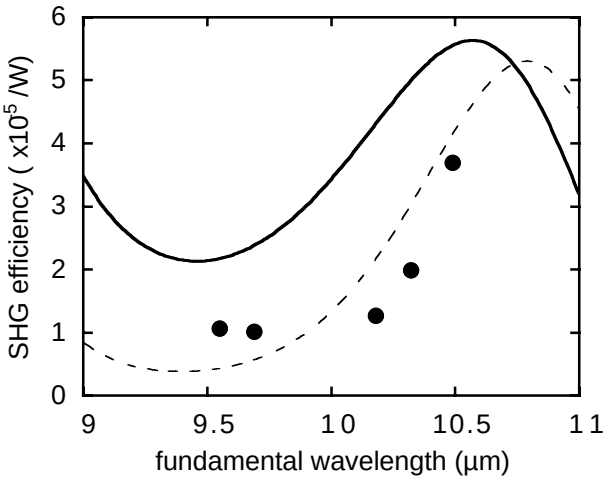

Figure 5.12: Conversion efficiency of CO_2 laser frequency doubling vs. wavelength. Solid line shows theoretical tuning behavior for dispersion of [20]. Dashed line shows theoretical tuning with dispersion shift of 0.0003.

5.6 Conclusion

Thick orientation-patterned GaAs films have been grown using HPVE on the orientation templates described in previous chapters. Films up to 200 μm in thickness exhibit excellent domain quality with vertical APBs down to periods around 30 μm. This stable vertical domain propagation should allow growth of much thicker GaAs films (>500 μm) with similar domain quality. Transmission measurements on these films confirm low attenuation losses at both long and short wavelengths, while harmonic generation measurements in an orientation-patterned thick GaAs film achieve near-theoretical efficiency. One can conclude from these results that thick orientation-patterned GaAs can achieve the properties required for effective frequency conversion, with high domain quality for quasiphasematching, large aperture, long crystal lengths, and high transparency.

References

1. L.A. Eyres, P.J. Tourreau, T.J. Pinguet, C.B. Ebert, J.S. Harris, M.M. Fejer, B. Gerard, and E. Lallier, "Quasi-phasematched frequency conversion in thick all-epitaxial, orientation-patterned GaAs," *Advanced Solid State Lasers*, OSA Trends in Optics and Photonics Vol. 34, H. Injeyan, U. Keller, and C. Marshall, eds. (Optical Society of America, Washington, DC, 2000) pp. 259-261.

2. L.A. Eyres, P.J. Tourreau, T.J. Pinguet, C.B. Ebert, J.S. Harris, M.M. Fejer, L. Becouarn, B. Gerard, and E. Lallier, "All-epitaxial fabrication of thick, orientation-patterned GaAs films for nonlinear optical frequency conversion," Appl. Phys. Lett. **79**, 904-906 (2001).

3. G.B. Stringfellow, *Organometallic Vapor-Phase Epitaxy: Theory and Practice* (Academic Press, San Diego, 1999).

4. J.M. Durand, "Influence of the growth parameters in GaAs vapour phase epitaxy," Philips J. Res. **34**, 177-210 (1979).

5. J.L. Gentner, "Vapour phase growth of GaAs by the chloride process under reduced pressure," Philips J. Res. **38**, 37-76. (1983).

6. L. Hollan, J.M. Durand, and R. Cadoret, "Influence of the growth parameters in GaAs vapor phase epitaxy," J. Electrochem. Soc. **124**, 135-139 (1977).

7. D.W. Shaw, "Kinetic aspects in the vapour phase epitaxy of III-V compounds," J. Cryst. Growth **31**, 130-141 (1975).

8. E. Gil-Lafon, J. Napierala, D. Castelluci, A. Pimpinelli, R. Cadoret, and B. Gerard, "Selective growth of GaAs by HVPE: keys for accurate control of the growth morphologies," J. Cryst. Growth **222**, 482-496 (2001).

9. F. Chavez, J. Mimila-Arroyo, F. Bailly, and J.C. Bourgoin, "Epitaxial GaAs by close space vapor transport," J. Appl. Phys. **54**, 6646-6651 (1983).

10. F. Bailly, G. Cohen-Solal, and J. Mimila-Arroyo, "Simplified theory of reactive close-spaced vapor transport," J. Electrochem. Soc. **126**, 1604-1608 (1979).

11. N. Pütz, E. Veuhoff, K.-H. Bachem, P. Balk, and H. Luth, "Low pressure vapor phase epitaxy of GaAs in a halogen transport system," J. Electrochem. Soc. **128**, 2202-2206 (1981).

12. M. Yoshida, H. Terao, and H. Watanabe, "Thermodynamic and experimental study of low pressure $Ga/AsCl_3/H_2$ VPE," (1986).

13. J. Napierala, E. Gil-Lafon, D. Castelluci, A. Pimpinelli, and B. Gerard, "Control of the growth morphologies of GaAs stripes grown on patterned substrates by HVPE," Optical Mater. **17**, 315-318 (2001).

14. E. Gil-Lafon, J. Napierala, D. Castelluci, A. Pimpinelli, B. Gerard, and D. Pribat, "Kinetic modelling of the selective epitaxy of GaAs on patterned substrates by HVPE. Application to the conformal growth of low defect density GaAs layers on silicon," *III-V and IV-IV Materials and Processing Challenges for Highly Integrated Microelectronics and Optoelectronics*, Mater. Res. Soc. Symp. Proc. 140, S.A. Ringel, E.A. Fitzgerald, and I. Adesida, eds. (Materials Reseach Society, Pittsburgh, PA, 1998) pp. 33-38.

15. Y. Li and L.J. Giling, "A closer study on the self-annihilation of antiphase boundaries in GaAs epilayers," J. Cryst. Growth **163**, 203-211 (1996).

16. T.J. Pinguet, O. Levi, T. Skauli, L.A. Eyres, L. Scaccabarozzi, M.M. Fejer, J.S. Harris, T.J. Kulp, S. Bisson, B. Gerard, L. Becouarn, and E. Lallier, "Characterization of 0.5 mm thick films of orientation-patterned GaAs for nonlinear optical applications," *Conference on Lasers and Electro-Optics*, OSA Trends in Optics and Photonics (TOPS) Vol. 56 (Optical Society of America, Washington, DC, 2001) p. 138.

17. J.I. Pankove, *Optical Processes in Semiconductors* (Prentice-Hall, Englewood Cliffs, NJ, 1971).

18. S.R. Johnson and T. Tiedje, "Temperature dependence of the Urbach edge in GaAs," J. Appl. Phys. **78**, 5609-5613 (1995).

19. T.J. Pinguet, personal communication to L. Eyres (2001).

20. A.N. Pikhtin and A.D. Yaskov, "Dispersion of the refractive index of semiconductors with diamond and zinc-blende structures," Sov. Phys. Semicond. **12**, 622-625 (1978).

CHAPTER 6: High Power Operation and Future Devices

6.1 Introduction

With the successful demonstrations of the preceeding chapters, we can now explore opportunities and limitations for nonlinear optical devices employing orientation-patterned GaAs crystals. Orientation-patterned GaAs films now exist with excellent domain quality, proper phase-matching periods for short wavelength pumping, large aperture, low attenuation losses and cm-scale device lengths. This state of the art should allow operation of devices at low peak and average power levels such as the CW devices examined in chapter 2. Recent new results [1] have confirmed the usefulness of orientation-patterned GaAs for CW frequency conversion at low power levels. DFG between 1.3 μm and 1.55 μm laser diodes produced 8-μm radiation with near the expected theoretical efficiency and confirmed that the OPGaAs crystals were optically homogeneous and quasi-phasematchable over a 2 cm length. For many of the desired higher peak and average power devices, however, several other previously unconsidered limitations which will constrain device design and operation. In this chapter we will investigate these limitations and the effects they will have on the performance of high power devices, including optical parametric amplifiers and optical parametric oscillators.

6.2 Constraints on high power operation

The constraints on high-power frequency conversion fall into two categories, intrinsic limitations and extrinsic limitations. Intrinsic limitations are inherent characteristics of the GaAs, such as two-photon absorption. Extrinsic limitations are due to residual nonidealities in the GaAs which may be improved in wavelength ranges of interest through improved fabrication processes, such as optical scattering from crystal defects or absorption above the intrinsic levels set by the Urbach tail and the phonon bands. The damage threshold could fall into either category, since one can hypothesize both an intrinsic damage threshold and a lowered threshold due to crystal imperfections. This section will review the three effects most likely to limit high peak and average power frequency conversion: the damage threshold, thermal effects associated with absorption, and two-photon absorption.

6.2.1 Damage threshold

One unavoidable limit on the operation of nonlinear optical frequency conversion devices is the threshold at which the crystals suffer physical damage from the optical radiation. Typically, the endfacets are the most likely locations for such damage to occur. The damage properties of GaAs at 2 μm have been measured by Peterson, *et al.* in conjunction with measurements of the $ZnGeP_2$ damage threshold [2]. The average damage threshold was observed to be 5.3 ± 1 J/cm^2 for 70 ns pulses in both diffusion-bonded GaAs stacks and individual vertical-gradient-freeze (VGF) GaAs wafer pieces in experiments with 2 μm beams which are well within the transparency range and outside the range of two-photon absorption. All damage was observed on either the front or rear surfaces of the GaAs crystals. Measurement was made by exposure of the sample to 10 pulses at the given energy level with damage detected by audible sounds or effects on transmission and confirmed by microscopic examination. In similar measurements on $ZnGeP_2$, the authors found that the energy threshold was approximately constant over a wide range of temporal pulse lengths ranging from 150 ps to 200 ns, while for longer pulses (250 μs) the energy threshold increased by two orders of magnitude. The authors speculate that if the energy is deposited faster than a characteristic thermal relaxation time of the crystal (estimated to be in the 100s of μs regime), the pulse format has little impact on the damage threshold and the damage depends on energy deposition alone. Similar results were obtained in measurements on $AgGaSe_2$ at the same wavelength [3]. This seems the best assumption to use in the absence of explicit data for damage threshold behavior in GaAs. Note, though, that there are some indications that this energy damage threshold depends on the definition and experimental configuration. Lallier [4] observed damage in GaAs crystals at over longer times with higher repetition rates that exhibited a lower damage threshold than that observed by Peterson. There could be damage accumulation mechanisms which serve to lower the damage threshold over time. Further investigation will be necessary to elucidate these issues in the HVPE-grown GaAs crystals, since these damage mechanisms might well depend on the processing history of the GaAs, crystal quality, and impurity concentrations.

6.2.2 Thermal effects

For high average power operation, thermal non-idealities can cause performance limitations below those of the damage threshold. These thermal effects are caused by absorption of the radiation from the pump beams and can affect both the beam quality and the phasematching uniformity. Optical absorption at the pump or other frequencies will lead to thermal gradients across the beam which produce thermal lensing through the thermo-optic effect. Such a thermal gradient

across the beam can also cause phasematching variations across the beam which reduce the nonlinear gain. Thermal gradients along the length of the crystal due to significant pump absorption can also limit the useful crystal length. Any detailed analysis of thermal effects on the conversion efficiency in parametric devices is beyond the scope of this dissertation, so we will instead try to understand the performance of GaAs-based frequency conversion devices by comparing their probable performance with that of $ZnGeP_2$, which has similar nonlinear and thermal properties. Bordui and Fejer [5] examine these deleterious thermal effects and develop two figures of merit which quantify the impact of thermal gradients across the beam on phasematching and thermal lensing, respectively. In the simplest model, the amount of thermal dephasing across a Gaussian beam is proportional to the pump power independent of beam size, while the focal length of an induced thermal lens is proportional to the pump beam intensity (Power/beam area). The magnitude of the thermal dephasing normalized to the mixing efficiency provides one figure of merit

$$\mathrm{FOM_{TD}} = \frac{d_{eff}^2 k_{th}}{\alpha_{pump} n^2 \left(\frac{\partial \Delta n}{\partial T}\right)}, \tag{6.1}$$

while the magnitude of the thermal lensing normalized to the mxing efficiency yields another

$$\mathrm{FOM_{TL}} = \frac{k_{th}}{\alpha_{pump} \left(\frac{\partial n}{\partial T}\right)}. \tag{6.2}$$

In these expressions, k_{th} is the thermal conductivity, $\partial \Delta n / \partial T$ is the temperature depencedence of the dispersion of the refractive indices, and $\partial n / \partial T$ is the dependence of the refractive index on temperature. For comparison of these figures of merit we take the $ZnGeP_2$ absorption at 2 μm to be 0.09 cm^{-1} [6] and the OPGaAs 2 μm absorption to be 0.034 cm^{-1}, which is the attenuation value recently measured at 1.55 μm [7] where the attenuation is observed to be decreasing with increasing wavelength. This attenuation value probably has a significant contribution from scattering, which would not contribute to the thermal load, so the actual thermal performace of OPGaAs will most likely be even better than this analysis indicates. The remainder of the material constants were obtained from [5] including the $\partial \Delta n / \partial T$ for $ZnGeP_2$ of $4.4*10^{-6}$ K^{-1} (calculated from the 40 cm-K temperature tuning bandwidth) with the exception of the $\partial \Delta n / \partial T$ for

SHG of 4 μm radiation in GaAs which was recently measured to be ~$1.5*10^{-5}$ K^{-1} [8]. Table 6.1 shows the thermal FOMs for the both GaAs and $ZnGeP_2$.

material	FOM_{TD} [GW*(pm/V)^2]	FOM_{TL} [μW]
GaAs	0.46	0.95
$ZnGeP_2$	0.45	0.022

Table 6.1: Thermal figures of merit of GaAs and $ZnGeP_2$.

The thermal dephasing FOMs are comparable for GaAs and $ZnGeP_2$, while the GaAs thermal lensing FOM is ~5x larger than that for $ZnGeP_2$. The similarity of these coefficients for GaAs and $ZnGeP_2$ indicates that GaAs-based nonlinear optical devices should behave similarly to or better than those based on $ZnGeP_2$ in high power operation. This is fortunate, because $ZnGeP_2$ has proven very robust in frequency conversion at high average power levels. Perhaps the most impressive devices have been high power 2 μm-pumped OPOs. Generation of > 10 W of mid-IR output has been demonstrated in a $ZnGeP_2$-based OPO pumped by 20 W at 2 μm [9]. The conversion efficiency was linear with pump power up to the 20 W pump power level with a 0.79 mm diameter beam waist, exhibiting none of the saturation behavior which has been observed at the 3-5 W (1 mm and 2 mm pump beam diameters, respectively) pump power levels in similar 2-μm-pumped room temperature $AgGaSe_2$ OPOs [10]. This saturation in $AgGaSe_2$ OPOs was determined to be caused by thermal lensing [11]. Given the properties of GaAs and the linear dependence of the thermal lensing on pump intensity, one would expect a GaAs OPO to operate without significant thermal lensing effects at average pump intensities several times greater than those already demonstrated in $ZnGeP_2$ (8 kW/cm^2). Similarly, since the thermal dephasing depends linearly on the pump power, one could expect GaAs to handle average pump power levels in excess of 20 W at 2 μm without suffering degredation in conversion efficiency. More detailed thermal analysis is not warranted until the contributions of absorption and scattering to the total attenuation can be separated and further investigation into the HVPE growth of OPGaAs elucidates the practical lower bound on the absorption. In any case, these calculations indicate that OPGaAs should exhibit excellent robustness in high power operation.

6.2.3 Two-photon absorption

GaAs exhibits two photon absorption (TPA) at wavelengths between the band edge and one half of the bandgap energy, so that the absorption depends on the intensity according to

$$\alpha_{total}(I) = \alpha_p + \beta I \tag{6.3}$$

where β is the TPA coefficient. For high peak power devices, this nonlinear scaling of absorption with intensity leads to significant constraints on device design and operation to prevent excessive absorption of pump radiation and associated deleterious thermal effects as discussed in the preceeding section. Figure 6.1 shows the TPA coefficient for GaAs as a function of wavelength taken from the model of Van Stryland, *et al.* [12]. Unfortunately, in the range of attractive 1-μm pump lasers, the TPA coefficient is between 20 cm/GW and 25 cm/GW, with a somewhat lower value of 12 cm/GW around 1.55 μm. Beyond 1.7-μm wavelength, the half-bandgap, TPA is naturally absent and presents no constraints on device design. Note that while the linear attenuation is typically an extrinsic characteristic for GaAs in the wavelength range of interest, being dependent on the concentrations of impurities, free carriers and physical defects which contribute to optical scattering, TPA is an intrinsic characteristic and therefore is not modifiable by improvements in crystal fabrication. The limitations on device performance associated with TPA can only be lifted by a change in material, for example by shifting the bandgap in moving to a ternary alloy like AlGaAs or to a different semiconductor like ZnSe or GaP. More detailed examination of the bound-electronic and free-carrier nonlinearities in GaAs can be found in [13].

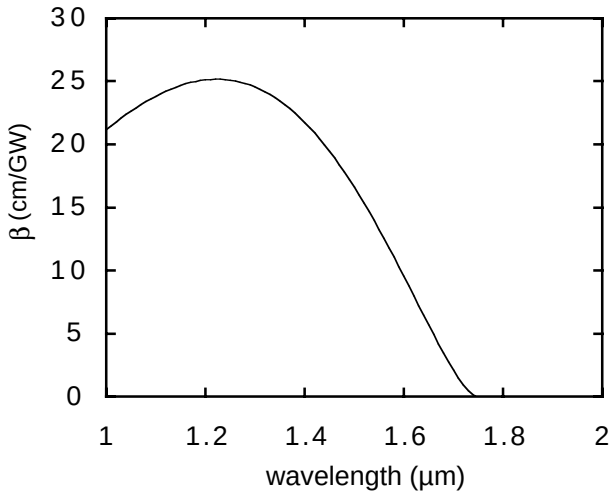

Figure 6.1: TPA coefficient as a function of wavelength for GaAs. Model comes from [12].

Plane waves propagating through GaAs in the wavelength range of TPA will be attenuated according to

$$I(z) = \frac{I_0}{\left[\exp(\alpha_p z) + \frac{\beta I_0}{\alpha_p}(\exp(\alpha_p z) - 1)\right]}, \tag{6.4}$$

with I_0 the optical intensity incident on the crystal, α_p is the linear power attenuation, and z the distance through the medium. For crystals with low linear attenuation levels we can expand the exponentials to first order to obtain

$$I(z) \approx \frac{I_0}{1 + \alpha_p z + \beta I_0 z}. \tag{6.5}$$

Ignoring the effects of linear absorption for the moment, one sees that with a TPA coefficient of 20 cm/GW, and an incident intensity of 50 MW/cm^2, half of the incident power will be absorbed in passing through a 1 cm long crystal. The effects of this absorbed power on nonlinear optical frequency conversion will depend on the actual power absorbed, but could contribute to both the damage and thermal effects. For a Gaussian beam, this effect is somewhat more complicated than for the plane wave, since the higher intensity center of the beam will be preferentially attenuated and the resulting beam profile will no longer be gaussian. The same effect will preferentially heat the central region of the gaussian beam and enhance any deleterious thermal lensing behavior. TPA also affects the pulse nonuniformly in time as well as space and serves to flatten the temporal shape. As a result of this non-uniform attenuation, the fraction of absorped pump power is smaller for gaussian pulses than for plane waves. Figure 6.2 shows the transmission of incident pump intensity/energy for plane waves, gaussian beams, and gaussian pulses in the presence of TPA. Clearly, one must remain in the regime where $\beta I_0 z < 1$ to prevent significant pump absorption.

6.3 Device modeling

This section models the performance of frequency-conversion devices including OPAs and OPOs pumped in both the non-TPA and TPA regimes. The thresholds are then compared to the limitations placed by the mechanisms of the preceeding section to evaluate feasibility of these devices. Along with the thermal effects caused by additional absorption of the pump radiation, TPA will produce gain saturation due to preferential attenuation of the highest intensity portions of the pump. For the calculations in this section, we make the simplifying assumption that the entire pump beam is attenuated by the same factor. This approximation is justified because the gain in a

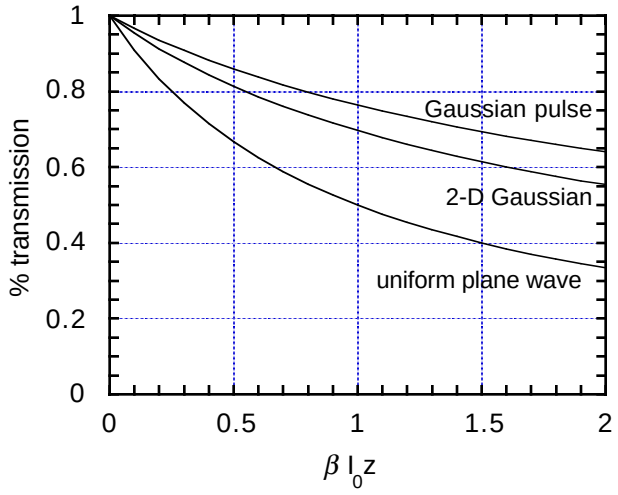

Figure 6.2: Theoretical transmission of GaAs as function of two-photon absorption. The three curves show the transmission of a uniform plane wave as described by equation 6.4, the integrated power transmission over a gaussian transverse profile, and the power transmission of a pulse with gaussian transverse and temporal profile.

high-gain parametric device is confined largely to the regions of high pump intensity. Additionally, this approximation has the benefit of overestimating the effects of TPA and thus providing an upper bound on the effect of TPA on the performance of the device.

6.3.1 OPA/OPG

The wide transparency range of GaAs through the mid-IR makes it attractive for parametric amplification of signal wavelengths in the mid-IR spectral region. With sufficient gain ($G \sim 10^{10}$) amplification of vacuum noise to macroscopic levels is even possible so that no input signal is required to generate signal and idler beams whose photon energies sum to that of the pump. To produce these high gains required for OPG, short pump pulses and high intensities are typically required. For pump wavelengths > 1.7 μm (or half the bandgap), this intensity will be limited only by the damage threshold and possible deleterious thermal effects. For shorter pump wavelengths, the intensities and gain will be limited severely by TPA.

In the absence of pump absorption, the gain in a parametric amplifier or OPO can be calculated by solving the two coupled equations

$$\frac{dE_s}{dz} + \frac{\alpha_x}{2}E_s = j\kappa_s E_p E_i^* \tag{2.6a}$$

$$\frac{dE_i}{dz} + \frac{\alpha_i}{2}E_i = j\kappa_i E_p E_s^* . \tag{2.6b}$$

For the case with input at only the signal wavelength, taking $\alpha_s = \alpha_i$ and neglecting pump depletion, one calculates a signal gain of

$$G(L) = \frac{|E_s(L)|^2}{|E_s(0)|^2} = \exp(-\alpha_s L)\cosh^2(\Gamma L) \tag{6.7}$$

for the phasematched case, where the gain is defined as

$$\Gamma^2 = \frac{8\pi^2 d_{eff}^2 I_p}{n_1 n_2 n_3 c\varepsilon_0 \lambda_s \lambda_i}, \tag{6.8}$$

I_p is the pump intensity defined as $I_p = nc\varepsilon_0 E_p^2/2$ and λ_s and λ_i are the wavelengths of the signal and idler respectively. For large gains one can approximate the cosh function as an exponential, so that the expression for gain in dB can be simplified to

$$G(\text{dB}) \approx 8.68\Gamma L - 6 . \tag{6.9}$$

For a 2-μm pump wavelength and degenerate parametric amplification in GaAs, this high gain approximation is

$$G(\text{dB}) \approx \left[\left(\frac{4.4\times10^{-3}}{\sqrt{W}}\right)\sqrt{I_p}L\right] - 6 , \tag{6.10}$$

a value which varies only slowly as one moves away from degeneracy. We assume here that the nonlinearity is 96 pm/V, which is scaled using Miller's rule from the 90 pm/V we used for 10.5 μm frequency doubling. Additionally, throughout this chapter we assume the type I phasematching configuration described in Chapter 2 in which $d_{eff} = 2d_{14}/\sqrt{3}$.

With the extremely short pulses used to obtain very large parametric gains, the useable crystal length is limited by group velocity walkoff. We can gain some idea of the behavior of such a short-pulse device by looking at short-pulse harmonic generation. For a degenerate OPA, the group walkoff length will be equal to the group walkoff length for second harmonic generation. Imeshev, *et al.* [14] investigated the effects of group-velocity mismatch on quasi-phasematched conversion efficiency and defined a figure of merit for confocal SHG

$$\text{FOM}_{\text{UF}} = \frac{d_{eff}^2}{cn_1 n_2 \delta\nu}, \tag{6.11}$$

where $\delta\nu$ is the group velocity mismatch parameter defined as

$$\delta\nu = \left(\frac{dk(\omega)}{d\omega}\bigg|_{\omega_1}\right) - \left(\frac{dk(\omega)}{d\omega}\bigg|_{\omega_2}\right). \tag{6.12}$$

With a fundamental pulse width of τ_1, the group velocity mismatch will cause the pump and generated harmonic pulses to walk off one another over a length $L_{gv} = \tau_1 / |\delta\nu|$. If the crystal length is chosen to be equal to the walkoff length in order to preserve the pulse length, the confocal SHG efficiency for a transform-limited fundamental pulse is

$$\eta_{conf} = \frac{76.7}{\varepsilon_0 \lambda_1^3} \mathrm{FOM}_{\mathrm{UF}} U_{FH} \tag{6.13}$$

where U_{FH} is the fundamental pulse energy.

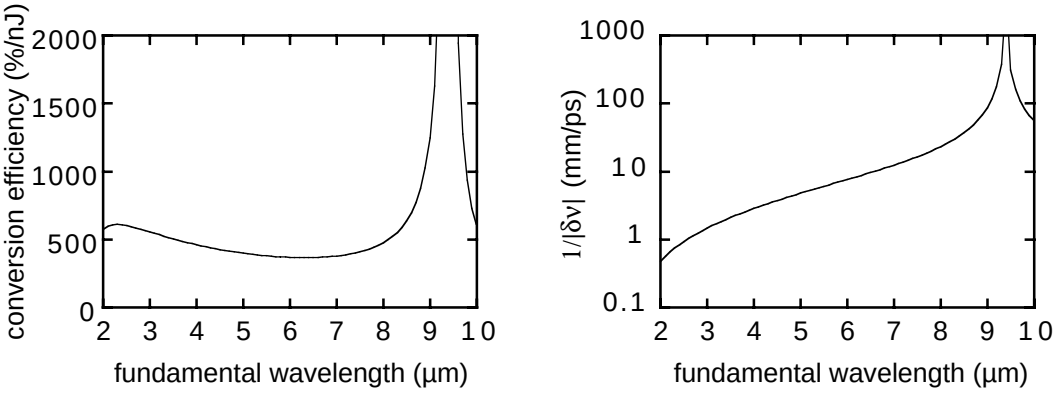

Figure 6.3: Conversion efficiency and group walkoff for SHG in OPGaAs.

Figure 6.3 shows both the confocal SHG efficiency and $1/|\delta\nu|$ as a function of fundamental wavelength. The group velocity mismatch goes to zero for a fundamental wavelength around 9.2 μm or equivalently for a degenerate OPA pumped at 4.6 μm, which permits long crystals and the very high efficiencies seen in the figure. The SHG efficiency is approximately constant around 500 %/nJ for wavelengths shorter than the region where $\delta\nu \approx 0$, which means that the parametric gain will similarly be roughly constant for the degenerate OPO with signal and idler in the same region. Note that this value is approximately 3 times larger than that of PPLN in its transparency range. More details on quasi-phasematched ultrafast SHG and DFG can be found in [14] and [15].

Since attractive lasers are available for pumping in the 1.0 μm - 1.55 μm wavelength range, it is worth exploring the constraints placed on OPA/OPG by two-photon absorption. One

can solve the same two coupled equations 6.6a and 6.6b with the pump distribution in the crystal given by equation 6.5 to obtain an approximation for the power gain of a plane wave at the signal wavelength in the presence of TPA and under the condition $\alpha_s = \alpha_i$ to be

$$G(L) = \left|\frac{E_s(L)}{E_s(0)}\right|^2 = \exp(-\alpha_s L)\cosh^2\left[\frac{2\Gamma}{(\alpha_p + \beta I_0)}(\sqrt{1 + (\alpha_p + \beta I_0)L} - 1)\right], \qquad (6.14)$$

which clearly reduces to equation 6.5 in the absence of pump absorption. Figure 6.4 shows this parametric gain for a 1-μm pump in OPGaAs and various crystal lengths neglecting absorption at the pump, signal and idler wavelengths to observe the constraints placed by TPA alone. The dashed lines show the gain without TPA, while the solid lines include the effects of TPA. The grey lines are constant intensity-length contours $\Delta = \beta I_0 L$ corresponding to absorption of some fraction of the total incident pump radiation in the nonlinear crystal. Even for long crystals (4 cm), only relatively low gains (< 10^2) are achiveable for $\Delta < 0.1$. In the presence of linear absorption at the pump wavelength, the achieveable gains are correspondingly reduced. The limitations on intensity mean that long crystals are preferred for short wavelength pumping, since they allow the same gains with lower pump intensities. Pumping at 1.55 μm instead of 1.064 μm increases only slightly (~ 3 dB) the gains achieveable before one reaches the same values of $\Delta = \beta I_0 L$ and the TPA-related absorption. TPA clearly places significant limitations on the achieveable parametric gain in the crystal. For this reason, short wavelength pumping in GaAs will be useful primarily for low gain amplifiers, such as power amplifiers and OPOs, rather than for high gain applications such as OPG. Note that large gains are possible with long crystals and high intensities, but these devices will suffer from large amounts of pump absorption and associated thermal effects which will limit the repetition rates. Additionally, high pump intensities in this wavelength range may also encounter complications from other nonlinear effects such as the nonlinear index of refraction.

6.3.2 OPOs

For OPO operation we again have the same pump wavelength regimes in which TPA is either absent or present. Considering first the case without TPA, one can use the method of Byer and Brosnan [16] to estimate pulsed SRO thresholds. For each trip around the OPO cavity during signal buildup, the signal beam is amplified or attenuated by

$$\frac{P_m}{P_{m-1}} = RG(t, L), \qquad (6.15)$$

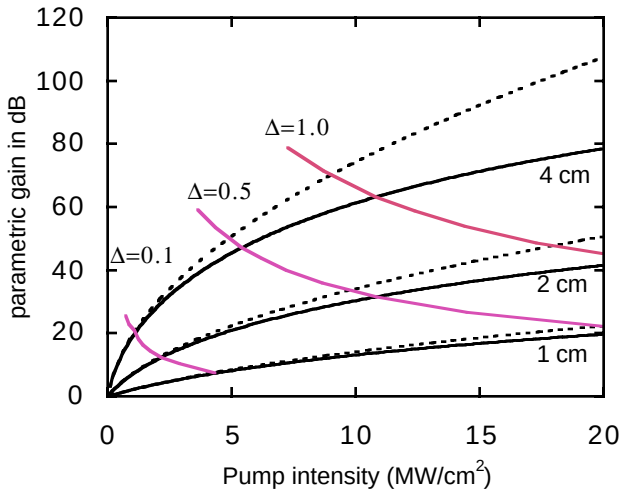

Figure 6.4: Parametric gain in OPGaAs pumped at 1.06 μm vs. pump intensity. The solid curves show OPGaAs samples of varying lengths, while the dashed curves show gain without TPA. The grey curves are plots of constant $\Delta = \beta I_0 L$ indicating magnitude of TPA. Linear absorption is neglected.

where $G(t, L)$ is the single-pass gain through the nonlinear crystal and R is the round-trip reflectivity of the cavity mirrors at the signal wavelength. For the case with linear absorption at the pump wavelength given by equation 6.4 with $\beta = 0$, the solution of equations 6.6a and 6.6b gives a single pass gain of

$$G(t, L) = \exp(-\alpha_s L)\cosh^2\left[\frac{\Gamma(t)}{\alpha_p}(\exp(-\alpha_p L) - 1)\right], \tag{6.16}$$

where $\Gamma(t)$ is given by

$$\Gamma^2 = \frac{8\pi^2 d_{eff}^2 g_s I_p(t)}{n_1 n_2 n_3 c\varepsilon_0 \lambda_s \lambda_i}, \tag{6.17}$$

and g_s quantifies the spatial coupling between the nonlinear polarization and the cavity mode according to

$$g_s = \frac{w_p^2}{w_p^2 + w_s^2}, \tag{6.18}$$

thus assuming the near-field focusing discussed in Sections 2.1.2 and 2.3.1. Starting from noise input levels, equation 6.16 can easily be numerically integrated from the noise level over many

round trips in the cavity during the assumed gaussian temporal pump pulse shape to the approximately μJ level we define as the threshold. The pump intensity is assumed constant during a single pass through the crystal for simplicity. Figure 6.5 shows the energy threshold of a 2-μm-pumped SRO generating an 8-μm idler for which the idler polarization is set to be confocal in the crystal in the same manner as was done for the DFG calculations of Chapter 2, since we use the same near-field approximation. Pump and signal beams are assumed to have the same waist diameter and are set by the constraint on the idler polarization. The threshold calculations could be extended to tighter focusing conditions using an approach like that of Guha, *et al.* [17] or Boyd and Kleinman [18] as discussed in Chapter 2, but the confocal idler case provides sufficient results for our purposes. The cavity is a bow-tie ring configuration to minimize the round-trip losses by only passing once through the OPGaAs crystal and is assumed 1 cm longer than the crystal on each end of the cavity. Each of the four mirrors is taken to have a reflectivity of R=0.99 at the signal wavelength and be perfectly transmitting at the pump and idler wavelengths, while the crystal is assumed to be antireflection coated at all wavelengths. The attenuation at pump, signal and idler wavelengths is assumed to be the same.

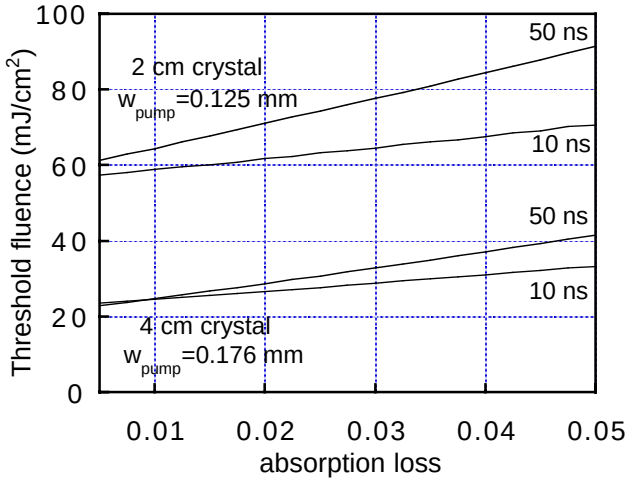

Figure 6.5: Threshold fluence of 2-μm-pumped OPO generating an 8 μm idler. Losses are assumed the same at all three wavelengths and the idler polarization is set to be confocal in the OPGaAs crystal.

The threshold pump energies extend down to ~11 μJ (22 mJ/cm^2 * 4.9×10^{-4} cm^2; see equation 2.7 and the following paragraph for the definition of effective area) for a 4-cm-long OPGaAs crystal and 50-ns pulses. Attenuation losses of 0.034 cm^{-1} at 1.55 μm have been observed in OPGaAs for periods shorter than those required for 2 μm pumping, indicating that the

range of operation of Figure 6.5 is realistic. We conclude that OPGaAs OPOs can achieve threshold at fluences more than two orders of magnitude below the 5.1 J/cm^2 material damage threshold at 2 μm discussed above. If the damage threshold under high-frequency pulsed operation is even an order of magnitude lower than this value, there should still be room to operate such low-threshold fluence OPOs. Examining thermal effects, assuming a OPGaAs OPO with 2-cm-long crystal and an ~ 80 mJ/cm^2 threshold were pumped to 5x over threshold to achieve high conversion efficiency, such an OPO could run at a repetition rate of 20 kHz before exceeding the 8 kW/cm^2 intensity value at which $ZnGeP_2$ with comparable thermal figures of merit exhibited no thermal degradation. Since the peak pump threshold intensity will remain constant as the OPO is scaled proportionally to higher power levels by increasing the beam sizes and since the thermal lens focal length scales with the intensity, thermal lensing should thus not be an issue, even at high repetition rates. We can conclude that for OPOs pumped at wavelengths outside the TPA regime, the large cushions between these threshold fluences and both the optical damage threshold and the thermal degredation regime leave significant room for optimization of OPO characteristics and adaptation to various engineering constraints. This is not surprising, since GaAs has comparable nonlinear gain and thermal properties to $ZnGeP_2$, which has been utilized for a wide range of mid-IR OPO applications.

At pump wavelengths below 1.7 μm, the practical pump intensities for an OPGaAs OPO will be constrained by TPA. Because an OPO can utilize multiple passes to achieve large gains, these constraints are somewhat less limiting than is the case for OPA devices. There are a variety of attractive pump sources available in the 1-μm-wavelength range; it is an interesting question whether or not such a 1-μm-pumped OPGaAs OPO is feasible. In the case with TPA, the gain for each round trip through the cavity is given by

$$\frac{P_m}{P_{m-1}} = R\exp(-\alpha_s L)\cosh^2\left[\frac{2\Gamma(t)}{(\alpha_p + \beta I_0)}\left(\sqrt{1 + (\alpha_p + \beta I_0)L} - 1\right)\right]. \qquad (6.19)$$

Figure 6.6 shows the threshold intensity of a 1-μm-pumped OPO generating directly an 8-μm idler as a function of the absorption at pump, signal and idler beams, which is again assumed to be equal. The OPO parameters and calculational method are the same as in the 2-μm-pumped case, with $\beta = 23$ cm/GW. The solid lines show the calculation using equation 6.19, which includes the assumption of small linear absorption at the pump wavelength, while the dashed curves show an upper bound on the threshold employing equation 6.16 with the approximation that $\alpha_p' = (\alpha_p + \beta I_0)$. The idler polarization is again set to be confocal in the 4-cm-long OPGaAs

crystal. The thresholds for 10-ns and 50-ns pulse widths are shown along with the CW threshold for the same device for comparision.

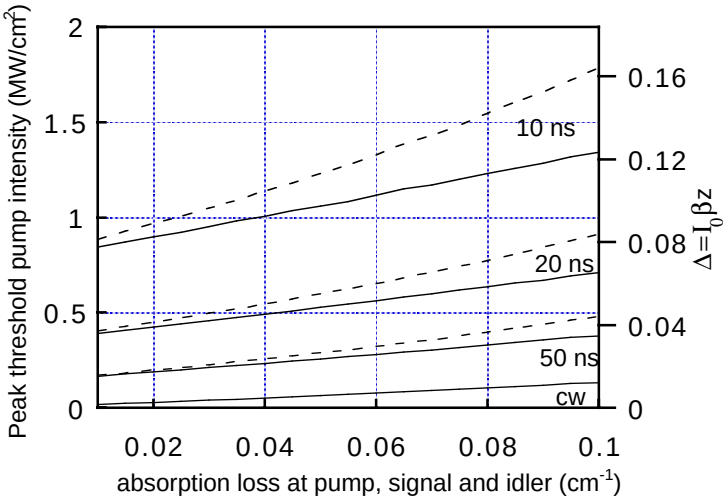

Figure 6.6: Threshold intensity for 1-μm-pumped OPO vs. GaAs absorption loss. Loss is assumed the same at all three wavelengths. OPGaAs crystal is 4-cm-long and OPO generates an 8 μm idler. Solid curves are threshold intensity with the approximation for low pump absorption of equation 6.19, while dashed curves show an upper bound.

The gain approximation for low pump absorption and the upper bound agree well in the regions of low absorption losses, as expected, and diverge more for larger absorption losses. Clearly long crystals and long pulses are optimal, since they lower the intensity threshold. Threshold intensities down to 0.2 MW/cm^2 can be obtained with 50 μs pulses and 0.005 cm^{-1} absorption with $\Delta = \beta I_o L = 0.02$. Achievement of significant conversion efficiency will require pumping several times over threshold, which will push operation into the regime where TPA will absorb non-negligible amounts of the pump radiation. Further reductions in threshold are possible by increasing the pulse length, since the CW threshold can be an order of magnitude smaller (~20 kW/cm^{-2}), but this feasibility of this strategy depends strongly on the attenuation. The 1-μm-pumped OPO feasibility will depend strongly on the absorption losses in the OPGaAs crystals. Losses at 1 μm were recently measured to be ~ 0.1 cm^{-1} at 1.064 μm in an orientation-patterned GaAs film [7], though this was on a sample having somewhat longer periods (27 μm) than those required for 1-μm pumping (8 μm - 15 μm) and is is not clear how the losses will scale with domain period. However, with low-loss crystals, long crystal lengths, and proper pulse formats, operation of a 1-μm-pumped OPGaAs OPO appears possible.

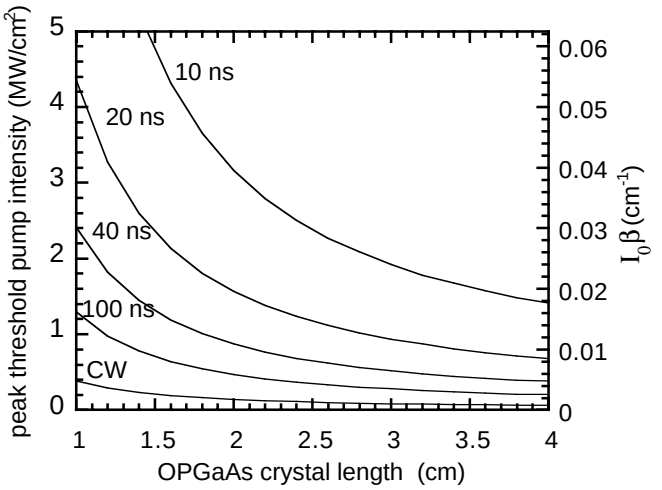

Figure 6.7: Threshold intensity for 1.5-μm-pumped OPO vs. GaAs crystal length. Loss of 0.034 cm^{-1} is assumed at all three wavelengths and OPO generates an 8 μm idler.

Figure 6.7 shows similar peak threshold intensities for 1.55 μm pumping and varying OPGaAs crystal length with the attenuation at all wavelengths set to 0.034 cm^{-1}, which was the value measured at 1.55 μm wavelength for 27-μm domain periods. Here the TPA coefficient is approximately a factor of 2 smaller (12 cm/GW) than that for a 1 μm pump wavelength. This reduction widens the window for OPO operation below TPA-related complication. Since these required periods have been demonstrated and the losses at 1.55 μm measured, this devices can be considered realistic, even at the present state of OPGaAs development. The ideal source for pumping such OPGaAs OPOs would be a quasi-CW source with long pulses, thus allowing pumping close to the CW threshold without the thermal loading required of true CW operation. Unfortunately, such lasers are more difficult to obtain than standard Q-switched lasers with shorter pulses. This pulse format may be achieveable using a master oscillator/power amplifier configuration instead of a directly Q-switched laser.

6.4 Conclusion

This chapter examined the major limitations on performance of high-peak-power devices in GaAs, including damage threshold, thermal effects, and two-photon absorption. OPA gain will be limited when pumped by 1-μm lasers, but suffers no such restrictions for pump wavelengths greater than 1.7 μm. OPO operation will be possible with 2-μm pumping for which there are large

margins between threshold and the relevant damage and thermal limitations. 1-μm-pumped OPOs look feasible in theory, but will depend on the magnitude of the attenuation losses achievable in OPGaAs with the proper domain periods.

References

1. O. Levi, T.J. Pinguet, T. Skauli, L.A. Eyres, L. Scaccabarozzi, M.M. Fejer, J.S.J. Harris, T.J. Kulp, S. Bisson, B. Gerard, L. Becouarn, and E. Lallier, "Mid-infrared generation by difference-frequency mixing in orientation-patterned GaAs," *Conference on Lasers and Electro-Optics*, OSA Trends in Optics and Photonics (TOPS) Vol. 56 (Optical Society of America, Baltimore, MA, 2001).

2. R.D. Peterson, K.L. Schepler, J.L. Brown, and P.G. Schunemann, "Damage properties of $ZnGeP_2$ at 2 μm," J. Opt. Soc Am. B **12**, 2142-2146 (1995).

3. B.C. Ziegler and K.L. Schepler, "Transmission and damage threshold measurements on $AgGaSe_2$ at 2.1 μm," Appl. Opt. **30**, 5077-5080 (1991).

4. E. Lallier, personal communication to L. Eyres (2000).

5. P.F. Bordui and M.M. Fejer, "Inorganic crystals for nonlinear optical frequency conversion," Annu. Rev. Mater. Sci. **23**, 321-379 (1993).

6. P.G. Schunemann and T.M. Pollak, "Ultralow gradient HGF-grown $ZnGeP_2$ and $CdGeAs_2$ and their optical properties," MRS Bulletin **23**, 23-27 (1998).

7. T.J. Pinguet, O. Levi, T. Skauli, L.A. Eyres, L. Scaccabarozzi, M.M. Fejer, J.S. Harris, T.J. Kulp, S. Bisson, B. Gerard, L. Becouarn, and E. Lallier, "Characterization of 0.5 mm thick films of orientation-patterned GaAs for nonlinear optical applications," *Conference on Lasers and Electro-Optics*, OSA Trends in Optics and Photonics (TOPS) Vol. 56 (Optical Society of America, Washington, DC, 2001) p. 138.

8. T. Skauli, personal communication to L. Eyres (2001).

9. P.A. Budni, L.A. Pomeranz, M.L. Lemons, P.G. Schunemann, T.M. Pollak, and E.P. Chicklis, "10 W mid-IR holmium pumped $ZnGeP_2$ OPO," *Advanced Solid State Lasers*, OSA Trends in Optics and Photonics (TOPS) Vol. 19, W.R. Bosenberg and M.M. Fejer, eds. (Optical Society of America, Washington, DC, 1998) pp. 226-229.

10. P.A. Budni, M.G. Knights, E.P. Chicklis, and K.L. Schepler, "Kilohertz $AgGaSe_2$ optical parametric oscillator pumped at 2 μm," Opt. Lett. **18**, 1068-1070 (1993).

11. C.L. Marquardt, D.G. Cooper, P.A. Budni, M.G. Knights, K.L. Schepler, R. DeDomenico, and G.C. Catella, "Thermal lensing in silver gallium selenide parametric oscillator crystals," Appl. Opt. **33**, 3192-3197 (1994).

12. E.W. Van Stryland, S. Guha, H. Vanherzeele, M.A. Woodall, and M.J. Soileau, "Verification of the scaling rule for two-photon absorption in semiconductors," Optica Acta **4**, 381-386 (1986).

13. A.A. Said, M. Sheik-Bahae, D.J. Hagan, T.H. Wei, J. Wang, J. Young, and E.W. Van Stryland, "Determination of bound-electronic and free-carrier nonlinearities in ZnSe, GaAs, CdTe, and ZnTe," J. Opt. Soc Am. B **9**, 405-414 (1992).

14. G. Imeshev, M.A. Arbore, M.M. Fejer, A. Galvanauskas, M. Ferman, and D. Harter, "Ultrashort-pulse second-harmonic generation with longitudinally nonuniform quasi-phase-matching gratings: pulse compression and shaping," J. Opt. Soc Am. B **17**, 304-318 (2000).

15. G. Imeshev, M.M. Fejer, A. Galvanauskas, and D. Harter, "Pulse shaping by difference-frequency mixing with quasi-phase-matching gratings," J. Opt. Soc Am. B **18**, 534-539 (2001).

16. S.J. Brosnan and R.L. Byer, "Optical parametric oscillator threshold and linewidth studies," IEEE J. Quantum Electron. **QE-15**, 415-431 (1979).

17. S. Guha, F.J. Wu, and J. Falk, "The effects of focusing on parametric oscillation," IEEE J. Quantum Electron. **QE-18**, 907-912 (1982).

18. G.D. Boyd and D.A. Kleinman, "Parametric interaction of focused gaussian light beams," J. Appl. Phys. **39**, 3597-3639 (1968).

CHAPTER 7: Summary

In the introduction to this dissertation, as at the beginning of the research described within it, we identified a number of applications for nonlinear optical frequency conversion in the near- and mid-IR, including countermeasures, remote sensing, and spectroscopy, as well as communications applications, such as WDM frequency conversion in the near-IR. Since these frequency conversion devices are typically limited by the performance of the nonlinear optical crystals used in their implementation, device engineers are always looking for advances in materials properties and fabrication which can improve the optical device performance. We also identified that GaAs and related zincblende semiconductor materials have excellent characteristics for applications in nonlinear optical frequency conversion, including large nonlinearities, an appealing transparency range for mid-IR generation, and a large thermal conductivity, along with compatibility with waveguide fabrication techniques. The only limitation was that of phasematching, since these isotropic semiconductors have no birefringence for phasematching and previous techniques for fabricating periodically-oriented GaAs materials proved difficult and yielded only short crystal lengths.

7.1 Accomplishments

7.1.1 Materials fabrication

At the heart of this dissertation lies the invention and demonstration of all-epitaxial techniques for fabricating orientation-patterned semiconductor films, particularly GaAs and AlGaAs. Using MBE to perform polar-on-nonpolar epitaxy, we investigated the proper parameters for GaAs growth on Ge and obtained the required crystal inversion in a heteroepitaxial GaAs/Ge/GaAs structure, solving antiphase domain complications along the way. Using these inverted GaAs heterostructures, we developed MBE-regrowth-compatible selective etching techniques and demonstrated all-epitaxial orientation-patterned templates. The domain periods demonstrated on these templates were sufficient to achieve quasiphasematching of any collinear frequency conversion process in the transparency range of GaAs/AlGaAs. We demonstrated growth of orientation-patterned thin and thick GaAs and AlGaAs films by a variety of techniques including HVPE and MBE. HVPE films had thicknesses up to 500 μm with excellent domain quality down to periods of 27 μm, while the MBE films had thickness up to 5 μm with excellent domain quality down to

periods of 3.25 μm. The domains propagated vertically through the film with large aspect ratios under both HVPE and MBE growth conditions.

7.1.2 Optical characterization

The thick GaAs films exhibit good optical transmission at both long and short wavelengths, with losses ≤ 0.1 cm^{-1} measured for the proper phasematching periods in the near-IR wavelength range attractive for pumping mid-IR generation. Harmonic generation measurements on these films found conversion efficiencies comparable those predicted theoretically. For waveguide devices, the efficiencies were limited by the large propagation losses of ~ 40 dB/cm and harmonic generation efficiencies were measured to be consistent with these losses.

7.2 State-of-the-art

Our materials and optical experiments show that orientation-patterned GaAs now meets all of the basic requirements for nonlinear optical frequency conversion and that it should be considered a promising candidate for application in mid-IR frequency conversion applications. For the thick GaAs materials in particular, we have simultaneously demonstrated a useful aperture (0.5 mm) high domain quality, proper domain periods for phasematching near-IR pumped frequency conversion, useful crystal lengths (2 cm), and good optical transmission at both near-IR and mid-IR wavelengths. Combining these with the attractive intrinsic material characteristics of high nonlinearity, high thermal conductivity and high damage threshold, GaAs appears poised to move quickly into applications by drawing on the vast accumulated knowledge about semiconductor growth and properties. Achievement of the same factors (aperture, poling, crystal length, etc.) in periodically-poled lithium niobate led quickly to demonstration of a plethora of nonlinear optical devices. We have seen from theoretical calculations that GaAs offers attractive possibilities for CW DFG, low threshold optical parametric oscillators, and high average power OPOs, particularly for conversion to beyond > 9.0 μm where $ZnGeP_2$ begins to exhibit absorption. It also has the major advantage of being pumpable by well-developed near-IR lasers in the 1 μm - 2 μm wavelength range.

7.3 Future work

Ongoing work in orientation-patterned GaAs will need to focus on several areas, including materials growth, optical properties, device modeling, and device demonstration. One of the most important issues is improving the orientation-template fabrication process. This will allow smaller template corrugations, which should produce lower defect densities in both bulk and waveguide devices. For waveguide devices, it will also be important to eliminate any corrugations which develop during regrowth, whether due to faceted growth or template defects. For bulk OPGaAs, investigation into the domain interruptions and pyramidal defects should result in higher domain quality and make possible growth of shorter period films for use with 1-μm pump lasers. Extending growth to thicker (>1 mm) apertures is also attractive and will probably occur in conjunction with the improvements in film quality.

Determining the sources of attenuation loss in both bulk and waveguide materials is extremely important, since the magnitude of these losses will determine the ultimate performance of the devices. The contributions of absorption and scattering will need to be understood and that information fed back to the crystal growth process to reduce these parasitic effects to the minimum possible levels. More detailed measurements of the optical properties of bulk materials, both absorption and dispersion, will be necessary to allow accurate device modelling. Eliminating residual ambiguity in the magnitude of the nonlinear susceptibility would also be helpful.

Many devices are presently being demonstrated in OPGaAs, including difference frequency generators and optical parametric oscillators. For near-IR-pumped operation, more detailed modelling of devices operating in the presence of two-photon absorption will be necessary to optimize performance. Waveguide device performance might be greatly improved by the design of waveguide structures resistant to corrugation-related scattering losses. As the performance of these devices improves, they can move out of the research environment and into practical applications such as spectroscopy, remote sensing, and countermeasures. Such testing under realistic device conditions will be necessary to verify thermal limitations and uncover any additional non-idealities affecting device operation.

Further into the future, since these devices utilize quasiphasematching, a variety of chirped or dispersion-tailored devices can be envisioned for applications such as pulse compression or tunable mid-IR generation. These orientation-patterned growth techniques could also be extended into other material systems to take advantage of properties like the extremely wide transparency range and low loss of ZnSe, or the potentially wide-bandwidth, mid-IR amplification pos-

sible with near-IR pump wavelengths using GaP. The larger bandgaps of these materials would also eliminate complications with two-photon absorption.

Overall, the research in this dissertation demonstrates that orientation-patterned semiconductor materials hold great promise for nonlinear optical frequency conversion. Further research into materials growth, optical properties, and devices is now required to turn that promise into a reality.